FERMILAB-THESIS-1999-37

Scaling Violation in Inclusive Jet Production

A thesis presented to the faculty of

The Rockefeller University

in partial fulfillment of the requirements for

the degree of Doctor of Philosophy

by

Alexander Akopian

1999

Abstract

Inclusive jet production in proton-antiproton collisions is studied with the CDF detector in the $|\eta|$ range 0.1-0.7, at center of mass energies of $\sqrt{s}$=630 and 1800 GeV. The ratio of scaled cross sections at two values of $\sqrt{s}$ is compared to Next-to-Leading Order (NLO) QCD predictions. Discrepancy with NLO QCD predictions at low values of fractional transverse momenta of jet $x_t(\equiv 2E_t/\sqrt{s})$ is observed. This result confirms the previous measurement by CDF at center of mass energies of 546 and 1800 GeV.

Acknoweledgements

I would like to express my gratitude to the entire Rockefeller University Experimental High Energy Physics Group. Especially, I would like to thank Professor Konstantin Goulianos, who gave me an opportunity to join the CDF experiment. His vision of the graduate study in High Energy Physics led me to Fermilab, where I had experienced the atmosphere of a real work on the on-going experiment. I benefited very much from the opportunity to share my time between hardware projects, analysis of experimental data and discussions of the obtained results.

I would like to thank my research advisor, Professor Anwar Bhatti. I gratefully acknowledge his guidance and assistance in all aspects of the research.

I consider myself fortunate for having an opportunity to meet such colleagues as Giorgio Apollinari, Kerstin Borras, Tim Cox, Luc Demortier, Nikos Giokaris, David Khazins, Stefano Lami and Phil Melese. From working with them I have learned a great deal of experimental physics and professionalism.

My special thanks are due to Anwar Bhatti, Luc Demortier and Dino Goulianos for their extremely careful reading of the manuscript and numerous important corrections, which made this thesis less painful to a reader. I also would like to thank Professor Greg Snow for his comments and suggestions.

I would like to thank the entire QCD group of CDF experiment for numerous discussions and suggestions. Especially, I would like to thank Steve Behrends, Brenna Flaugher and Joey Huston for their constant interest to this research.

I thank my fellow graduate students Suren Bagdasarov, Kenichi Hatakeyama, Arthur Maghakian, Christina Mesropian, Andrei Solodsky and Alexey Titov for sharing with me the unforgettable experience of being a graduate student at The Rockefeller University.

I am grateful to The Rockefeller University for hospitality and for providing me with the exceptional research opportunity. This thesis would not have been possible also without the dedicated effort of the entire CDF collaboration. All of the people involved have my sincerest thanks.

Finally, my most important acknowledgement is for the love, support and encouragement of my family – my parents, wife and my children.

Contents

List of Figures

List of Tables

Chapter 1

Introduction.

Quantum Chromo Dynamics (QCD) is a theory of strong interactions. It became a mathematically consistent theory in the 70's and now is part of the "Standard Model" of elementary particles. Experimental tests of QCD predictions either confirm the validity of QCD or indicate the existence of phenomena which QCD does not account for. Such tests set directions for further studies in High Energy Physics. The *Scaling Hypothesis* of inclusive jet production is one of the processes where the validity of QCD can be tested.

The first experiments in Deep Inelastic Scattering (DIS) of electrons on protons showed a point-like structure for protons. The **Naive Parton Model (NPM)** was introduced to describe quantitavely the results of DIS experiments and to make predictions for other experiments. In hadron-hadron collisions, according to the NPM, the interaction between two hadrons can be treated as an interaction between the constituents of the hadrons, the *partons*. Each hadron is described by a set of *parton distribution functions* – $pdf's$. Defined for a given type of parton, a pdf is the probability of finding this parton within the hadron, carrying fraction

$x = E_{parton}/E_{hadron}$ of the parent hadron momentum. The hadron-hadron inelastic cross section is a convolution of the *pdf*'s with the parton-parton cross section, summed over all partons in both hadrons. According to the NPM, the cross section as a function of jet $x_T \equiv 2E_t/\sqrt{s}$ (where E_t is the parton's transverse energy and $\sqrt{s}$ is the center of mass energy) does not depend on $\sqrt{s}$. The ratio of the cross sections measured at different $\sqrt{s}$ plotted versus jet x_T is unity. This statement is known as the scaling hypothesis.

In QCD, both the pdf's and the coupling constant depend on an energy scale Q^2 (*renormalization/ factorization* scale). The renormalization scale is usually chosen as the energy transferred in the interaction, and for jet production processes this is the transverse energy of the jet, E_t, multiplied by a constant. The dependence of the pdf's and coupling constant on Q^2 leads to a violation of the scaling hypothesis.

In 1988, CDF measured the inclusive jet cross section at $\sqrt{s}$=546 and 1800 GeV. The scaling hypothesis was rejected at 95% C.L. A discrepancy from the NLO QCD prediction was observed for x_T below 0.2. More data were needed to study the nature of the discrepancy.

In 1995, CDF collected data at $\sqrt{s}$=630 GeV with significantly higher statistics in order to study the validity of the QCD predictions for the ratio of inclusive jet cross-sections at $\sqrt{s}$= 630 and 1800 GeV. This study is the subject of this thesis.

Chapter 2 gives a detailed theoretical explanation of the scaling hypothesis in the NPM and its expected violation due to QCD effects. Chapter 3 describes the Fermilab accelerator complex and the apparatus used in this measurement- the Collider Detector at Fermilab (CDF). The data sets used in this analysis, the event selection and the raw inclusive jet cross section are presented in Chapter 4. Chapter 5 describes the correction for the detector effects and presents the corrected cross section.

A study of detector responses to the same E_t jets produced at different center of mass energies is presented in Chapter 6. The systematic uncertainties on the measurement of the cross section caused by the uncertainties on detector responses are presented in Chapter 7. The ratio of the scaled inclusive jet cross sections measured at center of mass energies of 630 and 1800 GeV, the uncertainties on the ratio and the discussion of the obtained result are given in Chapter 8.

Chapter 2

Theory.

2.1 Standard Model

In our present understanding, there are four fundamental forces (interactions) which govern all the physical processes in the known Universe:

- Strong
- Weak
- Electromagnetic
- Gravitation;

and there are two fundamental types of constituents of matter : *quarks* and *leptons*. There are three generations of quarks and leptons. Their properties are presented in Table 2.1. Each of these particles is described by a set of quantum numbers: spin, charge, baryon number and lepton number, isospin, mass. Quarks have an additional quantum number, color, specific for strong interactions. Each quark can have one of three possible values of color. All particles have corresponding antiparticles with the

			Charge Q	Baryon Number B	Lepton Number L	Spin
I	Quarks	u (up)	$\frac{2}{3}$	$\frac{1}{3}$	0	$\frac{1}{2}$
		d (down)	$-\frac{1}{3}$	$\frac{1}{3}$	0	
	Leptons	ν_e	0	0	1	
		e	-1	0	1	
II	Quarks	c (up)	$\frac{2}{3}$	$\frac{1}{3}$	0	$\frac{1}{2}$
		s (down)	$-\frac{1}{3}$	$\frac{1}{3}$	0	
	Leptons	ν_μ	0	0	1	
		μ	-1	0	1	
III	Quarks	t (up)	$\frac{2}{3}$	$\frac{1}{3}$	0	$\frac{1}{2}$
		b (down)	$-\frac{1}{3}$	$\frac{1}{3}$	0	
	Leptons	ν_τ	0	0	1	
		τ	-1	0	1	

Table 2.1: The properties of the quarks and leptons.

same mass and spin, and with opposite sign of charge, baryon and lepton numbers. As an example, the anti-u quark, denoted as $\bar{u}$, has spin $\frac{1}{2}$, charge $-\frac{2}{3}$, baryon number $-\frac{1}{3}$, and lepton number 0. The antiquark has also an opposite value of color. The positron (e^+) is the "anti-electron"; it has charge $+1$ and lepton number -1.

The quarks are constituents of *hadrons*. The hadrons are constructed in such a way that they are colorless and carry an integer charge and integer baryon number. There are two types of hadrons: baryons and mesons. Baryons are colorless configurations of three quarks, like $\Lambda^o(uds)$, proton $p(uud)$, neutron $n(udd)$. Mesons consist of one quark and one antiquark, like a pion, $\pi^+(u\bar{d})$. The quantum numbers of hadrons are defined by quantum numbers of constituent quarks: the baryons are half-integer spin particles (fermions) with baryon number equal to 1; the mesons are integer spin particles (bosons) with baryon number equal to 0. Besides the *valence* quarks, which establish the quantum numbers of hadrons, each hadron contains a sea

of quark-antiquark pairs, and gluons.[1]

The strong interaction is responsible for binding the quarks into hadrons and for coupling the *nucleons* into the nucleus. The weak interaction allows the transmutation of protons and neutrons into each other. These processes are responsible for synthesis of the heavy elements and were crucial in the early universe. Weak interactions are responsible for solar energy. The electromagnetic force binds the electrons to the nucleus, composing atoms. Different atoms can be bound together into molecules, again by the electromagnetic force. Gravitation is the weakest force. Its action is significant when applied to macroscopic bodies but is negligible compared to other forces at the microscopic scale.

These interactions are described by local gauge theories where force is transmitted by gauge bosons. The theories of strong, electromagnetic and weak interactions are combined in the $SU(3) \times SU(2) \times U(1)$ theory: the Standard Model of Elementary Particles. The non-abelian group representation of the electroweak interactions are described by the $SU(2) \times U(1)$ term. Quantum Chromodynamics (QCD)[2], the non-abelian local gauge theory of strong interactions, is represented by the $SU(3)$ transformation group in color space. In QCD, the force is carried by eight gluons, which are bi-color objects. In contrast to the photon, the carrier of the electromagnetic interaction, gluons can couple to each other. This property of gluons leads to the main features of the strong interactions: asymptotic freedom and confinement.

The forces, the gauge bosons and their properties are summarized in Table 2.2.

[1] The gluons are the "transmitters" of the strong interaction. They are described further in this Chapter.

Force	Gauge Boson	Q	Spin	Mass(GeV)
Strong	g (**gluon**)	0	1	0
Weak	W-**boson**	± 1	1	81
	Z-**boson**	0	1	92
Electromagnetic	γ (**photon**)	0	1	0
Gravitational	**graviton**	0	2	0

Table 2.2: Fundamental forces and gauge bosons.

2.2 Naive Parton Model

In the previous section, quarks and gluons were described as the constituents of hadrons. The Naive Parton Model (NPM)[1], a phenomenological model which was introduced to explain results of Deep Inelastic Scattering experiments, describes the hadrons as objects containing pointlike constituent-partons. According to the NPM, the interaction between two colliding hadrons can be treated as an interaction between two partons (one from each of the hadrons). The resulting hadron-level cross section can be written in the following form:

$$\frac{d\sigma}{d(p_t^2)} = \sum_{all\ \ partons} \int dx_1 dx_2 f(x_1) f(x_2) \frac{d\hat{\sigma}}{d(p_t^2)}$$

where p_t is the transverse momentum of the outgoing parton, $x_{1,2}$ is the momentum of incoming parton as a fraction of the parent hadron momentum ($x = P_{parton}/P_{hadron}$), $f(x)$ is a *parton distribution function* (PDF), a probability to find a parton carrying fraction x of the total momentum within the hadron; $\hat{\sigma}$ is the parton-parton scattering cross section.

The parton level cross section has the following form:

$$\frac{d\hat{\sigma}}{d\hat{t}} = \frac{|M|^2}{16\pi\hat{s}^2} = \frac{\alpha_s^2 |\tilde{M}|^2}{16\pi\hat{s}^2},$$

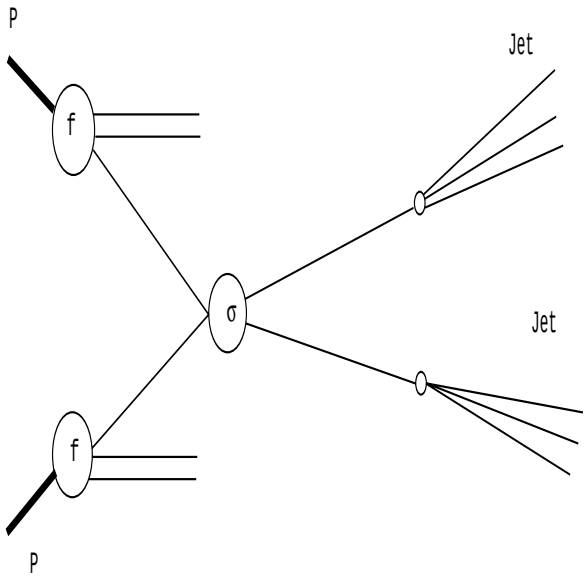

Figure 2.1: Hadron-hadron collision can be described as an interaction between partons within the hadrons.

or

$$\frac{d\hat{\sigma}}{d(p_t^2)} = \frac{d\hat{\sigma}}{d\hat{t}}\frac{\hat{s}}{\hat{u}} = \frac{\alpha_s^2|\tilde{M}^2|}{128\pi p_t^4(1+\cos\theta)}$$

where $\alpha_s^2|\tilde{M}^2|$ is the matrix element of hard scattering partons (α_s is the coupling constant of strong interactions), it depends on the scattering angle but is independent of the parton-parton center of mass energy $\sqrt{\hat{s}}$ and transverse momentum of outgoing parton. The scattering angle is denoted as θ. The variables $\hat{s}, \hat{t}$ and $\hat{u}$ are the Mandelstam variables for $2 \to 2$ parton-parton scattering,$A + B \to C + D$:

$$s = (P_A + P_B)^2, \quad t = (P_A - P_C)^2, \quad u = (P_A + P_D)^2,$$

where P indicates the 4-momentum of corresponding parton, A and B stand for two incoming partons; C and D denote the outgoing partons.

Partons are assumed to be massless and a substitution $p_t \to E_t$ is made in the formula above. The Lorentz invariant cross-section $\frac{d^2\sigma}{dE_t^2 d\eta}$, scaled by E_t^4, does not depend of

E_t and $\sqrt{s}$ separately but on a dimensionless variable $x_T = \frac{2E_t}{\sqrt{s}}$. The scaled invariant cross section averaged over an η range[2] is written as

$$E_t^4 < \frac{d^2\sigma}{d(E_t^2)d\eta} >_\eta = \frac{1}{\Delta\eta} \sum_{partons} \int dx_1 dx_2 f(x_1) f(x_2) \frac{\alpha_s^2 |\tilde{M}^2|}{128\pi(1+\cos\theta)}$$

Note that x_1 and x_2 depend only on x_T and rapidities of the jets: $x_{1,2} = \frac{x_T}{2}(e^{\pm\eta_1} + e^{\pm\eta_2})$. In the NPM, the scaled inclusive jet cross section, as a function of x_T, does not depend on $\sqrt{s}$. Thus the ratio of the scaled inclusive jet cross sections measured at different $\sqrt{s}$ is 1.0:

$$R = \frac{(E_t^3 < d^2\sigma/dE_t d\eta >_\eta)_{630}}{(E_t^3 < d^2\sigma/dE_t d\eta >_\eta)_{1800}} \equiv 1$$

In the next sections a brief description of QCD is given. It is shown that QCD predicts the dependence of the cross section on center of mass energy,$\sqrt{s}$, which means the violation of scaling hypothesis.

2.3 QCD

In perturbative QCD, the parton level cross section is expanded in powers of α_s- the *strong coupling constant*. The lowest order of the expansion corresponds to the cross section calculated in the Naive Parton Model. The higher orders of expansion lead to divergent integrals. These divergences are *regularized* either by the introduction of an ultraviolet momentum cut-off Λ (covariant regularization), or by reducing the space-time dimension $D = 4 - 2\epsilon$ (dimensional regularization). The regularized divergences are then absorbed into the definitions of the coupling constant and mass by a *renormalization* procedure, which introduces a new energy scale μ. The renormalized parameters depend explicitly on μ. The renormalized

[2] η is the pseudorapidity, defined as $\eta = \ln\tan(\theta/2)$, where θ is the scattering angle.

operators construct a Lie group when changing with μ. The coupling constant and the mass obey the *Renormalization Group Equations* (RGE):$\mu\partial g/\partial\mu = \beta(g)$ and $\mu\partial M_j/\partial\mu = \gamma_M(g)\cdot M_j$, where β and γ_M are renormalization group coefficients, which can be calculated in the perturbative theory, g is the coupling constant ($\alpha_s \equiv g^2/4\pi$). The RG equations provide the invariance of the observables under the changes of μ. The $S-$matrix should be renormalization-group invariant: $\mu DS/D\mu = 0$. The covariant derivative is defined as $\mu\frac{D}{D\mu} = \mu\frac{\partial}{\partial\mu} + \beta\frac{\partial}{\partial g} + \gamma_M \sum M_i \frac{\partial}{\partial M_i}$. The beta-function, $\beta = \mu\partial g/\partial\mu$ is the sensitivity of the coupling constant g to the renormalization parameter μ. It expands in powers of g as

$$\beta(g) = -bg^3(1 + b'g^2 + \cdots)$$

where $b = (33 - 2N_f)/12\pi$, N_f is the number of quark flavors.

Integration of the one-loop equation for β ($\beta(g) = -bg^3$) leads to a solution, which exhibits the dependence of the coupling constant on the renormalization scale:

$$g^2(Q^2) = \frac{g^2(\mu_o^2)}{1 + bg(\mu_o^2)\ln(Q^2/\mu_o^2)} \quad or \quad g^2(Q^2) = \frac{1}{b\ln(Q^2/\Lambda_{QCD}^2)},$$

where $\Lambda_{QCD} = \mu_o \cdot exp([-2bg^2(\mu_o^2)])$. The strong coupling constant, α_s, can be written as:

$$\alpha_s(Q^2) = \frac{12\pi}{(33 - 2N_f)\cdot\ln(Q^2/\Lambda_{QCD}^2)}.$$

This dependence of α_s on the renormalization scale Q^2 shows a property of strong interactions, *asymptotic freedom*: the coupling constant decreases with increasing Q^2. For high energies (or short probing distances) the partons inside the hadrons can be treated as free particles.

The coupling within the hadrons at the low energies, on other hand, reflects another property of the strong interactions, *confinement*: no single quark can exist apart from

other quarks and gluons.

The value of Λ_{QCD} is not predicted by theory. An evaluation of Λ_{QCD} is based on the experimental measurements of α_s and depends on the renormalization scheme used in the theory and on the number of active flavors.[3] The experimentally measured[3] value of $\Lambda^5_{\overline{MS}}$ is $202\pm^{65}_{53}$ MeV, where $\overline{MS}$ notation refers to the Modified Minimum Subtraction scheme for the renormalization. The number of active flavors is 5.

The hard scattering of two constituent quarks or gluons (one from each hadron) is governed by the strong interaction between two hadrons. During the scattering, a quark within a hadron can experience an impact and acquire a momentum which strikes the quark out of the hadron. The outgoing quark couples with the vacuum quarks and forms colorless hadrons. This process of coupling is called *hadronization* or *fragmentation*. The momentum of the struck quark is significantly higher than the momenta of the quarks picked from the vacuum. Resulting hadrons are almost collinear with the struck quark. This strongly collimated "bunch" of hadrons is called a jet.

The constituent quarks which did not participate in the hard scattering are called *spectators*. The spectator partons also fragment into hadrons which form the so called *Underlying Event* (UE). The UE hadrons do not have high transverse momenta (P_t). Most of these hadrons move in directions, close to the directions of the parent partons (e.g. directions of the colliding hadrons). The P_t of UE hadrons is roughly uniformly distributed in η (away from edge of phase space). The energy of the measured jets should be corrected for the contribution of the UE.

As was mentioned above, in perturbative QCD, the parton level cross section is expanded in powers of $\alpha_s(Q^2)$. The precision of the calculation at some order increases

[3]The number of flavors is chosen as the number of quarks with masses below the renormalization scale μ.

with decreasing value of $\alpha_s(Q^2)$. In practice, the long-distance part (low momentum partons, which were radiated before the hard scattering) is separated from the short-distance cross section. The latter is calculated by means of perturbative QCD, while the former is "factored" into the parton distribution functions. This procedure is known as *factorization*[4]; it introduces a factorization scale (μ_f), which should be chosen to be of the same order as the scale of parton-parton interaction. For simplicity, the renormalization and factorization scales are usually set equal. The parton distribution functions with factorized long-distance part have the form:

$$f_i(x,Q) = \sum_a \int_x^1 \frac{d\xi}{\xi} C_{ia}(x/\xi, Q/\mu, \alpha_s(\mu)) f_{a/H}(\xi,\mu) + \mathcal{O}(1GeV/Q)$$

where $f_{a/H}$ is the long-distance part. It is independent of the hard scattering process, is specific to the hadron H and depends on the factorization scale μ. C_{ia} are the so-called Wilson's coefficients; they depend on the renormalization and factorization scales and are independent of the hadron identity H.

The RGE for parton distribution functions are written in the form:

$$\mu \frac{df_{a/H}(x,\mu)}{d\mu} = \sum_b \int_x^1 \frac{d\xi}{\xi} P_{ab}(\xi/x, \alpha_s(\mu)) f_{b/H}(\xi,\mu)$$

These are called the Dokshitzer-Gribov-Lipatov-Altarelli-Parisi equations[5]. The indices a and b denote either a quark/anti-quark flavor or a gluon. The above equations describe the evolution of parton of type a in the hadron H. The kernels P_{ab} are the *splitting functions*. They can be expanded in series of power of α_s and are calculable in the perturbative theory. The splitting function, $P_{ab}(x)$, at leading-order can be interpreted as the probability to find a parton a in the parton b carrying fraction x of the longitudinal momentum of the parent parton and a transverse momentum squared $Q^2 \ll \mu^2$. The parton distribution functions evolve with the energy scale Q^2. The DGLAP equations provide a procedure for evaluation of the pdf's at any value

of the energy scale given a set of initial pdf's at some energy scale Q_o^2. This initial set of pdf's is obtained from experimental data by means of a *Global Analysis*.

2.4 Global Analysis

The Global Analysis is a project of constructing a set of pdf's, which is consistent with a variety of experimental measurements of different processes. Parameterized forms (one for each quark flavor and a gluon within a proton) are used as pdf's at some renormalization/factorization scale Q_o^2. Each of these initial parameterizations is evaluated at different values of the energy scale Q^2 and the theoretical predictions are calculated for every process for which there exists an experimental result. The parameters are optimized so that the best agreement (by means of a χ^2-test) is achieved between the experimental data and the theoretical calculations given the final pdf's. This final set can be used for comparison of new experimental data with theory. Currently, different sets of pdf's are available: MRS[6], GRV[7], CTEQ[8]. In this research, the CTEQ4M set from the CTEQ collaboration is used.

2.5 Jets

A jet is a narrow bunch of hadrons resulting from the fragmentation of the struck quark or gluon. This definition of the jet is rather abstract. In practice, a jet is defined in terms of its properties, e.g. the E_t, the spatial distribution of energy within the jet, the direction of jet axis. The requirement on a jet definition is that there should be a correspondence between the theoretically calculated jet properties and the algorithm used to reconstruct the jet in the experimental measurements. In the comparison of experimental data with theoretical predictions, the same definition

should be used in both theory and experiment, since the resulting cross section depends on the jet definition.

The *clustering algorithms*, such as JADE[9] and modified JADE[10] (also known as Durham or k_T algorithm) are based on combining particle momenta, so that a pair of particles can be substituted by a pseudo-particle. This new pseudo-particle has either its 4-momentum equal to the sum of the 4-momenta of the original two particles (*E-scheme*); or its 3-momentum equal to the sum of the 3-momenta of the original particles, and the energy equal to the sum of the weighted energies of the two particles (*P-scheme*). This algorithm is used in e^+e^- collisions.

The *cone algorithm* is typically used at hadron-hadron colliders. The jet is defined as energy deposited within a cone of radius $R = \sqrt{(\Delta\eta)^2 + (\Delta\phi)^2}$ in $\eta - \phi$ space, where η is the pseudo-rapidity and ϕ is the azimuthal angle.

The standard cone algorithm was adopted in 1990 at the Workshop on High Energy Physics in Snowmass, Colorado[11], and is referred to as the *Snowmass accord*. In this algorithm, the $E_t,\ \eta,\ \phi$ of the jets are calculated as E_t-weighted sums over particles or calorimeter cells within a cone of radius R:

$$E_t^{jet} = \sum_{i \in R} E_t^i$$

$$\eta_{jet} = \frac{1}{E_t^{jet}} \sum_{i \in R} E_t^i \cdot \eta_i$$

$$\phi_{jet} = \frac{1}{E_t^{jet}} \sum_{i \in R} E_t^i \cdot \phi_i$$

The suggested value of R in the Snowmass accord is 0.7. This size of the jets is optimal for both collecting the most energy of the jet within the cone ($\geq$90% for jets with $E_t > 20$ GeV) and for spatial resolution of the jets in multijet events.

The JETCLU[12] jet reconstruction algorithm, employed by CDF, selected a *seed*

tower (a tower is a calorimetry cell- see details in Chapter 3) with transverse energy E_t >1 GeV. The adjacent seed towers were combined into a *precluster* so that the E_t of the seed towers in a precluster were decreasing monotonically. In $\eta - \phi$ space, an E_t^{tower} weighted centroid of the precluster was obtained. A cone with radius $R = \sqrt{(\Delta\eta)^2 + (\Delta\phi)^2} = 0.7$ was constructed around the centroid. A new E_t-weighted centroid was calculated for all the towers within the circle and a new circle was drawn around the new centroid. Further iterations of this process were performed until the centroid became stable.

Special care was taken for overlapping clusters- if the total E_t of the "common" towers was greater than $\frac{3}{4}E_t$ of either cluster, then the two clusters were merged together. Otherwise, the two clusters were kept separate (i.e. not merged) and the common towers were included into the closer cluster. No overlapping jets were allowed. The final clusters were defined as the jets measured with the CDF Detector.

2.6 Scaling Violation

The running of the coupling constant and the evolution of parton distribution functions in QCD means that the dimensionless Lorentz-invariant inclusive jet cross section has the form:

$$E_t^3 < \frac{d^2\sigma}{dE_t d\eta} >_\eta = \frac{1}{\Delta\eta} \sum_{all\ partons} \int dx_1 dx_2 f(x_1, Q^2) f(x_2, Q^2) \frac{\alpha_s(Q^2)^2 |\tilde{M}^2|}{128\pi(1+\cos\theta)} \rightarrow F(x_t, Q^2)$$

where $Q = \xi E_t$. In the inclusive jet calculations both the renormalization and factorization scales are chosen to be the transverse energy of the jets multiplied by a factor. Since $x_t = 2E_t/\sqrt{s}$, the renormalization and factorization scale becomes $Q = \xi E_t = \xi x_t \sqrt{s}/2$. For same x_t jets, the cross section does depend on the center of mass energy $\sqrt{s}$, leading to a violation of the scaling hypothesis. The dependence of

α_s and the pdf on $\sqrt{s}$ is illustrated in Figure 2.2.

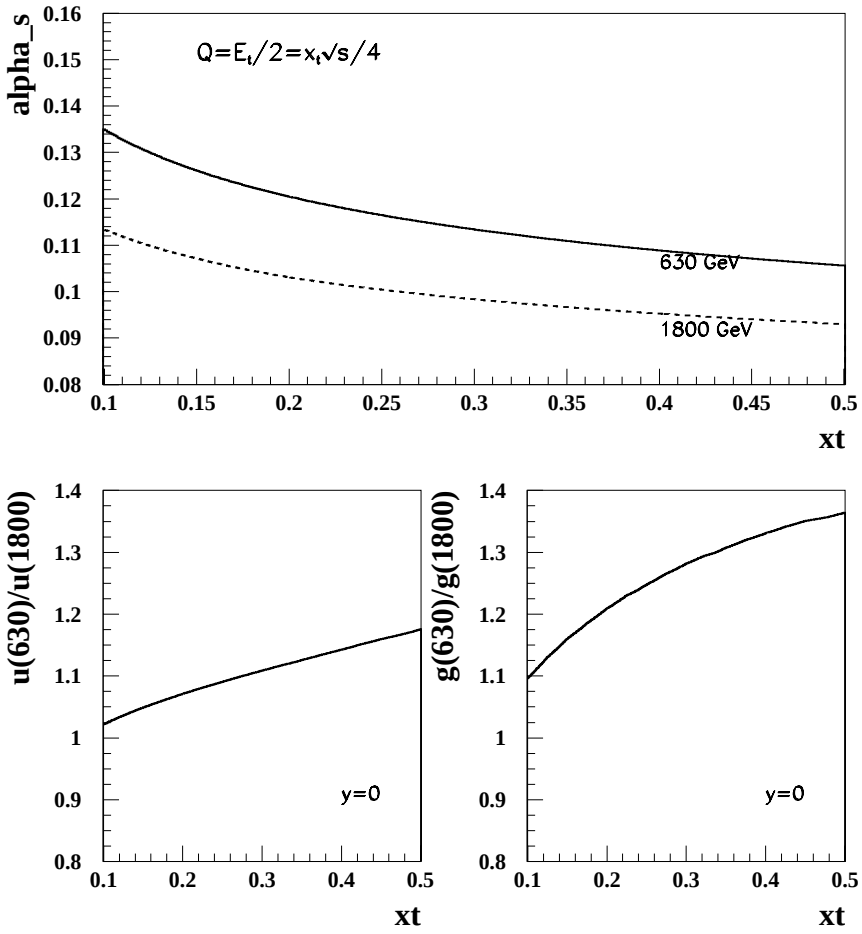

Figure 2.2: α_s as function of x_T for $\sqrt{s}$=630 and 1800 GeV (upper plot); ratio of pdf for up-quark and gluon (630 GeV over 1800 GeV) as function of x_T (bottom plots).

2.7 EKS NLO QCD Calculations

In this research, NLO QCD calculations by the EKS group[14] were used. In these calculations the final state may include three partons. If two of the partons are within radius R, they are combined into one jet. At NLO, the jet cross section depends on the cone radius. Figure 2.3 presents the theoretical prediction and the

measurement by CDF of the inclusive jet cross section as function of R. At R=0.7, the

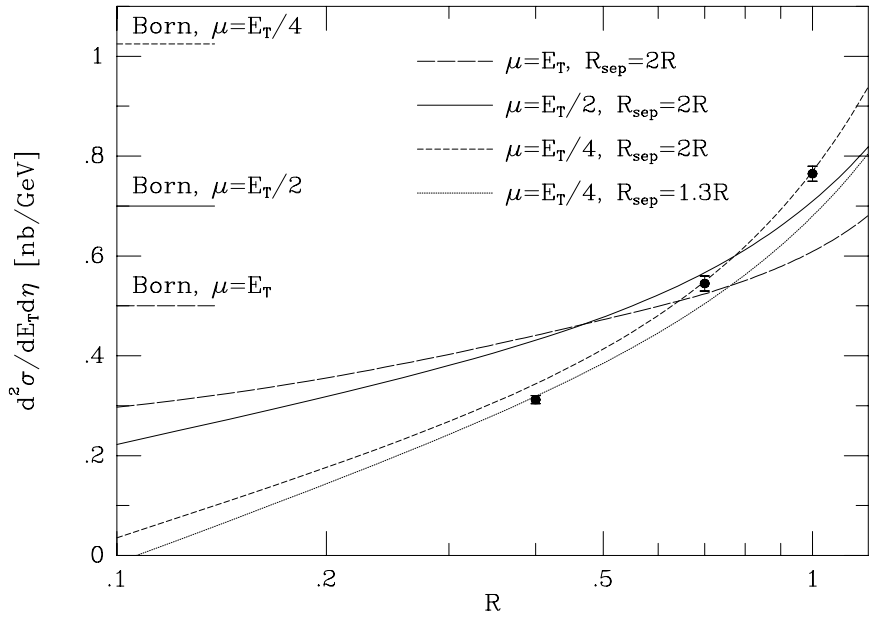

Figure 2.3: Dependence of the inclusive jet cross section on the cone radius. Jet cross section is measured by CDF (dots) and predicted by LO and NLO QCD at $\sqrt{s}$=1800 GeV, E_t=100 GeV, 0.1< $|\eta|$ <0.7

dependence of the cross section on the choice of the renormalization and factorization scale is weak. The cross section also depends on the criteria of merging two jets. In cone algorithms, the two jets are merged if the distance between them is less than a predefined parameter R_{sep}. The value $R_{sep} = 1.3R$ corresponds to the JETCLU algorithm. In EKS, the production of each jet is considered as a separate process with the renormalization and factorization scale equal to the transverse energy E_t of the jet multiplied by a factor.

2.8 The Ratio of Scaled Cross Sections as a Test of QCD Predictions

Experimental measurement of the cross section of some process with a variety of the detectors at different center of mass energies and further comparison with the QCD prediction is the usual way to test QCD. However, if within one experiment a cross section of some process is measured at different center of mass energies, then the ratio of the cross sections at different $\sqrt{s}$ is a stronger test of the QCD predictions than each measurement separately because most of systematic uncertainties cancel in ratio.

In the statistical analysis, if the parameter of interest f is a function of a number of other parameters a_i, and each of the parameters a_i is known (measured) with some uncertainty $\delta(a_i)$, then the uncertainty on the parameter f itself has the following form:

$$\delta(f) = \sqrt{\sum_i \sum_j \left(\frac{\partial f}{\partial a_i}\delta(a_i)\right) \cdot \left(\frac{\partial f}{\partial a_j}\delta(a_j)\right) \cdot \rho_{ij}},$$

where ρ_{ij} is the correlation coefficient of the measurements of parameters a_i and a_j. The correlation coefficient changes from 0 for uncorrelated uncertainties to 1 (-1) for completely correlated (anti-correlated) uncertainties.

The uncertainty on a function of two parameters is given by

$$\delta(f) = \sqrt{\left(\frac{\partial f}{\partial a}\delta(a)\right)^2 + \left(\frac{\partial f}{\partial b}\delta(b)\right)^2 + 2\rho_{ab}\left(\frac{\partial f}{\partial a}\right)\left(\frac{\partial f}{\partial b}\right)\delta(a)\delta(b)}.$$

If f is the ratio of parameters a and b ($f = a/b$), then the uncertainty on f becomes:

$$\delta(f) = \sqrt{\left(\frac{1}{b}\delta(a)\right)^2 + \left(\frac{a}{b^2}\delta(b)\right)^2 - 2\frac{a}{b^3}\delta(a)\delta(b)\rho_{ab}}$$

or

$$\delta(f) = f\sqrt{\left(\frac{\delta(a)}{a}\right)^2 + \left(\frac{\delta(b)}{b}\right)^2 - 2\left(\frac{\delta(a)}{a}\right)\left(\frac{\delta(b)}{b}\right)\rho_{ab}}$$

If two measurements with finite uncertainties are correlated, then the uncertainty on the ratio is less than it would be if there were no correlation. If the correlation $\rho_{ab} \equiv 1$, then

$$\delta(f)/f = |\delta(a)/a - \delta(b)/b|$$

If two measurements are totally correlated, then the relative uncertainty on the ratio of these two measurements equals the absolute value of the difference between the relative uncertainties of each of them.

This result applies to the measurement of the ratio of the inclusive jet cross sections. Since the same detector is used for the measurements at two center of mass energies, the systematic uncertainties of the measurements are correlated and the uncertainty on the ratio will be reduced. The same argument can be applied to the QCD predictions- there is an uncertainty caused by the choices of the renormalization and factorization scale and of the set of pdf, and a partial cancelation of these uncertainties reduces the overall theoretical uncertainty of the result.

This is why the comparison of the ratio of inclusive jet cross sections with the QCD predictions is expected to be more accurate than the separate comparison of the cross sections with the corresponding theoretical calculations at two values of the center of mass energy.

2.9 HERWIG Event Generator

The HERWIG Monte Carlo event generator[13] was used in this work for studies of the energy flow in the jets and the fragmentation dependence on the center

of mass energy. HERWIG is based on the computation of the Leading Order (LO) matrix elements and *parton shower* simulation of the initial and final state radiation. In the parton shower approach, the final state radiation is treated as splitting (by means of DGLAP equations) of incoming and outgoing quarks and gluons. The splitting continues until the parton has an E_t below a cut-off scale. Below this energy a phenomenological fragmentation model is employed. The initial state radiation carries a certain fraction of the 4-momentum of the incoming parton, which changes the 4-momentum Q transfered in the process. This leads to the evolution of the pdf in the incident hadron.

The LO calculations with parton shower simulation serves as a good approximation to the NLO QCD calculations. The advantage of such an event generator is that it produces a list of particles resulting from the hadron-hadron interaction. This output can be used for direct comparison with raw measurements after the particles are passed through the detector simulation package.

2.10 Results of Other Experiments

A number of experiments were undertaken to measure the inclusive jet cross section at different center of mass energies. The goal of these experiments was to check if the QCD prediction of the scaling violation is correct.

At the UA2 experiment (CERN, $Sp\bar{p}S$), the inclusive jet production cross section was measured in $p\bar{p}$ collisions at $\sqrt{s}$=546 and 630 GeV. At $\sqrt{s}$=630 Gev, a p_t-dependent increase of the cross section with respect to the $\sqrt{s}$=546 GeV data was observed. The increase could be described both by QCD calculations and by "approximate

x_t-scaling". The comparison of UA2 results with the measurements by the AFS collaboration[16] in $p\bar{p}$ collisions at $\sqrt{s}$=63 and 45 GeV exhibited the expected scale-breaking effects[15].

A similar measurement was performed by the UA1 group at CERN[17]. The inclusive jet cross section was measured at the same two center of mass energies, 546 and 630 GeV. The conclusion was that the observed increase in the cross section with $\sqrt{s}$ is consistent with scaling. The QCD calculations were presented, which show that comparison with much higher center of mass energy ($\sqrt{s} \sim 2000$ GeV) would be needed to be sensitive to non-scaling QCD effects. At the time of these measurements only Leading Order QCD calculations were available.

The CDF experiment was the first one to measure the inclusive jet cross section at such far from each other center of mass energies as $\sqrt{s}$=546 and 1800 GeV[18]. The scaling hypothesis was ruled out with 95% Confidence Level. However, at low x_t the ratio of the measured cross sections was inconsistent with the NLO QCD predictions (Fig 2.4).

An attempt to explain the difference between the theory prediction and the CDF measurement was made by S.Ellis[19]. The Underlying Event E_t at CDF was estimated by measuring E_t in a cone perpendicular to the leading jet axis. The measured value of E_t was subtracted from the E_t of the jet. S.Ellis argued that energy associated with the hard scattering could also contribute to the cone perpendicular to the jet axis ("splash-out" effect). As a result the E_t of the measured jets was over-corrected. The correction for the splash-out effect would decrease the observed disagreement to about 1σ level. However, reanalysis of CDF data, using new UE definition, showed no such effect.

Recently, the DØ collaboration presented the ratio of inclusive jet cross sections at

$\sqrt{s}$=630 and 1800 GeV. Results of two experiments are compared in Chapter 8.2

It is the goal of the current analysis to study the observed discrepancy between the ratio of the cross sections measured by CDF at $\sqrt{s}$=546 and 1800 GeV and the NLO QCD predictions.

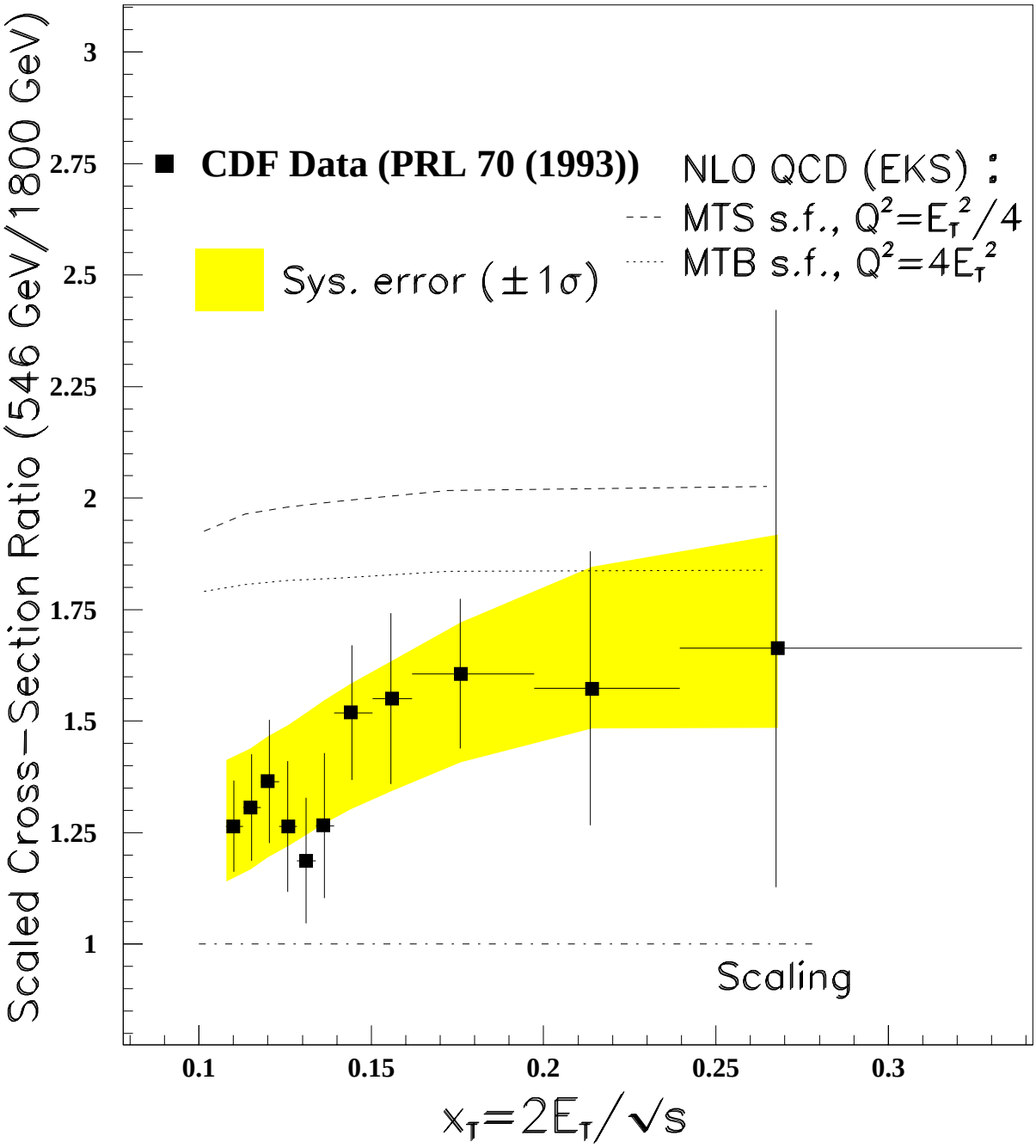

Figure 2.4: CDF data at 546 GeV confirmed scaling violation. However, a discrepancy with NLO QCD was observed.

Chapter 3

TEVATRON Collider and the CDF Detector.

3.1 Tevatron Collider

The Fermilab Tevatron collider is an accelerator colliding protons (p) with anti-protons ($\bar{p}$) at a center of mass energy of 1.8 TeV. The Fermilab accelerator complex consists of six stages of acceleration (Figure 3.1).

A **Cockroft-Walton Generator** provides the first stage of acceleration. Electrons are added to the hydrogen atoms creating negative charged ions. The ions are accelerated by a positive voltage up to the energy of 750 KeV.

The **Linac** is a linear accelerator. Negative hydrogen ions are injected into the Linac and are accelerated up to the energy of 400 MeV.

The **Booster** is a synchrotron type accelerator. The hydrogen ions are stripped from the electrons before they enter the Booster. The resulting protons are accelerated to the energy of 8 GeV. The Booster loads twelve bunches of protons into the Main

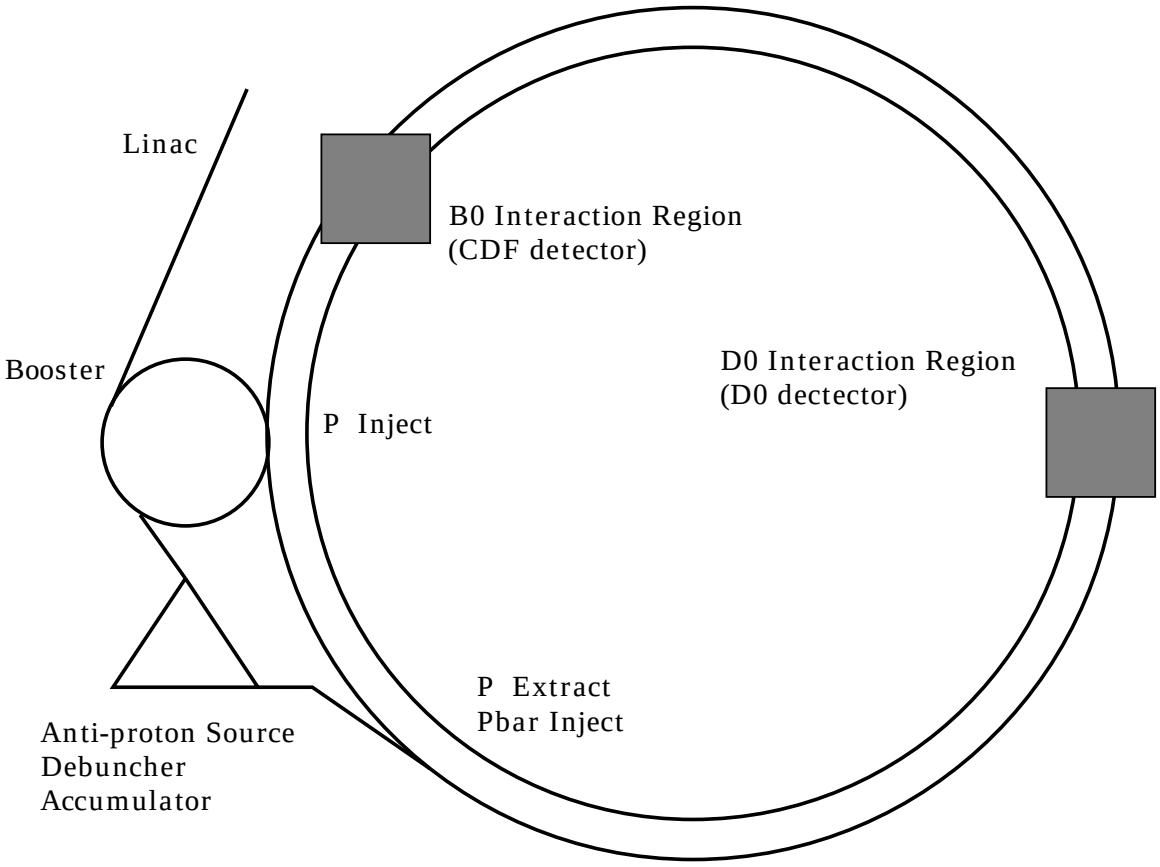

Figure 3.1: Schematic view of Tevatron Collider

Ring.

The **Main Ring** is another proton synchrotron which accelerates p from 8 GeV to 150 GeV. When a sufficient amount of antiprotons is produced (as described below), they are also injected into the Main Ring and are accelerated simultaneously with the protons but in the opposite direction.

The **Antiproton Storage Ring** is the machine where $\bar{p}$ are stored and "bunched" before injection into the Main Ring. Protons accelerated to 120 GeV in the Main Ring are extracted and focused onto a target. The collision in the target produces secondary particles. Antiprotons are selected from the secondary particles and transported to the Debuncher. After stochastic cooling they are transported to the Accumulator

ring. When the required number of $\bar{p}$ are produced they are reinjected into the Main Ring and are accelerated to 150 GeV.

The **TEVATRON** is a superconducting synchrotron, which is located in the same tunnel as the Main Ring. The bunches of p and $\bar{p}$ at energy of 150 GeV are injected from the Main Ring into the TEVATRON. In the TEVATRON, they are accelerated simultaneously to 900 GeV and are directed to a head-on collision in a designated area at the center of the detector. The instantaneous luminosity of the Tevatron is given by

$$L = \frac{N_p N_{\bar{p}} f}{\mathcal{A}}$$

where N_p and $N_{\bar{p}}$ are the numbers of p and $\bar{p}$ per bunch, f is the frequency of bunch crossings and $\mathcal{A}$ is the effective area of the crossing beams. The numbers of protons and antiprotons in the bunches (the instantaneous luminosity) continuously decreases with time, so that after some time a new injection of particles is needed. The period of time between two injections is defined as a *run*. The average duration of a run during the 1995-1996 data collection was about 20 hours.

The rate of all events is proportional to the instantaneous luminosity: $Rate = \mathcal{L} \cdot \sigma$, where σ is the cross section of the corresponding process. Since the luminosity changes during a run, the rate of events also changes. In practice, a number of events accumulated during some time is measured rather than the rate of production of these events. This corresponds to an integration over time: $N_{events} = \int Rate(t) \cdot dt = \sigma \cdot \int \mathcal{L} dt$, where $\int \mathcal{L} dt$ is the integrated luminosity (usually integrated over the duration of a run).

The instantaneous luminosity (at its maximum) is a characteristic of the collider. The integrated luminosity, on the other hand, is a measure of the total number of "interactions" stored on magnetic tape. Section 3.2.3 describes how the integrated

luminosity is measured in this experiment.

3.2 Collider Detector at Fermilab (CDF)

CDF is a multipurpose detector built at the Tevatron. Components of the detector include the tracking, calorimetry and the muon subsystems. Detailed description of CDF is given in [20]. This section contains a brief description of the detector with emphasis on the components necessary for the inclusive jet analysis.

The coordinate system of the detector reflects the axial symmetry with respect to the beam-pipe (azimuthal angle ϕ), and forward/backward symmetry (pseudorapidity $\eta = -\ln(\tan(\theta/2))$, where θ is the polar angle), with z, the direction of proton beam, being the third coordinate. Since there always is a spread of z-positions of the interaction point around the center of the detector, two values of η are distinguished: *detector* η, measured from the geometrical center of the detector, z=0, and denoted as η_D, and *event* η, measured from the interaction point in an event, written simply as η. The detector coordinates are used in this section to point out the location of the different detector units with respect to the center of the detector. There is also a global coordinate system: z-axis along the proton direction, x-axis pointing to the outside of the accelerator ring in the horizontal plane, and y-axis pointing up.

The detector features 2π coverage in azimuth and -4.2 to 4.2 in pseudorapidity, which makes it close to 4π coverage, leaving open the forward (high-η) region for incoming bunches of protons and antiprotons. There are three main divisions of the detector in η_D-space:

- Central $|\eta_D| < 1.1$
- Plug $1.1 < |\eta_D| < 2.4$

- Forward 2.4< $|\eta_D|$ <4.2

The tracking component is located in the Central region of the detector, while the muon system is located in the Central and Forward parts. Figures 3.2 and 3.3 present a quarter view and an isometric cut-away view of the detector, respectively. In the

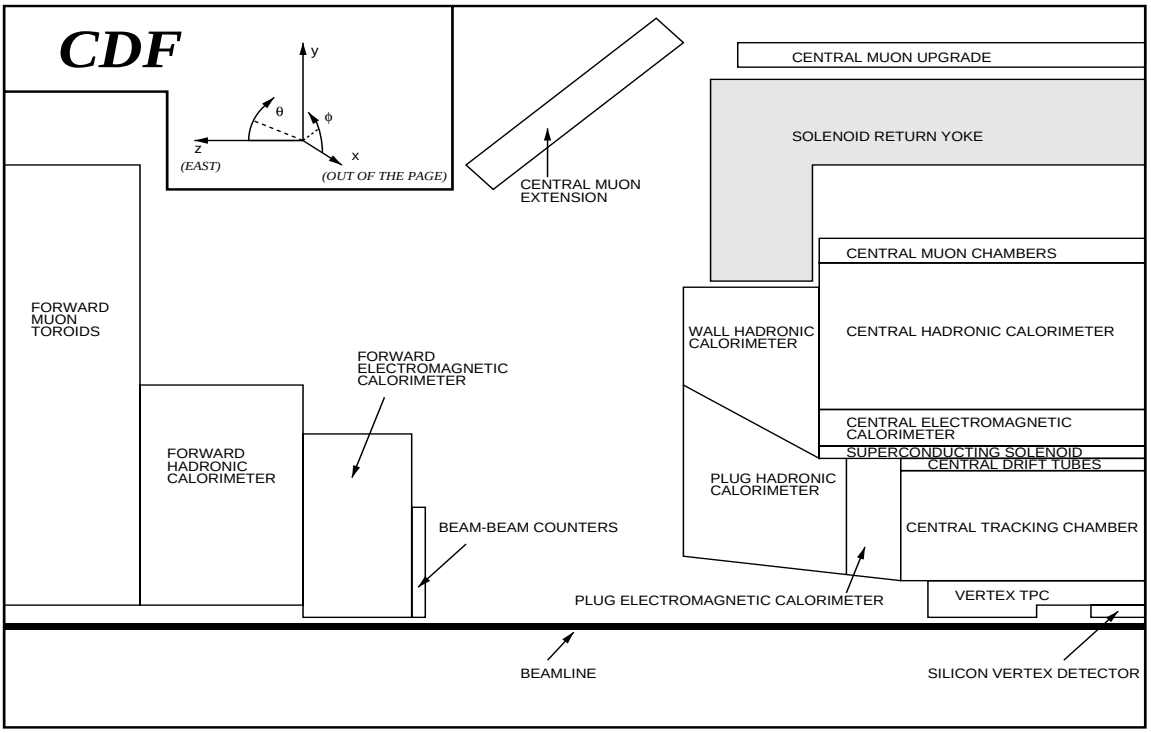

Figure 3.2: Quarter view of the CDF detector

inclusive jet analysis, only jets in the η-range 0.1-0.7 (central detectors) are used.

3.2.1 Tracking Detectors

In the range $|\eta|$ <1.1, particles from the interaction point pass through the following detector components:

- charged particle tracking system
- sampling calorimeter

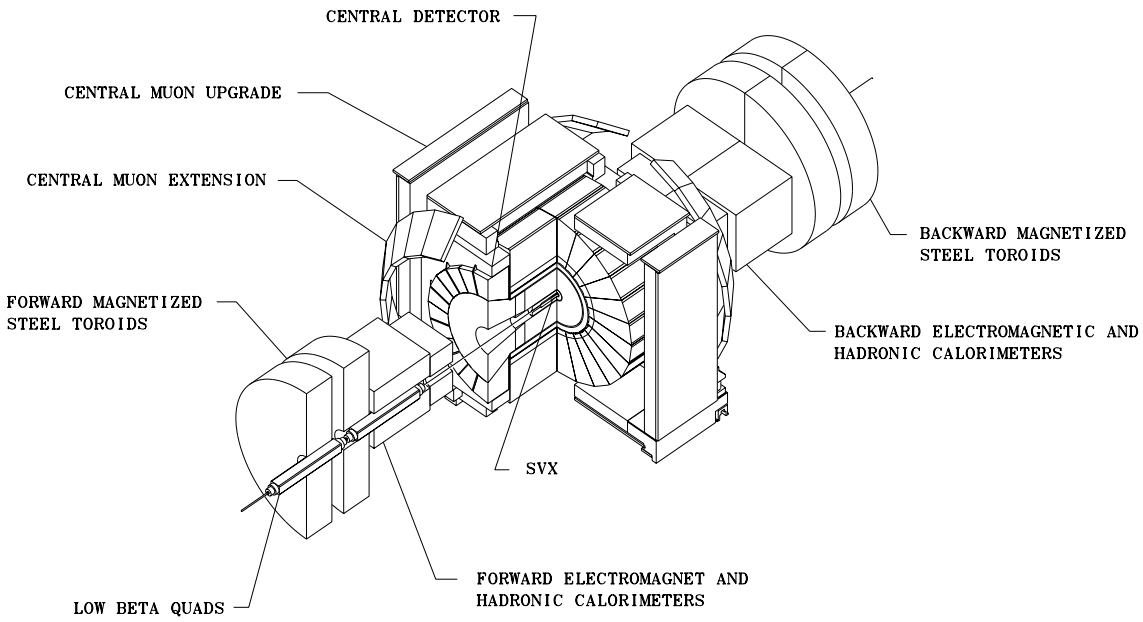

Figure 3.3: Isometric cut-away view of the CDF detector

- muon detector

The tracking system is used to provide position, momentum and charge information of charged particles along their helical trajectories in the solenoidal magnetic field. The tracking information is used in this analysis for studies of the charged component of jets (study of jet fragmentation dependence on center-of-mass energy) and for a precise measurement of the primary interaction point.

The components of the tracking system are a solenoidal magnet, a silicon microstrip vertex detector (SVX), a vertex chamber (VTX), the central tracking chamber (CTC), and the central drift tubes (CDT).

The CDF solenoidal magnet provides an axial magnetic field of 14.1 kG within a cylindrical volume of 5 m in length and 3 m in diameter. A NbTi/Cu superconductor was used in the construction of the magnetic coil. The magnetic field flux is returned

through a steel yoke, which supports the calorimeters.

The silicon vertex detector (SVX')[21] provides precise tracking in the $r-\phi$ plane, separating secondary from primary vertices, and is used to obtain a measurement of the impact parameter of the traversing particles.

The SVX' consists of two 12-sided barrels with an active length of 51 cm. Barrels are located coaxially with the beam pipe on each side of the geometric center of the detector. Each barrel is made of 4 layers of silicon microstrip sensors. The microstrips are oriented parallel to the barrel axis. Each ladder covers 30^o in azimuth. Twelve ladders are combined in a layer to cover 360^o in azimuth.

The silicon is n-doped, there is a p-doped region under each strip, providing an array of pn diodes. A charged particle passing through the strip excites the electrons. The resulting *charges* and *holes* are "collected" from the diode region by the electric fields. The high strip density results in an SVX transverse impact parameter resolution of 40μm.

The vertex chamber (VTX) provides tracking information in the $r-z$ plane. The two halves of the VTX are coaxial with the beam pipe and surround the SVX barrels. Each half consists of 22 octagonal modules, which cover 360^o in azimuth and zero to 3.25 in η. The 18 modules immediately surround the SVX. They contain 16 sense wires strung in the $r-\phi$ plane perpendicular to a radial line extended from the origin. The remaining 10 modules are located at larger z. They contain 24 sense wires. The drift gap is 4 cm and the active medium is argon-ethane. The units are rotated in ϕ, so that the VTX segments may better match the CTC $r-\phi$ track segments.

The central tracking chamber[23] (CTC) provides precise position and momentum measurements of high transverse momentum tracks for $|\eta|<1.1$. In this analysis the information gathered with the CTC was used for the study of jet fragmentation for

different jet E_t and center of mass energies.

The CTC is a cylindrical drift chamber (Figure 3.4), which surrounds the VTX. It

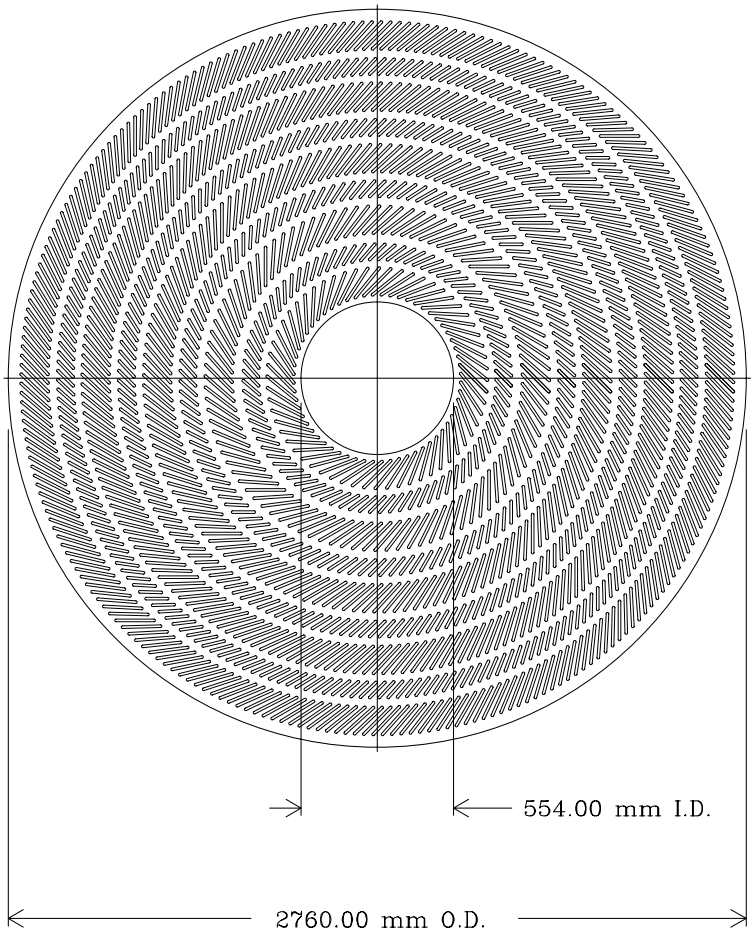

Figure 3.4: End view of the CTC.

has inner and outer diameters of 55.4 cm and 276.0 cm and a length of 3.2 m. The CTC consists of 84 layers of sense wires arranged into 9 superlayers. In five of the superlayers, the wires are parallel to the beam line. These *axial* superlayers contain 12 sense wire layers each. They are interleaved with four superlayers of *stereo* wires in which the angle between the sense wires and the beam line alternates between $\pm 3^o$. Both axial and stereo superlayers are divided into cells so that the maximum drift

distance is less than 40 mm. The longitudinal resolution of a stereo wire is approximately equal to the position resolution of the calorimetry ($\sim$ 4mm).

Each sense wire is connected to a multiple hit time-to-digital converter (TDC), mounted in a FASTBUS crate.

The central drift tube[24] (CDT) consists of three layers of 672 drift tubes aligned parallel to the beam pipe, surrounding the CTC. Each drift tube is 3m long and 1.27 cm in diameter. A 50 μm diameter stainless steel wire was used as anode for each drift tube. The CDT provides $r-z-\phi$ information. Charge division along the anode wire provides the $r-z$ part of the tracking information while the measurement of the drift time in three layers provides the $r-\phi$ part of the information.

3.2.2 Central Calorimetry

The most important part of the CDF detector for this analysis is the central calorimeter. It consists of two major parts- *Central Electromagnetic Calorimeter*[25] (CEM) and hadron calorimeters[27]. The hadron calorimeters are the *Central Hadron Calorimeter* (CHA) and the *Endwall Hadron Calorimeter* (WHA).

The CEM is located immediately outside the solenoidal magnet. It covers 360^o in ϕ and -1.1 to 1.1 in η, and has a depth of 5.9 radiation lengths (including the magnetic coil).

A hybrid design was used for the CEM. Thirty-one layers of 5 mm thick SCSN-38 polystyrene scintillator as active medium read out with wavelength shifter provided the energy measurement with a resolution σ/E [GeV] of $13.5\%/\sqrt{E}$. The scintillator layers were interleaved with layers of lead.

At approximately the depth of the maximum of an electromagnetic shower, layers of

strip chambers were located. These provided position determination and measurement of the transverse shower development.

The CEM calorimeter was constructed from 48 modules (24 on each side). The individual modules were wrapped in two layers of vellum drawing paper. A general layout of each module is presented in Figure 3.5. Each module was divided into ten

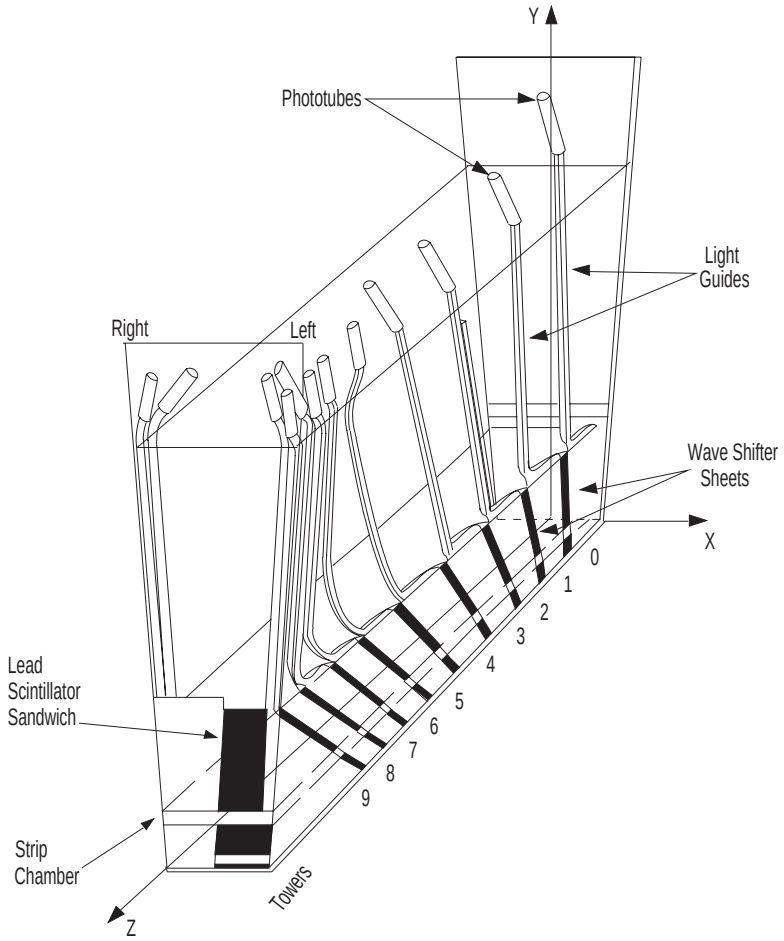

Figure 3.5: Layout of CEM unit.

towers with projective geometry. Every tower covered approximately 0.1 units in η and 15^o in ϕ. The light from each tower was collected with a wavelength shifter and transmitted to the phototube (Hamamatsu $R850$) by lightguides. Two phototubes

were used per tower; one for each side of the tower.

Three separate calibration systems[26] were used in the CEM detector.

- 3 mCi ^{137}Cs source. A motor driver moved the source into the calorimeter module. The signal from the scintillator provided information on radiation damage and the aging of the scintillator.

- A Xenon flash was used for testing the wavelength shifters. The trigger signal passed through a pulse shaping circuit and caused a Xenon bulb to flash. A specially designed optical fiber passed the light into a scintillator rod. The scintillator rod absorbed the light and re-emitted it into the wavelength shifters.

- A Green LED flash was used for calibration of the phototubes. A special construction injects a green LED signal almost directly into the phototube.

The calibration with ^{137}Cs source was performed during the accelerator shut down periods, while the Xenon and LED flash calibrations were carried out about every 20 hours (before the beginning of new TEVATRON run).

The final energy scale for the CEM calorimeter was obtained from electron data sets using the CTC momentum measurement.

In the central region, two hadron calorimeters[27] are used, the Central Hadron Calorimeter (CHA) and the Endwall Hadron Calorimeter (WHA). The CHA and WHA calorimeters cover 360^o in ϕ and -1.32 to 1.32 in η. The CHA is positioned immediately after the CEM but does not cover the entire η range of the later. The WHA calorimeter covers the gap in hadron calorimeters between CHA and Plug. Both CHA and WHA consist of 48 modules. Each module consists of steel-scintillator layers with 2.5 cm sampling for CHA and 5.0 cm sampling for WHA. Each module is divided into projective towers, covering approximately 0.1 unit in η and 15^o in ϕ. There are

24 towers in each η-ring, corresponding to each 15^o slice in ϕ. From these 24 towers, 12 are entirely within the CHA, 6 are within the WHA, and 6 are shared. The towers of the hadronic calorimeters match those of CEM. The size of the towers in $\eta - \phi$ space is fine enough so that the energy of the jets is spread over sufficient number of adjacent towers. The parameters of the CHA and WHA calorimeters are summarized in Table 3.1.

	CHA	WHA
Towers:		
number	384 (8/module)	288 (6/module)
total depth	$4.7\Lambda_{abs}$	$4.5\Lambda_{abs}$
Layers:		
number	32	15
steel thickness	2.5 cm	5.0 cm
scintillator thickness	1.0 cm	1.0 cm
number of phototubes	768	576

Table 3.1: Characteristics of the CHA and WHA calorimeters.

The CHA was designed to have an energy resolution of $\sigma(E)/E = 0.5/\sqrt{E}$ [GeV]. A 2.5 cm sampling was chosen for this calorimeter. A 5.0 cm sampling was chosen for the WHA, since for the same E_t the total energy in the WHA is on average a factor of $\sqrt{2}$ larger than that in the CHA.

The light from the plastic scintillator in the calorimeter towers is collected by wavelength shifter strips, which are positioned along the long side of the scintillator sheets. The light from each tower is collected by two photomultiplier tubes positioned on opposite sides in azimuth.

The angular and longitudinal responses of the modules were made uniform by adjusting the optical properties of the wavelength shifters by placing filters at the couplings between the shifters and the light guides.

Calibration systems were designed for monitoring phototube gains, possible deterio-

ration of scintillators, wavelength shifters and light guides. For the primary system a pulsed laser was used, whose light was diffused and distributed by the optical fibers to the wavelength shifters in front of all photocathods. A backup system used a point-like β source that could be inserted between the light guides and the phototubes. Aging effects could be monitored by inserting the ^{137}Cs source into holes in the scintillator and reading the signal with a read-out system. Studies of uniformity were also performed.

3.2.3 Beam Beam Counters

The measurement of the integrated luminosity is based on the rate of the *minimum bias trigger* generated by the Beam-Beam Counters (BBC)[20]. The BBC counters are two planes of scintillator counters which reside on each side (East and West) of the detector at about 5.8 m from its geometric center. Each plane consists of sixteen "criss-crossed" 1 inch thick scintillator plates and covers the η_D-range of 3.2-5.9.

Signals detected in coincidence from both parts (East and West) of the BBC within a 15 nsec gate centered at 20 nsec after the beam crossing constitute the minimum bias trigger.

The minimum bias trigger does not include events due to collisions between beam particles and the residual gas in the beam pipe, beam halo and events due to cosmic rays.

The integrated luminosity for a run is calculated using the formula

$$\int \mathcal{L}dt = N_{BBC}/\sigma_{p\bar{p}}^{BBC}$$

where N_{BBC} is the number of minimum bias triggers during the run and $\sigma_{p\bar{p}}^{BBC}$ is the total cross section of $p\bar{p}$ interaction, corrected for the BBC acceptance. The measured value of $\sigma_{p\bar{p}}^{BBC}$ is

- 39.9 ± 1.2mb at $\sqrt{s}$=630 GeV
- 51.15 ± 1.60mb at $\sqrt{s}$=1800 GeV

The acceptance of the BBC counters is 0.637 ± 0.022[28], the same at both values of $\sqrt{s}$.

3.2.4 The Trigger System and Data Acquisition

The total $p\bar{p}$ cross section at both $\sqrt{s}$=630 and 1800 GeV is orders of magnitude larger than the cross section of inclusive jet production. A sufficient number of these rare events was collected by increasing the collider intensity and the crossing rates of the beams. Special trigger combinations and a *prescale technique* were used to select events of interest and suppress the number of high rate events written to tape.

The CDF trigger was designed as a three level system[29]. Hadron and electromagnetic calorimeter towers were summed into trigger towers with sizes of $0.2(\eta) \times 15^o(\phi)$, corresponding to an array of 42×24 in $\eta - \phi$ space. The signals from the towers were weighted by $\sin\theta$, so that the trigger threshold was set in units of transverse energy E_t.

The Level 1 calorimeter trigger required the E_t of single trigger towers to be higher than a preset threshold. Level 1 received signals with a rate of about 300 kHz, which required the ability to make a decision within 3.5 μs.

The Level 2 trigger started after the Level 1 accepted the event. Level 2 used the

same 42×24 array of trigger towers and searched for E_t clusters. Towers below a programmable threshold were ignored. A hardware *cluster finder* identified clusters within a time of 200 ns. The energies of all towers in the identified cluster were summed to obtain the total E_t of the cluster and the E_t weighted first and second η and ϕ moments.

In a similar way, the Level 2 trigger identified possible candidates for muon, electron and photon signals.

The Level 3 trigger was the last stage of the on-line trigger system. After Level 2, events were packaged and sent to a farm of 48 Silicon Graphics CPUs, where a FORTRAN reconstruction code including various filtering algorithms was executed.

Since the rates of different processes in $p\bar{p}$ collision differ by orders of magnitude and the total rate of all processes exceeds the ability of the recording system, a prescale is set for a number of processes. This means that only every N^{th} event of a given process (trigger) is written to tape. The number N is the *prescale factor*. This approach allows one to reject a large fraction of frequent events and to record more rare events. On the other hand, a sufficient number of frequent events was still written to tape and was available for reconstruction and statistical analysis of their properties. The prescale factor was recorded for use in the evaluation of the cross section of prescaled events.

The data acquisition (DAQ) at CDF was performed by a multilevel FASTBUS network. At the lowest level of this network data were read from the FASTBUS[31] and RABBIT[32] front end electronic systems, which digitized the analog signals on the output level of the detector components.

FASTBUS is a flexible system with support of both high and low speed devices. Its flexibility and modularity were crucial for the DAQ requirements of CDF. The FAST-

BUS protocol allowed the system to be partitioned so that the data from different detector components could be processed in parallel. FASTBUS was used for the read out from the tracking chambers and trigger system.

The RABBIT system was designed at Fermilab by the Particle Instrumentation Group. It was used at CDF to read out the signals from the calorimetry and muon systems.

Chapter 4

Data Sets.

Inclusive jet data sets collected at the collider energies $\sqrt{s}$=630 and 1800 GeV were used in this analysis. In the following sections, the hardware triggers and event selection criteria are described.

4.1 Inclusive Jet Triggers at $\sqrt{s}$=630 GeV

Two triggers were used in the inclusive jet data collection at $\sqrt{s}$=630 GeV: *Jet_15* and *Jet_5*.

The main trigger, Jet_15, was responsible for the jets with E_t above 30 GeV. This trigger had the following requirements:

- Jet $E_t \geq 15$ GeV
- E_t of the electromagnetic component (EM) of the jet ≥ 0.5 GeV

Data selected with Jet_5 trigger were used in this analysis for the measurement of the cross section in E_t bins of 20-25 GeV and 25-30 GeV. Because the inclusive jet

spectrum rises exponentially towards low transverse energies, the Jet_5 trigger was dynamically[1] prescaled. The requirements for Jet_5 trigger were:

- Level 2 L2_4_BBC trigger (where the dynamic prescale was set)
- Jet $E_t \geq 5$ GeV

The L2_4_BBC trigger was based on the requirement of a single tower in the Central calorimeter with E_t above 4 GeV and a coincidence in the West and East BBC counters.

A study was performed to evaluate the trigger efficiency as a function of jet E_t. The efficiencies of the Jet_5 and Jet_15 triggers were estimated from the Minimum Bias and Jet_5 samples respectively as a ratio

$$\epsilon = M_{trig}/M_{tot},$$

where M_{trig} is the number of events in the parent sample which passed the trigger requirement for the E_t of the leading cluster:

- $E_t^{L2} > 5$ GeV for Jet_5 trigger
- $E_t^{L2} > 15$ GeV for Jet_15 trigger,

M_{tot} is the total number of events in the parent sample.

The uncertainty on the efficiency was calculated as[2]

$$\delta\epsilon = \sqrt{\frac{\epsilon(1-\epsilon)}{M_{tot}-1}}.$$

[1]The value of the prescale parameter varied in the range 100 to 600 depending on the instantaneous luminosity of the TEVATRON. The average prescale factor over the entire Data set was 151.3.

[2]For the trigger efficiency of 100%, the uncertainties are 68% C.L. intervals obtained from binomial statistics.

Jet_5 trigger (Min. Bias sample)			
Jet E_t	M_{trig}	M_{tot}	$\epsilon(\%)$
6.28	4130	41216	10.02 ± 0.15
11.60	742	1831	40.52 ± 1.15
16.83	159	208	76.44 ± 2.95
22.13	40	42	95.24 ± 3.33
27.13	6	6	$100\ ^{+0.00}_{-26.37}$
31.60	4	4	$100\ ^{+0.00}_{-36.72}$
37.38	2	2	$100\ ^{+0.00}_{-59.96}$
Jet_15 trigger (Jet_5 sample)			
Jet E_t	M_{trig}	M_{tot}	$\epsilon(\%)$
6.92	2158	110767	1.95 ± 0.04
11.97	819	25963	3.15 ± 0.11
17.00	1085	7275	14.91 ± 0.42
22.05	1350	2165	62.36 ± 1.04
27.04	653	766	85.25 ± 1.28
32.04	257	268	95.90 ± 1.21
36.96	110	115	95.65 ± 1.91
41.65	47	47	$100\ ^{+0.00}_{-3.83}$
46.81	25	25	$100\ ^{+0.00}_{-7.08}$
53.09	8	8	$100\ ^{+0.00}_{-20.51}$
57.85	7	7	$100\ ^{+0.00}_{-23.05}$

Table 4.1: Jet_5 and Jet_15 trigger efficiencies. The uncertainties on points with 100% efficiency are 68% C.L. intervals obtained from binomial statistics.

The values of Jet_5 and Jet_15 trigger efficiencies are given in Table 4.1 and plotted in Figure 4.1. The triggers with the corresponding prescale factors and jet E_t bins they contributed to are listed in Table 4.2.

4.2 Inclusive Jet Triggers at $\sqrt{s}$=1800 GeV

The inclusive jet data at $\sqrt{s}$=1800 GeV cover the jet E_t range 40-440 GeV. This E_t range approximately corresponds to the same x_t range which is covered by the inclusive jet data at $\sqrt{s}$=630 GeV.

Data at $\sqrt{s}$=1800 GeV were collected with four triggers: *Jet_100*, *Jet_70*, *Jet_50* and *Jet_20*. These triggers were based on the following requirements:

- Jet_100 was the main trigger at 1800 GeV. This trigger required at least one jet with E_t >100 GeV. The trigger was not prescaled.

- Jet_70 trigger required at least one jet with E_t >70 GeV. This trigger was prescaled by 8 at Level 2.

- Jet_50 trigger required at least one jet with E_t >50 GeV. This trigger was based on Level 1 L1_4_PRESCALE_40 trigger, which required single tower with energy in CEM and CHA calorimeters above 4 GeV. The L1_4_PRESCALE_40 trigger was prescaled by 40, so the prescale parameter for Jet_50 was also 40.

- Jet_20 trigger required at least one jet with E_t >20 GeV. This trigger was prescaled twice- the Level 2 prescale factor was 25. The Level 1 L1_4_PRESCALE_40 trigger was also required. This made the combined prescale factor of Jet_20 trigger equal to $25 \times 40 = 1000$.

Table 4.2 lists the triggers, prescale factors and the corresponding jet E_t bins in the data set.

4.3 Event Selection

The data samples contained events that passed the trigger requirements. However the triggers could also be activated by events that do not contain information valuable for this study and should not be used in the analysis. These events were rejected by the following additional cuts:

- The COSFLT filter rejects non-$p\bar{p}$ collision events, the ones originated by cosmic ray muons or by interactions of beam particles with the beam pipe. This filter rejects events that are out of time with respect to the beam crossing time marker and have out of time energy above 8 GeV.

- The following two cuts reject non-$p\bar{p}$ collision events that are not rejected by COSFLT.

  - $E_{tot} < \sqrt{s}$
  - $\not{E}_t/\sqrt{\sum E_t}$ <6

- $|Z_{vtx}| < 60$ cm. The events with a large offset of the vertex from the center of the detector were rejected. However they could activate the Minimum Bias trigger and the BBC counters, which means that these events could be included in the integrated luminosity (see 3.2.3, 4.4) and affect the measured cross section.
  In order to make a correction for this cut, the fraction of events with large vertex offset was estimated by fitting the Z_{vtx} distribution in Minimum Bias sample

by the beam profile distribution. The corresponding corrections for both data sets are given in Table 4.2.

- $0.1 < |\eta_D| < 0.7$ - only central jets are used in the analysis, the jets outside this η_D range were not counted. This η_D range was chosen so that jets were confined to central calorimeters and away from the crack at $\theta = 90^o$, where the jet energy resolution is good.

4.4 Integrated Luminosity

The integrated luminosity (defined in 3.1) was measured for all runs. The total integrated luminosity was calculated as a sum over the runs, contributing to the inclusive jet data sets.

The values of the integrated luminosities, prescale factors and Z_{vtx} cut corrections are shown in Table 4.2.

Different triggers contributed to different E_t ranges. This means that the prescale factors corresponding to these E_t ranges may vary. Since the raw cross sections were evaluated for every E_t bin individually (see 4.5), the corrections for the Z_{vtx} cut can also be applied to the integrated luminosity: $\int \mathcal{L}dt \to \int \mathcal{L}dt \cdot (\epsilon_{Z_{vtx}}/f_{PS})$.

4.5 Raw Cross Section

At both center of mass energies, the double differential inclusive jet cross section, averaged over the η-range $0.1 < |\eta| < 0.7$, was calculated according to the formula:

$$\frac{1}{\Delta\eta}\int d\eta \frac{d\sigma}{dE_t d\eta} = \frac{1}{\Delta\eta} \cdot \frac{1}{\int \mathcal{L}dt} \cdot \frac{N_{jet}/\epsilon}{\Delta E_t},$$

$\sqrt{s}$	$\int \mathcal{L}dt$	$\epsilon_{Z_{vtx}}$	Trigger	f_{PS}	E_t-range
630	$570nb^{-1}$	0.84			
			Jet_5	151.3	20-30
			Jet_15	1.0	30-140
1800	$88.77pb^{-1}$	0.92			
			Jet_20	1000	40- 75
			Jet_50	40	75-100
			Jet_70	8	100-130
			Jet_100	1	130-440

Table 4.2: For two data sets, the integrated luminosities are presented. Z_{vtx} cut corrections are based on the information on the beam profile. The triggers are listed with the corresponding prescale factors and jet E_t bins they contributed to. The prescale factors and the Z_{vtx} cut corrections should be applied as overall corrections to the integrated luminosities for both data sets.

where N_{jet}/ϵ is the number of jets in the bin of width ΔE_t corrected for the trigger efficiency ϵ, $\int \mathcal{L}dt$ is the effective integrated luminosity after including prescale and Z_{vtx} cut corrections, and $\Delta\eta$=1.2 is the η range used in the analysis. The statistical uncertainty on the cross section was calculated as:

$$\delta\left(\frac{d^2\sigma}{dE_t d\eta}\right) = \frac{\delta\left(N_{jet}/\epsilon\right)}{\int \mathcal{L}dt \Delta E_t \Delta\eta} =$$

$$\frac{d^2\sigma}{dE_t d\eta} \cdot \sqrt{\left(\delta N_{jet}/N_{jet}\right)^2 + \left(\delta\epsilon/\epsilon\right)^2}.$$

The uncertainty on the luminosity was common to all data points and was treated separately.

The raw inclusive jet cross sections measured at $\sqrt{s}$=630 and 1800 GeV are given in Tables 4.3 and 4.4 and are plotted in Figure 4.2. They should be corrected for the effects of energy degradation in the calorimeter and finite resolution of the detector before comparison with the QCD predictions.

	E_t bin GeV	$< E_t >$ GeV	#-of-jets	$d^2\sigma/dE_t d\eta$ nb/GeV	$\delta(d^2\sigma/dE_t d\eta)$ nb/GeV
Jet_5					
1	20-25	22.0	2165	0.118E+03	0.486E+01
2	25-30	27.0	766	0.399E+02	0.144E+01
Jet_15					
3	30-35	32.2	36363	0.131E+02	0.179E+00
4	35-40	37.1	17010	0.613E+01	0.131E+00
5	40-45	42.2	7600	0.262E+01	0.300E-01
6	45-50	47.2	3692	0.127E+01	0.209E-01
7	50-55	52.2	1883	0.649E+00	0.149E-01
8	55-60	57.3	1041	0.359E+00	0.111E-01
9	60-65	62.3	560	0.193E+00	0.815E-02
10	65-70	67.3	306	0.105E+00	0.603E-02
11	70-75	72.4	156	0.537E-01	0.430E-02
12	75-80	77.3	97	0.334E-01	0.339E-02
13	80-85	82.2	68	0.234E-01	0.284E-02
14	85-90	87.3	44	0.152E-01	0.228E-02
15	90-100	94.3	30	0.517E-02	0.943E-03
16	100-115	106.1	22	0.253E-02	0.539E-03
17	115-145	122.9	7	0.402E-03	0.151E-03

Table 4.3: Raw cross section at $\sqrt{s}$=630 GeV, combined from Jet_5 and Jet_15 trigger samples.

	E_t-bin GeV	$< E_t >$ GeV	#-of-jets	$d^2\sigma/dE_t d\eta$ nb/GeV	$\delta(d^2\sigma/dE_t d\eta)$ nb/GeV
Jet_20					
1	40-45	42.26	22621	0.469E+02	0.132E+01
2	45-50	47.26	12277	0.246E+02	0.608E+00
3	50-55	52.27	7083	0.140E+02	0.324E+00
4	55-60	57.30	4046	0.794E+01	0.189E+00
5	60-65	62.34	2431	0.476E+01	0.127E+00
6	65-70	67.33	1655	0.323E+01	0.969E-01
7	70-75	72.39	1062	0.207E+01	0.729E-01
Jet_50					
8	75-80	77.34	16819	0.142E+01	0.189E-01
9	80-85	82.36	11609	0.948E+00	0.128E-01
10	85-90	87.36	8330	0.677E+00	0.916E-02
11	90-90	92.39	5897	0.478E+00	0.764E-02
12	95-100	97.34	4368	0.353E+00	0.624E-02
Jet_70					
13	100-105	102.38	15097	0.256E+00	0.290E-02
14	105-110	107.38	11151	0.186E+00	0.228E-02
15	110-115	112.36	8501	0.141E+00	0.186E-02
16	115-120	117.40	6541	0.108E+00	0.157E-02
17	120-125	122.35	4980	0.823E-01	0.132E-02
18	125-130	127.40	3748	0.618E-01	0.111E-02
Jet_100					
19	130-140	134.57	43006	0.435E-01	0.302E-03
20	140-150	144.58	25970	0.263E-01	0.163E-03
21	150-160	154.61	16486	0.167E-01	0.130E-03
22	160-170	164.63	10650	0.108E-01	0.104E-03
23	170-180	174.65	7055	0.714E-02	0.850E-04
24	180-190	184.64	4804	0.486E-02	0.701E-04
25	190-200	194.69	3178	0.321E-02	0.570E-04
26	200-220	208.78	3527	0.178E-02	0.300E-04
27	220-240	228.79	1746	0.883E-03	0.211E-04
28	240-260	248.92	957	0.484E-03	0.156E-04
29	260-280	268.92	416	0.210E-03	0.103E-04
30	280-300	288.98	202	0.102E-03	0.719E-05
31	300-320	309.32	116	0.587E-04	0.545E-05
32	320-360	336.10	100	0.253E-04	0.253E-05
33	360-440	385.46	31	0.392E-05	0.704E-06

Table 4.4: Raw cross section at $\sqrt{s}$= 1800 GeV

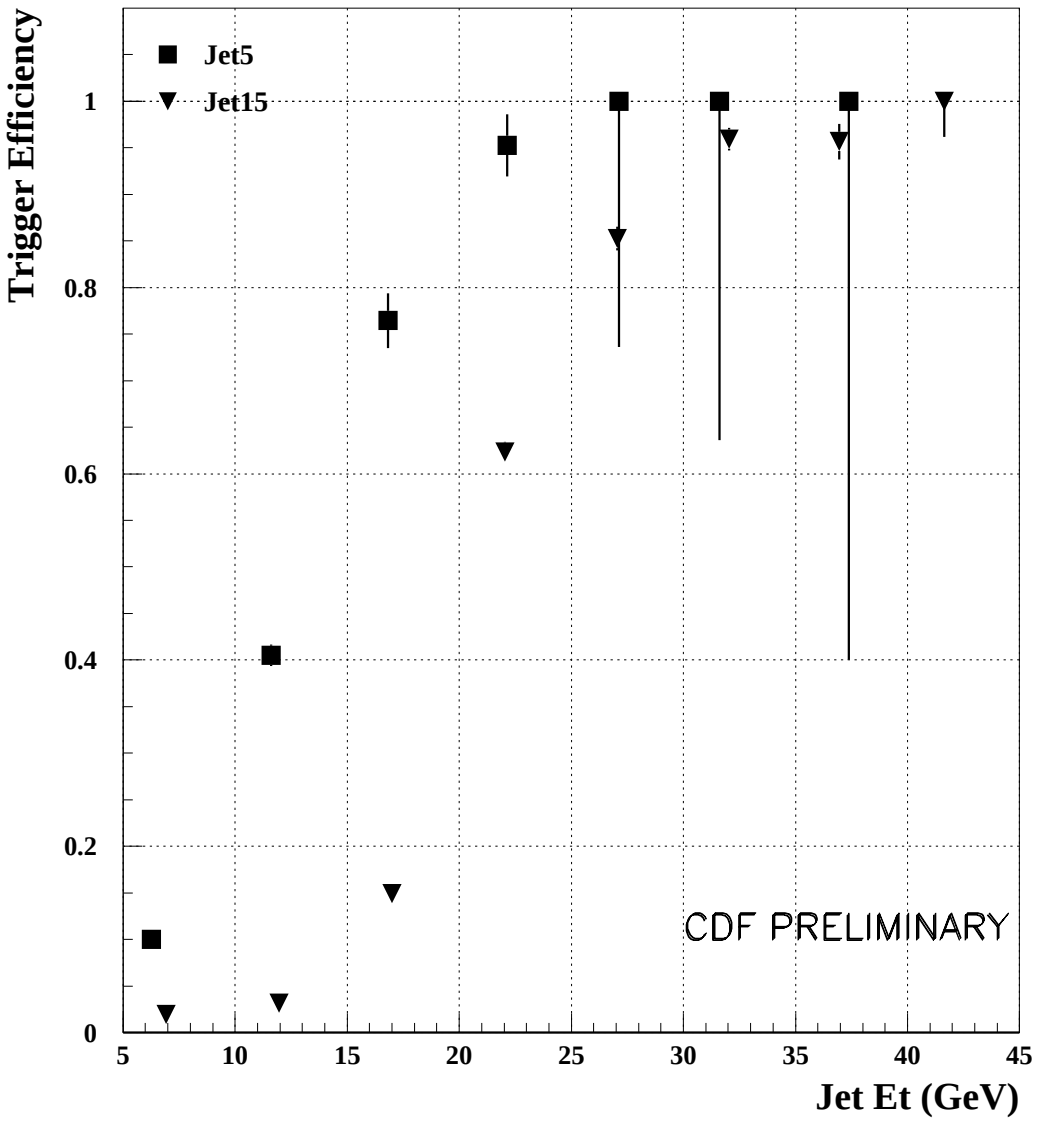

Figure 4.1: Efficiencies of the Jet_5 and Jet_15 inclusive jet triggers. For the trigger efficiency of 100%, the uncertainties are 68% C.L. intervals obtained from binomial statistics.

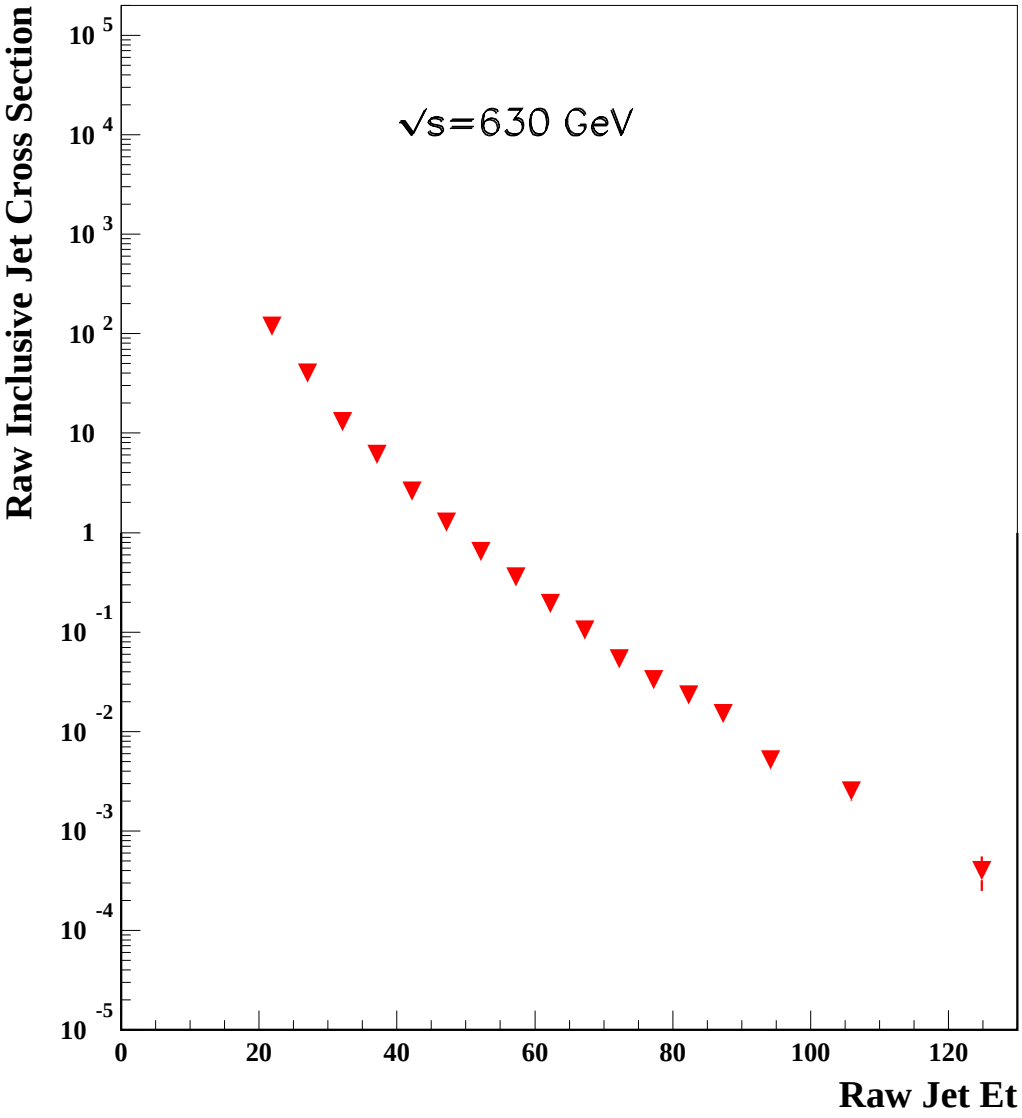

Figure 4.2: Raw inclusive jet cross section measured at $\sqrt{s}$=630.

Chapter 5

Correction for Detector Effects. The Corrected Cross Section.

The spectrum of the jets *measured* by the detector differs from the spectrum of the *true* jets which emerge from the hadron-hadron interaction due to the energy degradation of the particles in the detector. This results in the different transverse energy measured within the cone surrounding the jet axis. The theoretical predictions, on the other hand, do not take into account the detector effects. Correction for the detector effects is needed so that experimentally observed spectra (cross-section) can be compared with the theoretical predictions and measurements by other experiments.

The jet spectrum correction procedure employed by CDF, called *unsmearing*[33], is a fitting procedure, which uses the parameterized detector response function. The response function ($\mathcal{RF}$) of the detector is the probability that a true jet with transverse energy E_t^{true} will be measured as a jet with transverse energy E_t^{meas} in CDF detector.

The convolution of the true jet spectrum with the response function yields the spectrum of measured jets:

$$\sigma(E_t^{meas}) = \int \sigma_{tr}(E_t^{true})\mathcal{RF}(E_t^{true}, E_t^{meas})dE_t^{true}.$$

To extract the true spectrum from the measured one, the ture spectrum was parameterized and the parameters were tuned to obtain reasonable agreement between the measured spectrum and the convolution described by the above equation.

5.1 Detector Response Functions

The response of the detector to certain particles of a given energy can be obtained directly from *test beam* measurements by exposing the detector to monoenergetic beams of particles; however, this can not be done for jets.

A two-stage Monte Carlo simulation was used to extract the detector response to jets:

- The fragmentation simulation. A phenomenological fragmentation model was tuned to reproduce the charged particle spectra in experimentally observed jets.
- The detector simulation. The detector response to every particle in a jet was evaluated. The resulting tower energies were passed through the jet reconstruction algorithm so that the simulated jets were reconstructed in the same way as in the measured events.

Since the tuning of the fragmentation itself relied on the detector simulation, the following paragraphs describe the detector simulation first and then the fragmentation and the derived $\mathcal{RF}$.

The QFL package[34] was used for detector simulation. It is based on parameterization of the detector response to single particle rather than direct simulation of the

energy losses by a particle traversing the active media of the detector. The response to single particle was tuned with test beam and single tracks in $p\bar{p}$ collision data at CDF.

Outputs of event generators were passed through the QFL package. The responses of relevant detector components were then calculated and the results were stored in the same format as the real measured data. The JETCLU jet clustering algorithm was used for the reconstruction of the jets. If the properties of simulated jets are close to those of real jets, this approach provides the best correspondence between true and measured jets.

The distribution of the parent parton's energy among the daughter hadrons is governed by the fragmentation process. The exact nature of the fragmentation is not completely understood, however a phenomenological model was used to convert a parton of given energy into hadrons. The SETPRT module[35], developed at CDF, fragmented the parton outgoing from the interaction. The tracking system of CDF was used to study the spectra of charged particles associated with the observed jets and jets simulated with SETPRT. The parameters of the fragmentation model were tuned to reproduce the following variables, observed in data:

- The number of tracks pointing inside the jet cone (measure of the charged particle multiplicity).
- $P_{\perp}$, the component of the track momentum perpendicular to the jet axis.
- P_t (relative to the beam axis) of the tracks pointing inside the jet cone.
- The number of tracks pointing inside a cone (with $(\eta - \phi)$ size of 0.7) perpendicular in ϕ to the jet axis. This is a measure of the Underlying Event multiplicity.

- $P_{\perp}^{90}$, the momentum of tracks in a cone perpendicular to the jet axis: $\phi_{\perp}^{90} = \phi^{jet} + 90^{o}$.

- P_t (relative to the beam axis) of the tracks pointing inside the cone perpendicular to the jet.

- The P_t flow: $\Delta\phi$ between a track and the jet axis weighted by the P_t of the track, for tracks pointing inside the jet cone.

- The P_t loss flow: $\Delta\phi$ between the track and the jet axis weighted by the P_t lost by the track due to the non-linearity of the central hadron calorimeter.

- Energy Loss: the amount of the jet energy lost due to the non-linearity of the central hadron calorimeter.

Using these parameters, the fragmentation in SETPRT was tuned to agree with the observations in the 1988-1989 CDF jet data, over the whole jet E_t range. The SETPRT+QFL model provided the correspondence between the measured jet E_t^{meas} and the true (before QFL) jet E_t^{true}. The distributions of E_t^{meas} for a fixed value of E_t^{true}, $\mathcal{D}_{E_t^{true}}(E_t^{meas})$, were normalized in order to obtain the $\mathcal{RF}$:

$$\mathcal{RF}(E_t^{true}, E_t^{meas}) = \frac{\mathcal{D}_{E_t^{true}}(E_t^{meas})}{\int \mathcal{D}_{E_t^{true}}(E_t^{meas}) dE_t^{meas}}$$

The $\mathcal{RF}$ at each value of E_t^{true} was fitted with a four-parameter function describing the mean, width and the exponential tails. Figure 5.1 presents the $\mathcal{RF}(E_t^{true}, E_t^{meas})$ for three values of E_t^{true}.

The $\mathcal{RF}$ depends on two factors: the energy spectrum of hadrons within the jet (fragmentation) and the response of the detector to a single hadron. The $\mathcal{RF}$ obtained using SETPRT+QFL corresponds to jets produced at $\sqrt{s}$=1800 GeV. The same $\mathcal{RF}$

was used to unsmear the inclusive jet cross section measured at $\sqrt{s}$=630 GeV. The study of the fragmentation dependence on the center of mass energy is described in Chapter 6. It is shown that the detector response to same E_t jets does not depend on $\sqrt{s}$ and that the same $\mathcal{RF}$ can be used for both data sets.

5.2 Unsmearing

The unsmearing procedure consisted of three stages:

- The choice of an initial parameterization to represent the unknown true cross section as a function of true jet E_t^{true}.
- The convolution of the parameterized true cross section with the detector $\mathcal{RF}$. The resulting *smeared* cross section was compared with the measured cross section.
- The optimization of the parameters of the true cross section until a reasonable agreement between the smeared and measured cross sections was achieved.

The true cross section was parameterized as follows:

$$\frac{d^2\sigma}{dE_t^{true}d\eta} = p_0(1-2E_t^{true}/\sqrt{s})^{p_6}\cdot 10^{\sum_{i=1,5} p_i(\lg E_t^{true})^i} \equiv \mathcal{F}(E_t^{true}),$$

where E_t^{true} was the true jet E_t and $p_0, ..., p_6$ were the parameters to be optimized. For every measured E_t bin, the smeared cross section was calculated as:

$$\langle\frac{d^2\sigma^{smr}}{dE_t^{meas}d\eta}\rangle_{bin} = \frac{1}{E_t^{high}-E_t^{low}}\cdot\int_{E_t^{low}}^{E_t^{high}} dE_t^{meas}\int_{5GeV}^{E_t^{max}} dE_t^{true}\mathcal{RF}(E_t^{true},E_t^{meas})\mathcal{F}(E_t^{true}),$$

where E_t^{low} and E_t^{high} are the lower and upper limits of the E_t^{meas} bin; the inner integral is the smeared cross section as a function of E_t^{meas}: $d^2\sigma^{smr}/dE_t^{meas}d\eta$; and

the outer integral evaluates the average of the smeared cross section over the width of the E_t bin. In the inner integral, the upper limit of integration, E_t^{max} is set to 200 GeV for $\sqrt{s}$=630 GeV data, and 600 GeV for $\sqrt{s}$=1800 GeV data. The smeared cross section was compared with the experimentally measured raw cross section. This procedure was repeated to minimize

$$\chi^2 = \sum_i \left((\sigma^{smeared} - \sigma^{measured}) / \delta\sigma^{measured} \right)^2 ,$$

where $\sigma \equiv d^2\sigma / dE_t d\eta$.

The minimization of the χ^2 function was performed by the MINUIT package[37]. The functional form with optimized parameters represented the corrected cross section; it is referred to as the *physics curve*, $\mathcal{F}(E_t^{true}) = d^2\sigma^{true}/dE_t^{true}d\eta$. The fractional *residual of the unsmearing*,

$$(\sigma^{measured} - \sigma^{smeared})/\sigma^{smeared}$$

is presented in Figure 5.2 and in Table 5.1. The error on the fractional residual was calculated as

$$\delta \left((\sigma^{measured} - \sigma^{smeared})/\sigma^{smeared} \right) = \delta\sigma^{measured}/\sigma^{smeared},$$

where σ is again the double differential cross section. The large value of χ^2/ndf (3.15) can be traced to the 2^{nd}, 3^{rd} and 4^{th} points, which have very small statistical errors. Increasing the errors by a factor of 2 resulted in better value of χ^2/ndf (to 1.8) but did not change the parameters of the best fit significantly. The found minimum of the χ^2 functional is stable.

The same distribution for data measured at $\sqrt{s}$=1800 GeV is presented in Figure 5.3; the corresponding value of χ^2/ndf is 1.69. The physics curve obtained for each center

of mass energy was used to correct the measured cross section. For every measured E_t bin the following variables were calculated:

$$E_t(M) = \frac{\int_l^h dE_t^{meas} \int_{5GeV}^{E_t^{max}} dE_t^{true} E_t^{meas} \mathcal{RF}(E_t^{true}, E_t^{meas}) \mathcal{F}(E_t^{true})}{\int_l^h dE_t^{meas} \int_{5GeV}^{E_t^{max}} dE_t^{true} \mathcal{RF}(E_t^{true}, E_t^{meas}) \mathcal{F}(E_t^{true})}$$

and

$$E_t(T) = \frac{\int_l^h dE_t^{meas} \int_{5GeV}^{E_t^{max}} dE_t^{true} E_t^{true} \mathcal{RF}(E_t^{true}, E_t^{meas}) \mathcal{F}(E_t^{true})}{\int_l^h dE_t^{meas} \int_{5GeV}^{E_t^{max}} dE_t^{true} \mathcal{RF}(E_t^{true}, E_t^{meas}) \mathcal{F}(E_t^{true})},$$

where indices l and h mean the lower and upper E_t limits of the measured E_t bin; E_t^{max} is set to 200 GeV for $\sqrt{s}$=630 GeV data, and to 600 GeV for $\sqrt{s}$=1800 GeV. $E_t(T)$ is the average value of E_t^{true} contributing to the given measured bin; $E_t(M)$ is the predicted average measured E_t^{meas} in the bin. The corrected jet E_t is defined as:

$$E_t^{corrected} = \frac{E_t(T)}{E_t(M)} \cdot E_t^{measured}.$$

For every bin, the ratio of the physics curve to the smeared cross section (smeared physics curve) was the estimate of the cross section correction. The cross section corrected for detector effects is given by

$$\frac{d^2\sigma^{corr}}{dE_t d\eta} = \mathcal{F}(E_t^{corrected}) \cdot \frac{< d^2\sigma^{measured}/dE_t d\eta >_{bin}}{< d^2\sigma^{smeared}/dE_t d\eta >_{bin}}.$$

This corrected cross section can be directly compared with theoretical predictions at $E_t^{corrected}$.

5.3 The Corrected Cross Section

The corrected cross section at $\sqrt{s}$=630 GeV is presented in Table 5.2 and Figures 5.4 and 5.5 with the inclusive jet cross section measured at $\sqrt{s}$=1800 GeV;

	E_t-bin	$\sigma^{smeared}$	$\sigma^{measured}$	$\delta\sigma^{measured}$	$\frac{(\sigma^{measured}-\sigma^{smeared})}{\sigma^{smeared}}(\%)$
1	20-25	0.1225E+03	0.1185E+03	0.4858E+01	-3.27± 3.97
2	25-30	0.3595E+02	0.3992E+02	0.1442E+01	11.05± 4.01
3	30-35	0.1343E+02	0.1306E+02	0.1790E+00	-2.75± 1.33
4	35-40	0.5704E+01	0.6126E+01	0.1310E+00	7.39± 2.30
5	40-45	0.2628E+01	0.2618E+01	0.3003E-01	-0.38± 1.14
6	45-50	0.1283E+01	0.1272E+01	0.2093E-01	-0.85± 1.63
7	50-55	0.6544E+00	0.6486E+00	0.1495E-01	-0.89± 2.28
8	55-60	0.3460E+00	0.3586E+00	0.1111E-01	3.65± 3.21
9	60-65	0.1884E+00	0.1929E+00	0.8152E-02	2.39± 4.33
10	65-70	0.1052E+00	0.1054E+00	0.6026E-02	0.17± 5.73
11	70-75	0.6012E-01	0.5374E-01	0.4302E-02	-10.61± 7.16
12	75-80	0.3505E-01	0.3341E-01	0.3393E-02	-4.67± 9.68
13	80-85	0.2082E-01	0.2342E-01	0.2841E-02	12.52± 13.64
14	85-90	0.1258E-01	0.1516E-01	0.2285E-02	20.46± 18.16
15	90-100	0.6281E-02	0.5167E-02	0.9434E-03	-17.73± 15.02
16	100-115	0.2107E-02	0.2526E-02	0.5386E-03	19.88± 25.56
17	115-145	0.4053E-03	0.4019E-03	0.1519E-03	-0.85± 37.47

Table 5.1: The smeared true cross section, measured raw cross section, the statistical error on measured cross section, and the fractional residual of the unsmearing at $\sqrt{s}$=630 GeV.

the cross sections are plotted versus jet E_t and x_t. Comparison with EKS NLO QCD predictions (CTEQ4M as pdf set) is shown in Figures 5.6 and 5.7. Figure 5.8 presents comparison of the corrected cross section with EKS NLO QCD calculations at $\sqrt{s}$=630 GeV for different sets of pdf. At $\sqrt{s}$=1800 GeV, data are consistent with QCD predictions at low E_t, while at $\sqrt{s}$=630 GeV, a discrepancy with QCD at low E_t is observed.

$< E_t^{corr} >$	$d^2\sigma^{corr}/dE_t d\eta$	$\delta(d^2\sigma^{corr}/dE_t d\eta)$	σ-corr.	E_t-corr.
21.5	0.194E+03	0.797E+01	1.6404	0.9822
28.5	0.521E+02	0.188E+01	1.3044	1.0545
34.7	0.159E+02	0.217E+00	1.2137	1.0808
40.5	0.728E+01	0.156E+00	1.1890	1.0909
46.2	0.310E+01	0.356E-01	1.1848	1.0948
51.7	0.151E+01	0.249E-01	1.1887	1.0961
57.2	0.776E+00	0.179E-01	1.1961	1.0958
62.6	0.432E+00	0.134E-01	1.2053	1.0948
68.0	0.234E+00	0.990E-02	1.2150	1.0934
73.4	0.129E+00	0.738E-02	1.2245	1.0917
78.5	0.663E-01	0.531E-02	1.2333	1.0899
84.1	0.415E-01	0.421E-02	1.2411	1.0881
89.4	0.292E-01	0.354E-02	1.2476	1.0864
94.7	0.190E-01	0.286E-02	1.2526	1.0848
102.0	0.666E-02	0.122E-02	1.2882	1.0829
114.4	0.334E-02	0.713E-03	1.3239	1.0804
134.7	0.572E-03	0.216E-03	1.4243	1.0792

Table 5.2: Corrected Cross Section at $\sqrt{s}$=630 GeV.

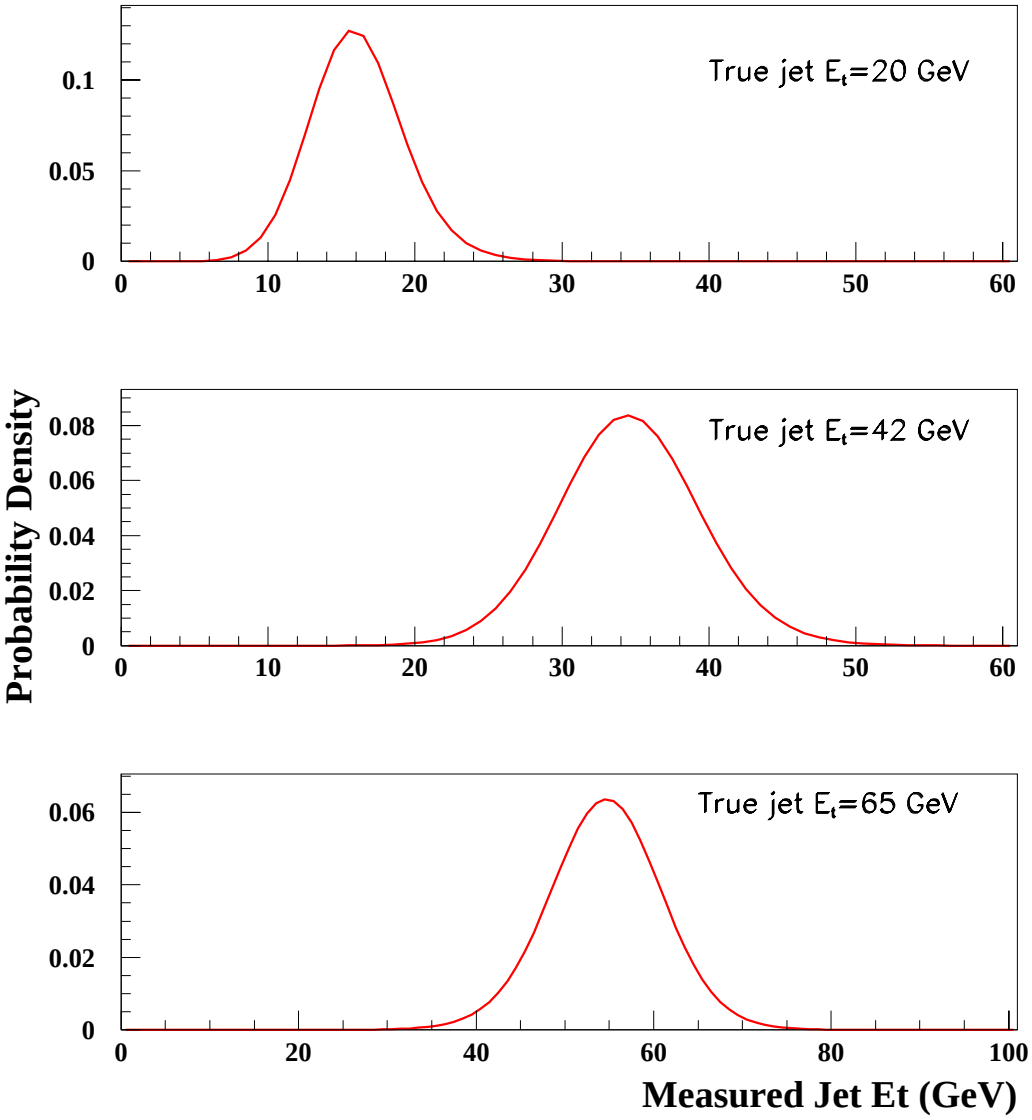

Figure 5.1: The CDF response function.

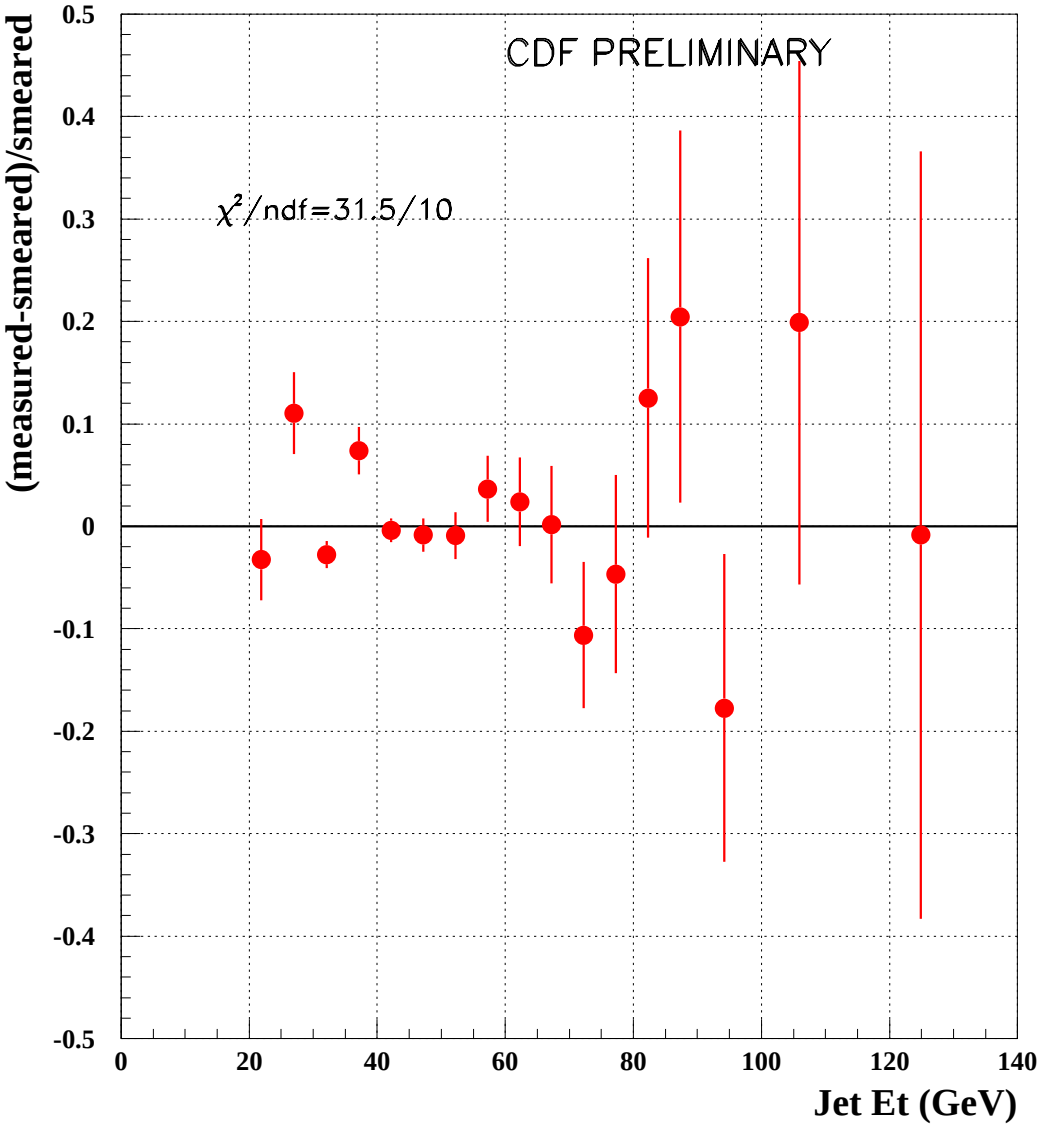

Figure 5.2: The residual of unsmearing at $\sqrt{s}$=630 GeV. The large value of χ^2 is due to very small statistical errors on 2^{nd},3^{rd},4^{th} points.

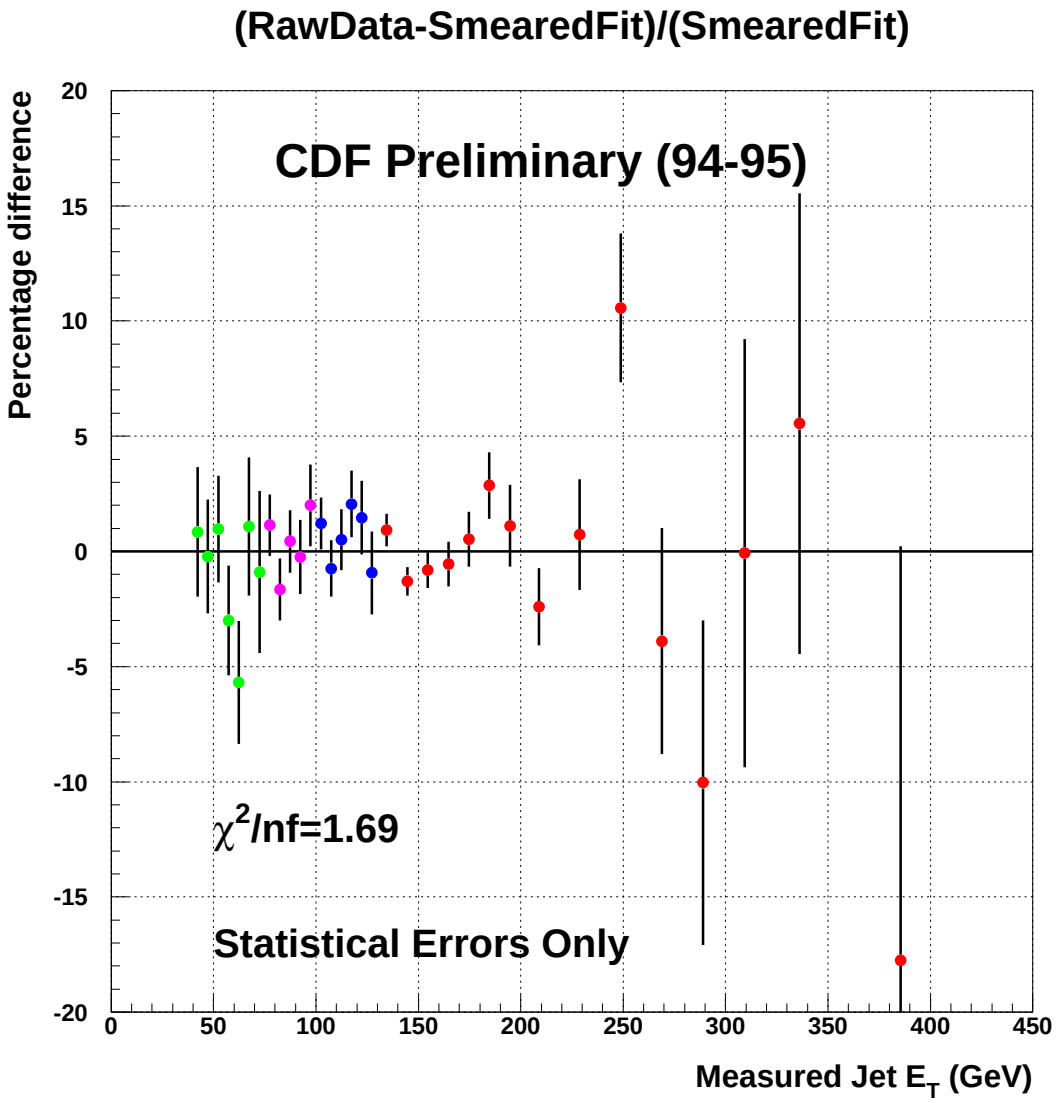

Figure 5.3: The residual of unsmearing at $\sqrt{s}$=1800 GeV.

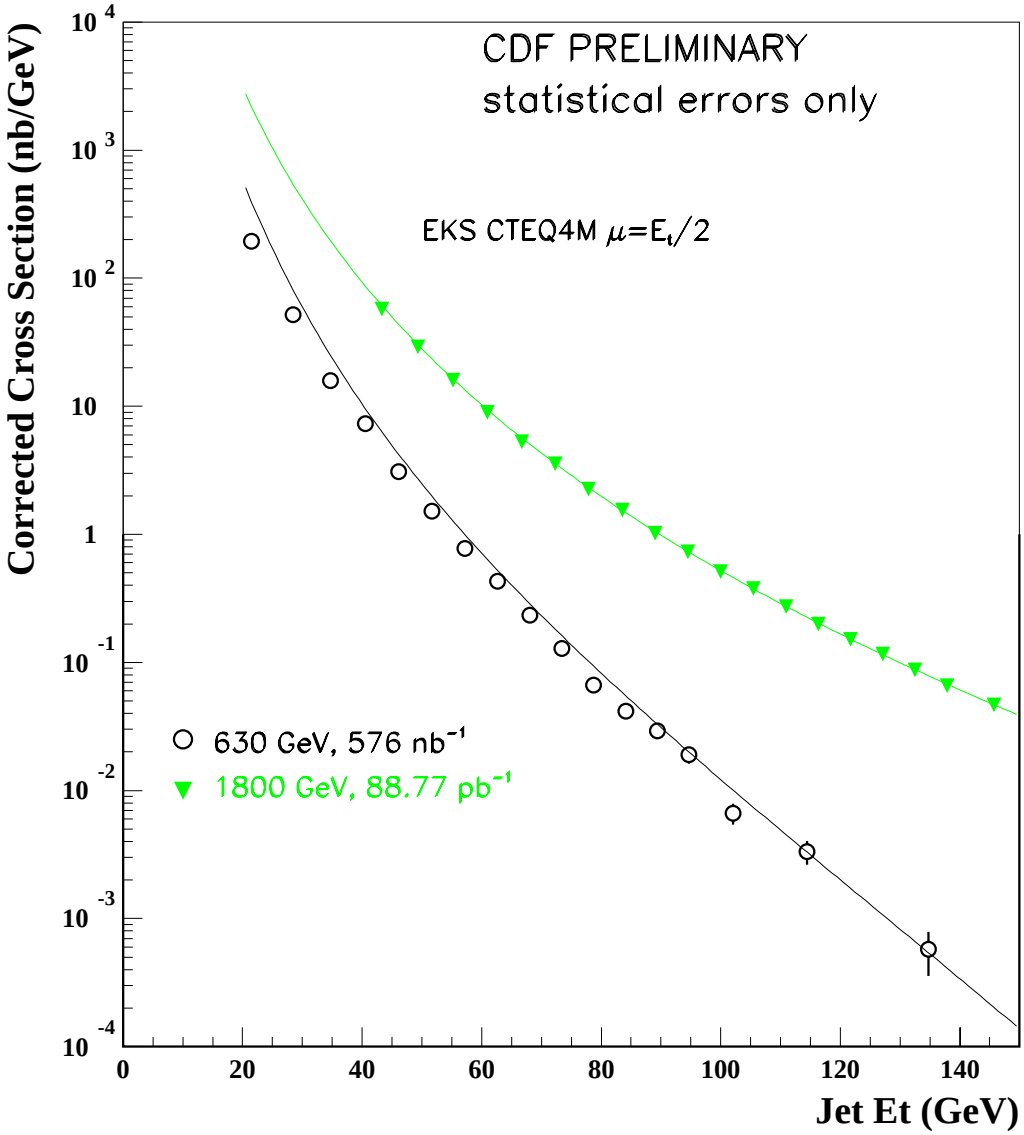

Figure 5.4: The corrected inclusive jet cross sections measured at $\sqrt{s}$=630 and 1800 GeV versus jet E_t. Data are compared to NLO QCD predictions.

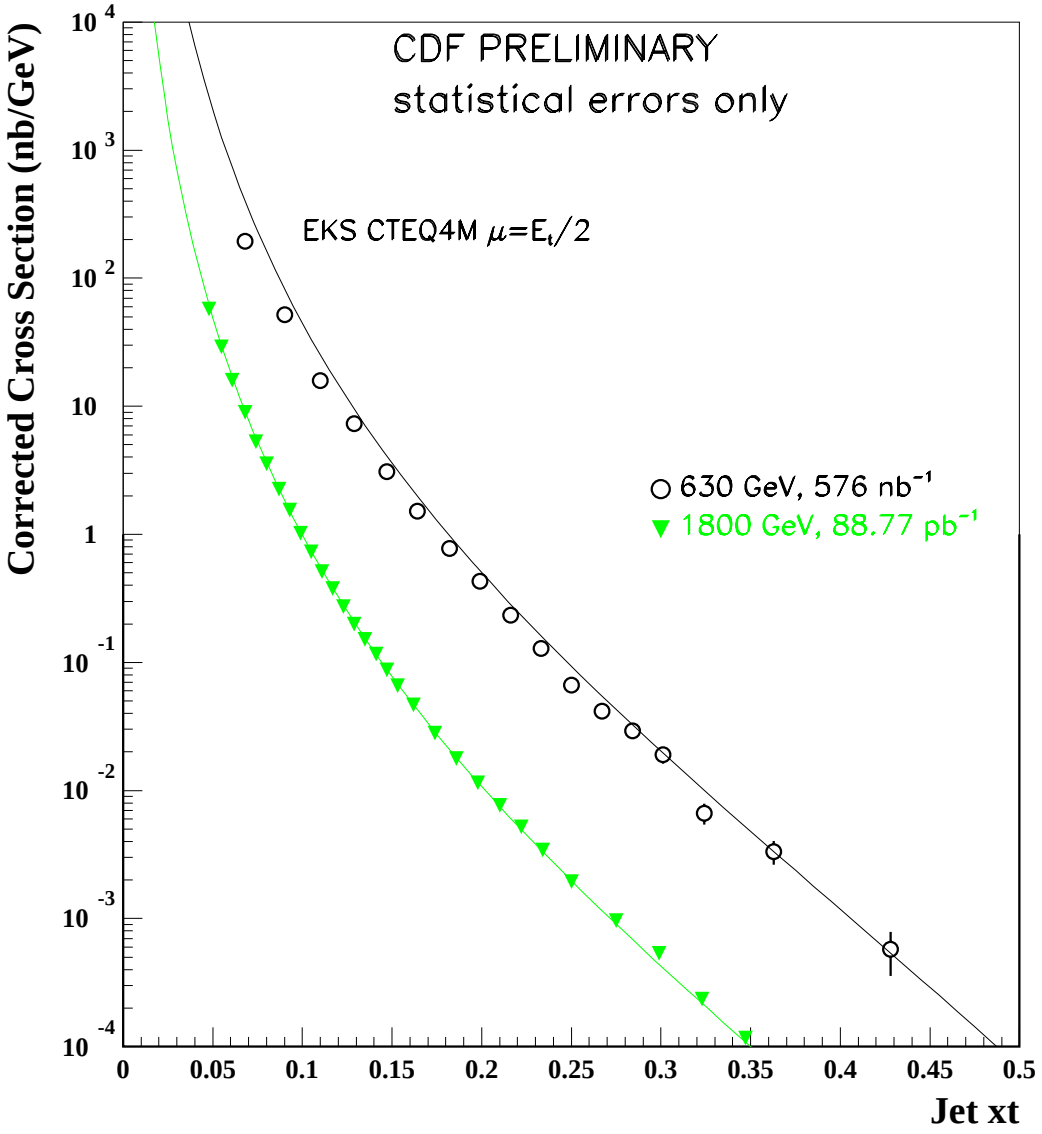

Figure 5.5: The corrected inclusive jet cross sections measured at $\sqrt{s}$=630 and 1800 GeV versus jet x_t.

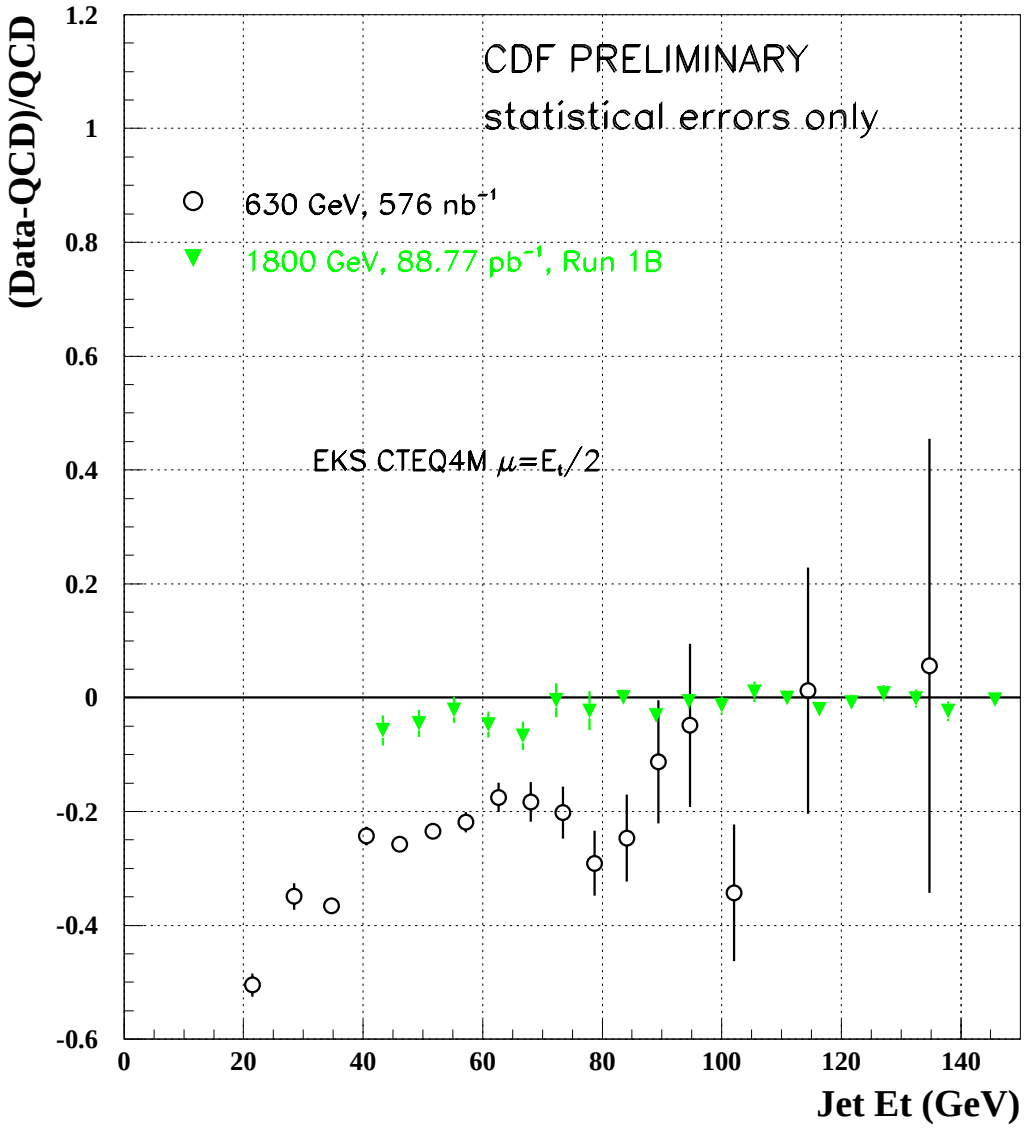

Figure 5.6: (Data-Theory)/Theory comparison with NLO QCD predictions at $\sqrt{s}$=630 and 1800 GeV.

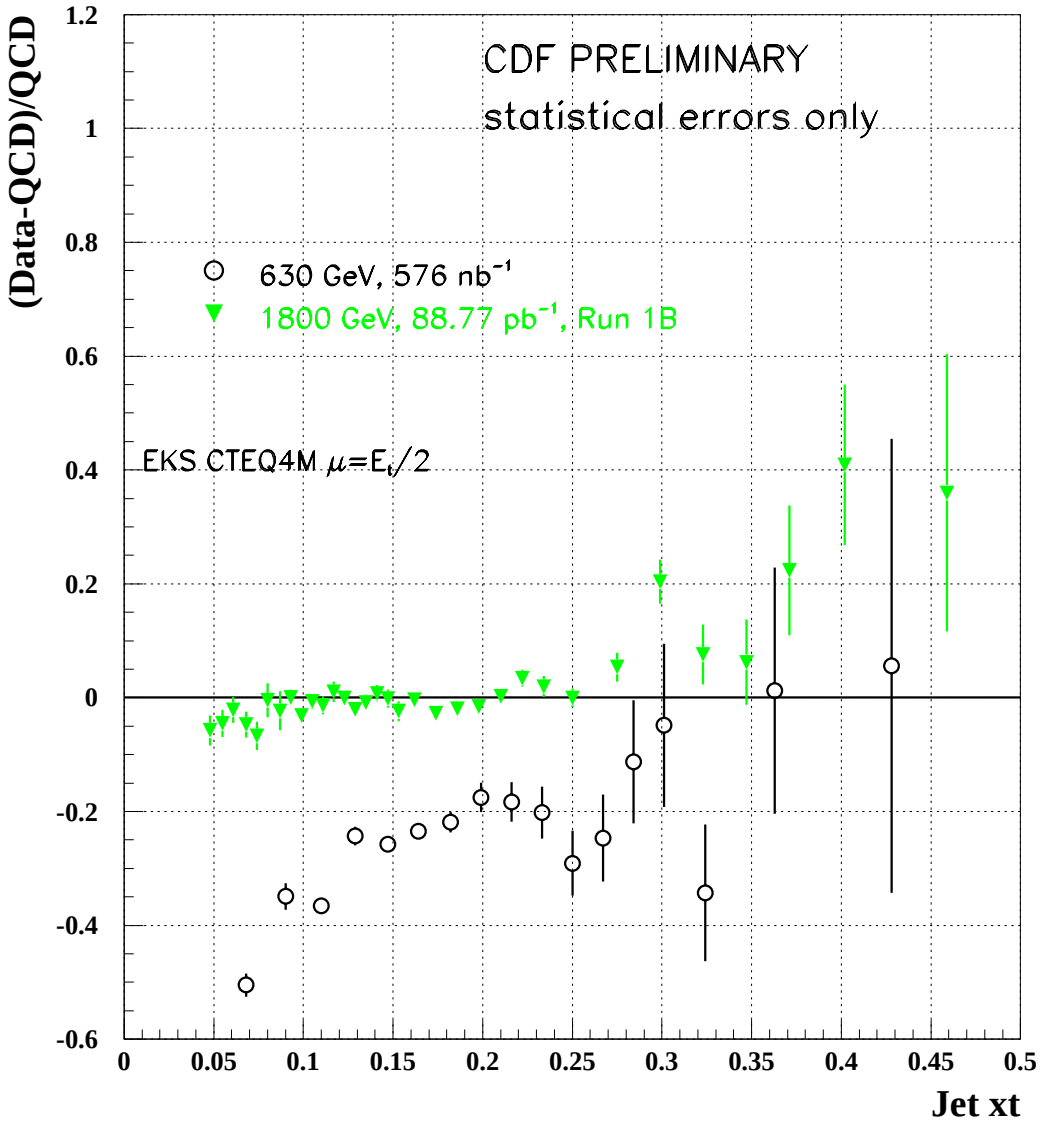

Figure 5.7: (Data-Theory)/Theory comparison with NLO QCD predictions at $\sqrt{s}$=630 and 1800 GeV.

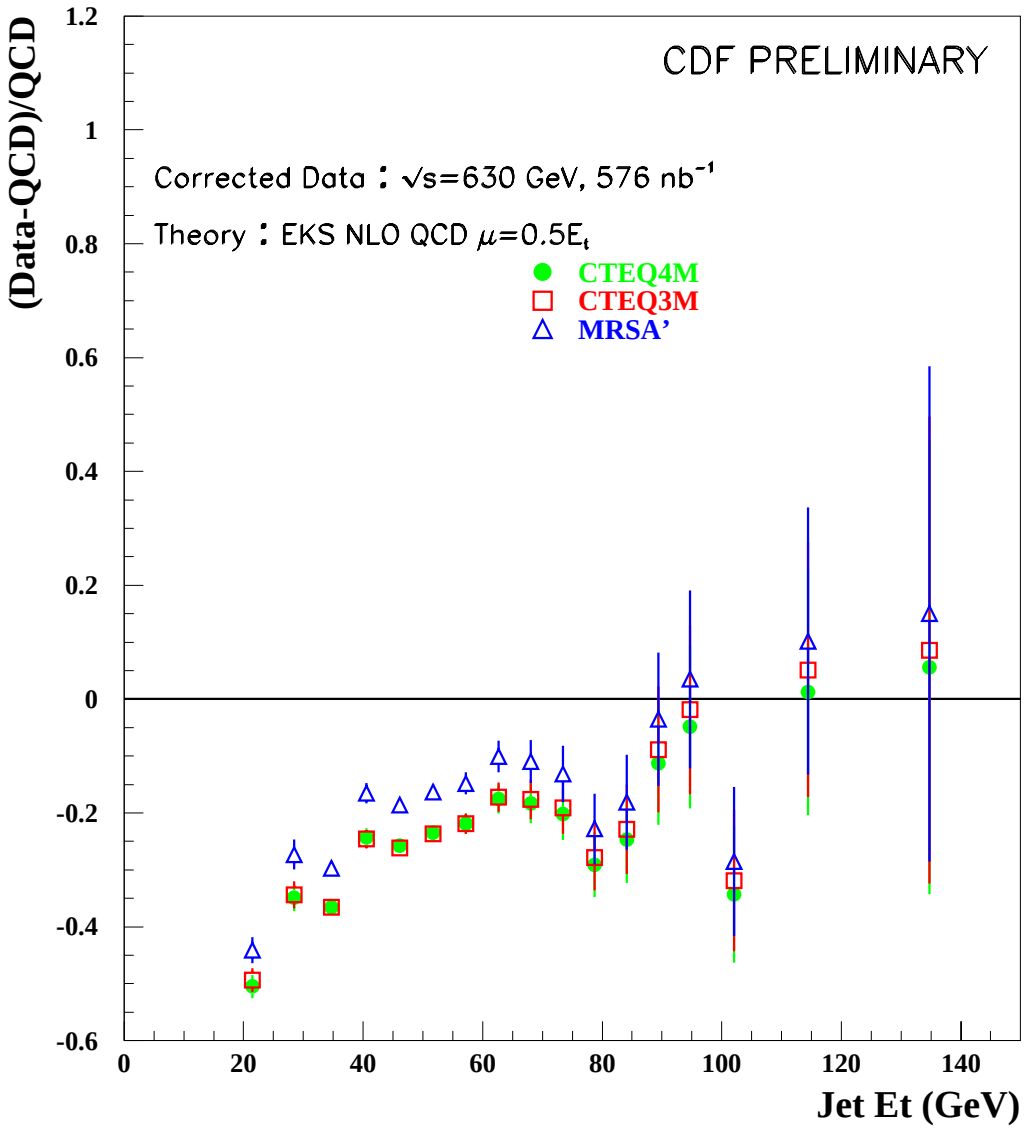

Figure 5.8: (Data-Theory)/Theory comparison with NLO QCD predictions at $\sqrt{s}$=630 GeV. Comparison for different sets of *pdf*'s is presented.

Chapter 6

Fragmentation Study. Dependence of Calorimeter Response on $\sqrt{s}$.

The results presented in Chapter 5 were obtained by unsmearing the raw inclusive jet cross section using a detector response function, $\mathcal{RF}$, which was tuned to jets produced at $\sqrt{s}$=1800 GeV. The same $\mathcal{RF}$ can be used for both data sets if the detector response to jets of same E_t^{true} but produced at different center of mass energies are the same. The detector response to a jet with the transverse energy E_t^{true} depends on the momentum spectrum and spatial distribution of the particles within the jet. The momentum spectrum of the particles is governed by the fragmentation process. The fragmentation depends on the type of parton. Contribution of gluons and quarks is different at the two $\sqrt{s}$ values and may lead to different detector responses.

This Chapter describes the study of the fragmentation process and the detector response to jets simulated using the HERWIG event generator and to jets observed with the CDF detector at $\sqrt{s}$=630 and 1800 GeV.

6.1 HERWIG

The HERWIG event generator was used for an independent test of the $\sqrt{s}$ dependence of the detector response function. The $\mathcal{RF}$ derived from HERWIG at two $\sqrt{s}$ values were compared with each other and with the standard $\mathcal{RF}$.

HERWIG predictions are based on the leading order (LO) QCD matrix element calculations. The parton-shower method is used to generate the initial and final state radiation.

The HERWIG 5.6 version implemented in the CDF Analysis Control was used in this study. Initialization parameters were set as follows:

```
PROC 1500              ( QCD 2to2 process)
BEAMS ENERGY 315.0 315.0 (momenta of colliding hadrons)
HARDS TRANSVERSE_MOMENTUM 20 315.0
HARDS RAPIDITIES -4.2  4.2  (set the rapidity range
MASSES TOP 174.0 (set the mass of the top quark)
STRUCTURE_FUNCTION MOPDF 430     (select CTEQ3M as pdf)
```

6.2 $\mathcal{RF}$ derived from HERWIG

A list of hadrons resulted from $p\bar{p}$ interaction was created as an output of every HERWIG generated event. The particles from the HERWIG output were clustered in jets by the LUCELL clustering algorithm, which provided the true jets generated by HERWIG. The LUCELL clustering is very similar to CDF clustering algorithm. In order to obtain the HERWIG "measured" jets, the particles from HERWIG output were passed through the QFL package which simulated the detector response to the particles and stored the events in the same format as the real

measured data. This enabled the further analysis of HERWIG events with the same code which was used for the CDF data.

For a fixed value of true jet E_t^{true}, the measured jet E_t^{meas} distribution was histogrammed. A set of such histograms corresponding to various values of true jet E_t^{true} provided the HERWIG response function.

6.3 HERWIG $\mathcal{RF}$ at different $\sqrt{s}$

For every value of true jet E_t the mean value of the measured E_t distribution is calculated. This is done for HERWIG $\mathcal{RF}$'s obtained at both values of center of mass energy. The ratio of the mean E_t^{meas} ($< E_t^{meas} >_{630}$ / $< E_t^{meas} >_{1800}$) is presented in Figure 6.1. This plot shows that the average response to a jet is the same for jets produced at both center of mass energies. For true jets with E_t below 15 GeV, at $\sqrt{s}$=630 GeV the mean measured jet E_t is lower than at $\sqrt{s}$=1800 GeV. This may yield an additional uncertainty on the value of corrected jet E_t (for low E_t jets) at $\sqrt{s}$=630 GeV. However, this uncertainty does not explain the observed discrepancy between the measured cross section and NLO QCD predictions at $\sqrt{s}$=630 GeV. Comparison of the "shapes" of $\mathcal{RF}$'s corresponding to the same values of E_t^{true} at different center of mass energies is given in Figure 6.3. The study of fragmentation in HERWIG shows no significant dependence on center of mass energy.

6.4 Comparison of HERWIG $\mathcal{RF}$ with SETPRT

The response function obtained from HERWIG at $\sqrt{s}$=1800 GeV was compared with the standard SETPRT $\mathcal{RF}$. Figure 6.2 presents the ratio of the mean E_t^{meas} (HERWIG $\mathcal{RF}$ at $\sqrt{s}$=1800 GeV over standard $\mathcal{RF}$) as a function of E_t^{true}.

The difference in response functions obtained from HERWIG and SETPRT at the same center of mass energy indicates a difference in fragmentation models. This difference can be caused by different charge multiplicity in the P_t spectrum in HERWIG and in data (the fragmentation parameters in SETPRT were tuned to reproduce the momentum spectra of the charged component of the jets measured at $\sqrt{s}$=1800 GeV). Studies of fragmentation in HERWIG showed that there is no dependence of the detector response on center of mass energy; however, a difference between response functions obtained from HERWIG and from SETPRT was observed. The next section describes the study of the calorimeter response to jets experimentally observed at different $\sqrt{s}$. It is shown that the detector response is the same at both values of $\sqrt{s}$; therefore the same $\mathcal{RF}$ should be used for the unsmearing of $\sqrt{s}$=630 GeV data as for $\sqrt{s}$=1800 GeV.

6.5 Fragmentation Study in Data

As was mentioned in the previous sections, the difference in momentum spectra of particles within jets (caused by possible dependence of fragmentation on $\sqrt{s}$) may result in different detector responses to $\sqrt{s}$=630 and 1800 GeV jets. A comparison of the energy lost by a jet in the detector at two center of mass energies would exhibit a difference in detector response.

A study of the fragmentation dependence on $\sqrt{s}$ in two data sets (at $\sqrt{s}$=546 and 1800 GeV) is presented in Figure 6.4. The energy loss[38] is defined as:

$$Loss(E_t^{jet}) = \sum_i \left(P_i - CAL(P_i)\right),$$

where P_i is the momentum of the i^{th} charged particle within the jet cone, $CAL(P_i)$ is the calorimeter response to a particle with momentum P_i obtained from the test

beam measurements. The value of $Loss/E_t^{jet}$ for two data sets is plotted versus jet E_t. The losses at two $\sqrt{s}$ values are close to each other, a small difference at low E_t can be accommodated by subtracting the Underlying Event E_t, corresponding to each center of mass energy.

Based on these studies we conclude that same $\mathcal{RF}$ should be used to correct both $\sqrt{s}$=630 and 1800 GeV data. We use SETPRT $\mathcal{RF}$ as it is tuned to CDF data.

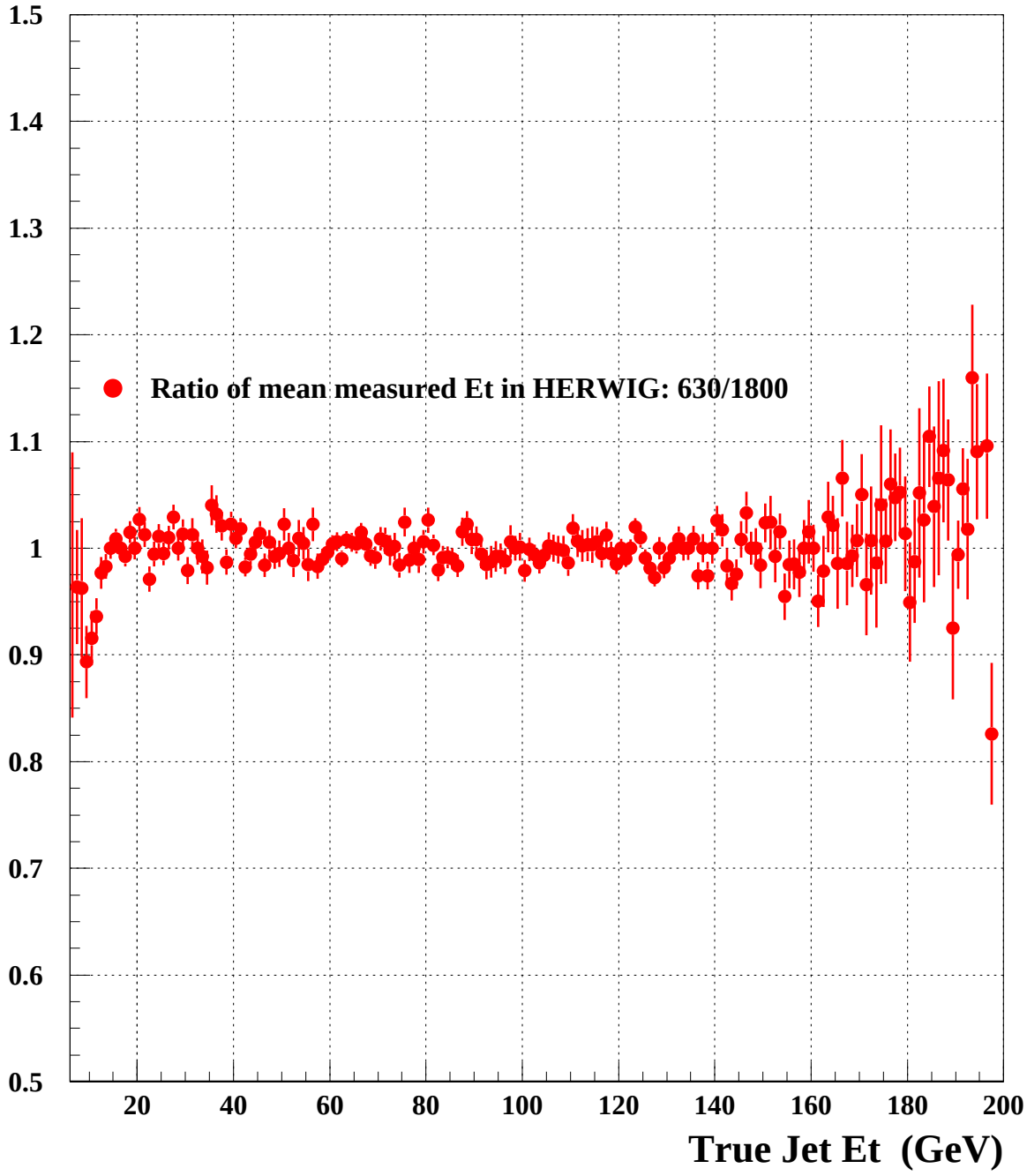

Figure 6.1: Ratio of average measured jet E_t's, $< E_t^{meas} >_{630}$ / $< E_t^{meas} >_{1800}$, obtained from HERWIG for $\sqrt{s}$= 630 and 1800 GeV, versus true jet E_t.

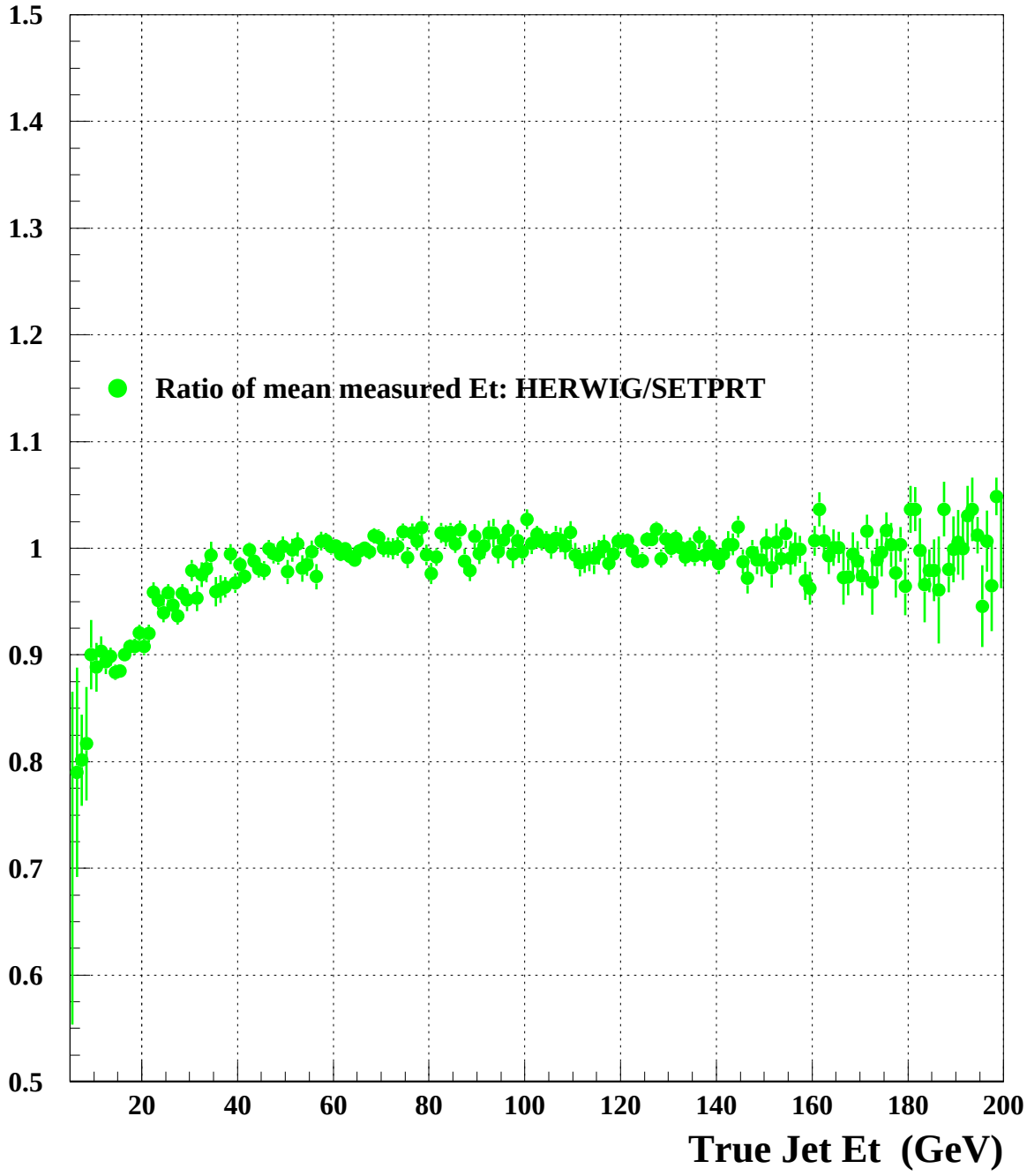

Figure 6.2: Ratio of average measured jet E_t's, $< E_t^{HERWIG} > / < E_t^{SETPRT} >$, obtained from HERWIG and SETPRT $\mathcal{RF}$, versus true jet E_t. The HERWIG $\mathcal{RF}$ is for $\sqrt{s}$=1800 GeV.

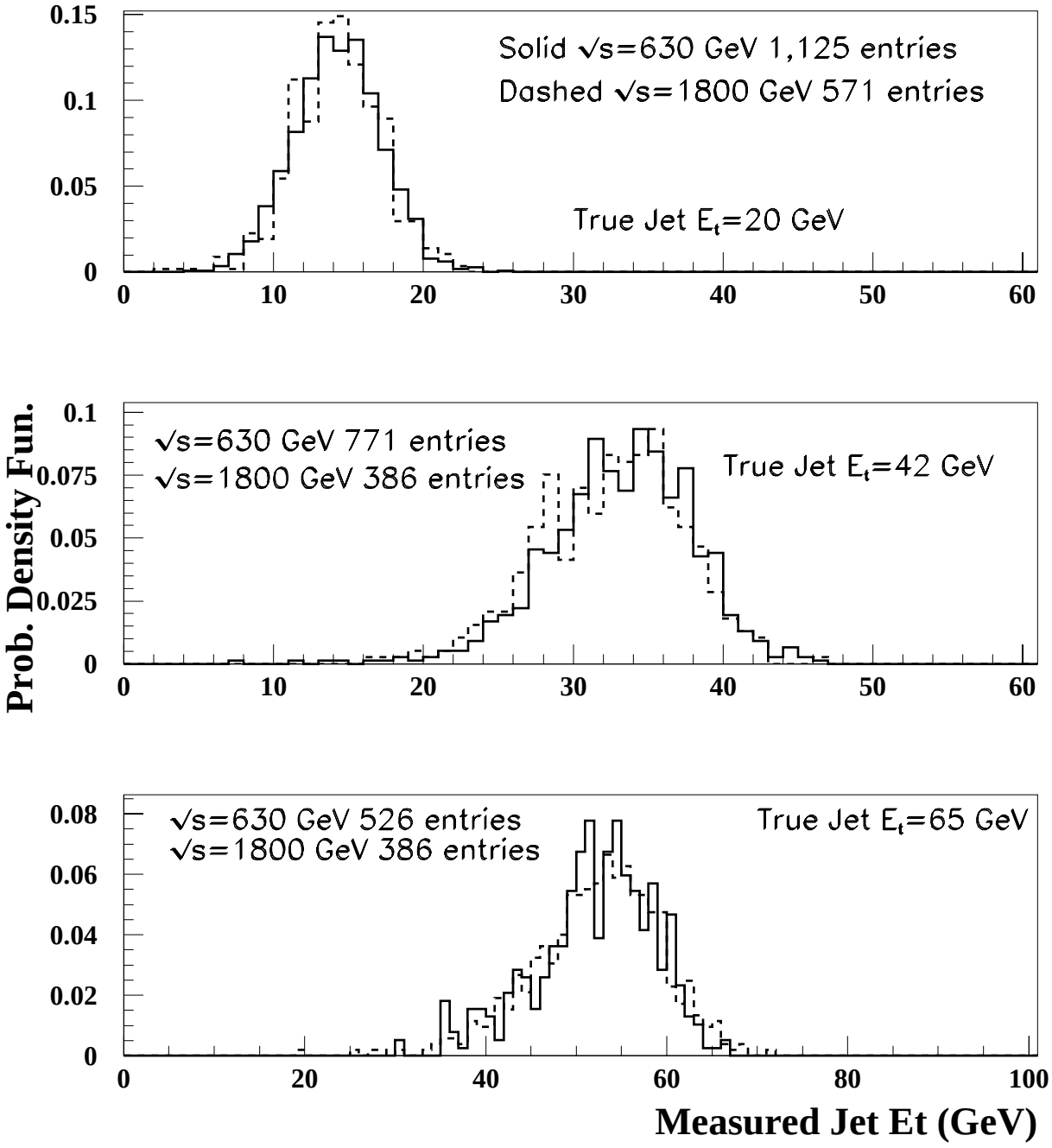

Figure 6.3: Comparison of HERWIG $\mathcal{RF}$ at $\sqrt{s}$=630 and 1800 GeV for three values of true jet E_t.

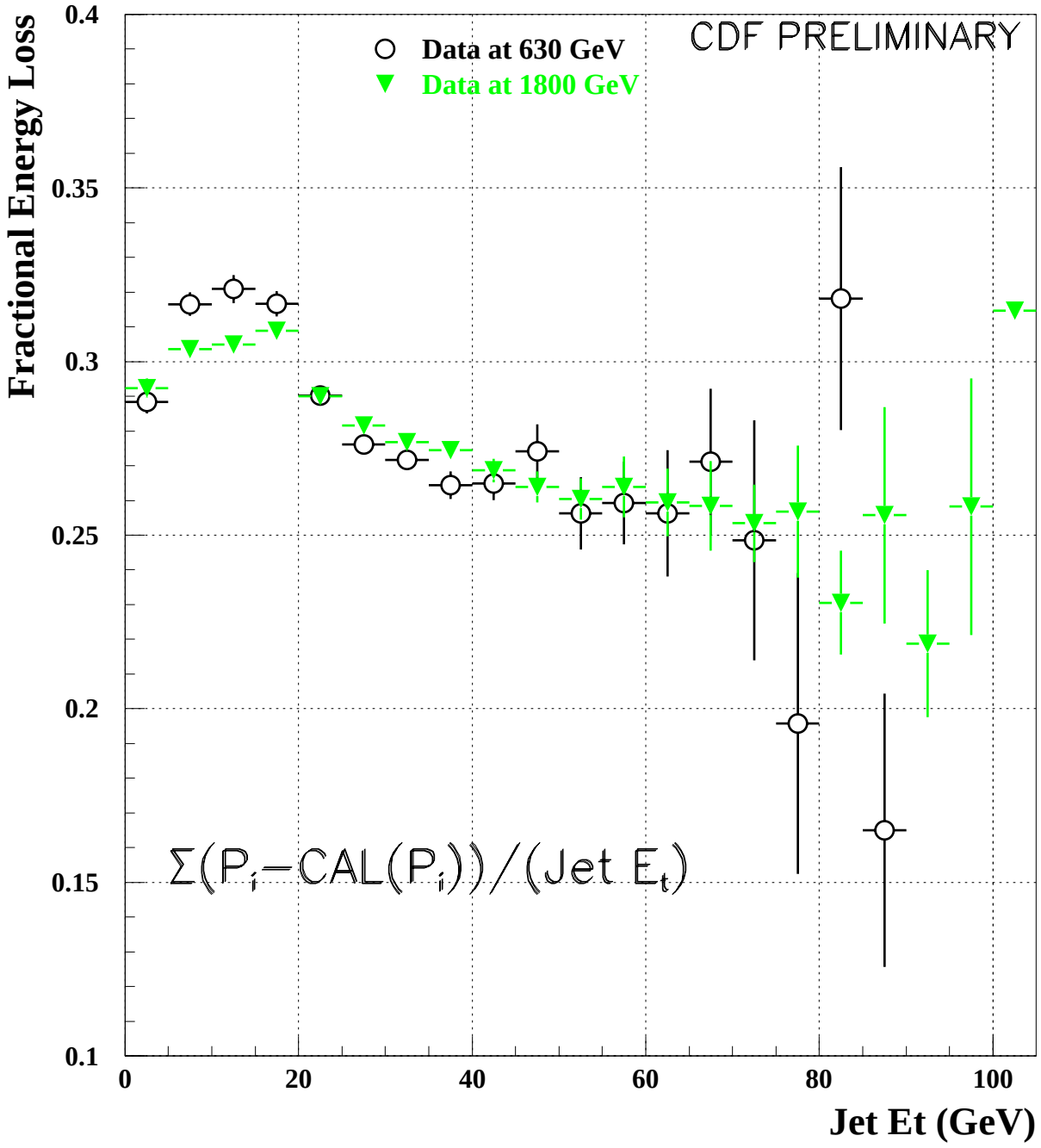

Figure 6.4: Jet Energy Loss in the calorimetry as a function of jet E_t for data measured at $\sqrt{s}$=630 and 1800 GeV.

Chapter 7

Systematic Uncertainties

The Response Function ($\mathcal{RF}$) used in the unsmearing procedure accounts for the distortions of the true spectrum by the detector due to energy degradation, finite resolution and Underlying Event (UE) E_t.

Uncertainties or possible changes in the values of the detector effects, the Underlying Event (UE) E_t and the uncertainty on the fragmentation parameters in SETPRT propagate to the uncertainty on the corrected cross section.

The following sources of the systematic uncertainties were considered:

- Calorimeter response to single e^-/γ
- Calorimeter response to high P_t pions
- Calorimeter response to low P_t pions
- Energy resolution of the calorimeter
- E_t scale of the calorimeter
- Fragmentation properties

- Underlying Event E_t

A set of additional $\mathcal{RF}$'s was developed for each of these parameters. A pair of $\mathcal{RF}$ corresponded to a change in one parameter upward and downward.

The raw cross section was unsmeared with each of these $\mathcal{RF}$. The resulting corrected cross section (and the Physics Curve) represented the change in cross section due to a change in only one parameter.

The $\mathcal{RF}$ corresponding to the nominal values of the parameters are referred to as *nominal* $\mathcal{RF}$. Correspondingly, the corrected cross section and the Physics Curve ($\mathcal{F}$) obtained with the nominal $\mathcal{RF}$ is referred to as the nominal cross section and nominal physics curve $\mathcal{F}_o$.

The systematic uncertainty on the cross section due to the uncertainty on the underlying parameter was calculated as follows:

$$\delta_\alpha(E_t) = \frac{(\mathcal{F}_\alpha(E_t) - \mathcal{F}_o(E_t))}{\mathcal{F}_o(E_t)} \cdot \frac{d^2\sigma}{dE_t d\eta},$$

where α is the index of the source of uncertainty, $d^2\sigma/dE_t d\eta$ is the nominal cross section, $\mathcal{F}(E_t)$ is the nominal Physics Curve and $\mathcal{F}_\alpha(E_t)$ is the Physics Curve corresponding to the source of uncertainty α. The positive and negative uncertainties were grouped separately. The total systematic uncertainty on the cross section was calculated as:

$$\delta^\pm(E_t) = \sqrt{\sum_\alpha \left(\delta^\pm_\alpha(E_t)\right)^2},$$

where "+" and "-" indicate the sign of the uncertainty.

The following sections describe the sources of the uncertainties and the evaluation of the uncertainty on the ratio of the scaled cross sections at two center of mass energies.

The systematic uncertainties on the cross section at $\sqrt{s}$= 630 GeV are listed in Tables 7.1 and 7.2, and plotted in Figures 7.1 and 7.2.

7.1 Detector Response to e^-/γ

Neutral pions decay into pairs of photons, which generate electromagnetic showers in the Electromagnetic calorimeter. The response of the calorimeter to electrons or photons was used as an estimate of the energy deposited by the neutral pions in the jets.

7.2 Detector response to pions

The detector response to high p_t single pions (>15 GeV) was measured in test beams. The response for low p_t single pions was obtained from minimum bias data. The uncertainties on the cross section were estimated separately for low and high p_t pions.

7.3 Energy resolution of the detector

The energy resolution of the detector was responsible for the smearing of the jet spectrum. The $\mathcal{RF}$ with modified energy resolution ($\pm$10% change of the width of the $\mathcal{RF}$) was used in the unsmearing procedure.

7.4 Energy scale stability of the detector

The energy scale of the detector might change with time. The uncertainty caused by this source was measured by scaling the jet E_t in the raw data by 1% up and down. The value of 1% was chosen since it reflected the change (with respect to 1989 CDF Data) in the energy scale of Central EM calorimeter due to aging of the scintillators.

7.5 Fragmentation Properties

The fragmentation tuning was performed by adjustment of the parameters of SETPRT so that the spectra of charged particles in the simulated jets reproduced the spectra in the measured jets. The efficiency of finding tracks associated with the jets affected the quality of the fragmentation parameters. The resulting uncertainty on fragmentation parameters was a source of the uncertainty on the corrected cross section. The $\mathcal{RF}$ was evaluated for modified values of the fragmentation parameters. The cross section unsmeared with this $\mathcal{RF}$ and the corresponding $\mathcal{F}$ were used for the evaluation of the systematic uncertainty on the cross section and the ratio of corrected cross sections due to the uncertainty on fragmentation tuning.

7.6 Underlying Event (UE)

The UE E_t in jet production processes was estimated from a Minimum Bias Sample, as the average E_t measured in cones with (η, ϕ) radius of 0.7 randomly drawn in the Central Calorimeter ($0.1 < |\eta| < 0.7$).

An UE E_t change of 30% was incorporated into the $\mathcal{RF}$. The uncertainty of 30%

covers the difference in UE E_t measured in Minimum Bias sample and in dijet events (measured in directions perpendicular to the jet axes). The section corrected with this modified $\mathcal{RF}$ provided the systematic uncertainty due to the uncertainty on UE E_t.

7.7 Integrated Luminosity

The integrated luminosity ($\mathcal{L}$) enters the expression for the cross section as a normalization factor. The uncertainty on the value of integrated luminosity $\delta(\mathcal{L})$ contributes to the systematic uncertainty on the cross section as follows:

$$\delta\sigma = \frac{d\sigma}{d\mathcal{L}}\delta\mathcal{L} = \sigma \cdot \frac{\delta\mathcal{L}}{\mathcal{L}}.$$

The uncertainties on the luminosity ($\delta\mathcal{L}/\mathcal{L}$) at both center of mass energies were 4.4% for $\sqrt{s}$=630 GeV and 4.1% for $\sqrt{s}$=1800 GeV.

xt^{jet}	e^-/γ. Resp.	Energy Resol.	π Resp. low p_t	π Resp. high p_t	Total [nb/GeV]
0.068	+0.464E+01	+0.223E+02	+0.168E+02	+0.465E+01	+0.436E+02
	−0.569E+01	−0.198E+02	−0.168E+02	−0.252E+01	−0.395E+02
0.090	+0.114E+01	+0.327E+01	+0.400E+01	+0.122E+01	+0.837E+01
	−0.140E+01	−0.321E+01	−0.401E+01	−0.825E+00	−0.791E+01
0.110	+0.421E+00	+0.886E+00	+0.143E+01	+0.482E+00	+0.278E+01
	−0.514E+00	−0.907E+00	−0.143E+01	−0.381E+00	−0.266E+01
0.129	+0.186E+00	+0.326E+00	+0.607E+00	+0.227E+00	+0.116E+01
	−0.227E+00	−0.338E+00	−0.612E+00	−0.203E+00	−0.112E+01
0.147	+0.907E-01	+0.142E+00	+0.284E+00	+0.117E+00	+0.546E+00
	−0.110E+00	−0.148E+00	−0.288E+00	−0.115E+00	−0.528E+00
0.164	+0.470E-01	+0.692E-01	+0.142E+00	+0.642E-01	+0.275E+00
	−0.571E-01	−0.719E-01	−0.144E+00	−0.678E-01	−0.268E+00
0.182	+0.254E-01	+0.360E-01	+0.737E-01	+0.366E-01	+0.146E+00
	−0.309E-01	−0.373E-01	−0.752E-01	−0.409E-01	−0.143E+00
0.199	+0.142E-01	+0.196E-01	+0.397E-01	+0.215E-01	+0.801E-01
	−0.173E-01	−0.203E-01	−0.406E-01	−0.251E-01	−0.792E-01
0.216	+0.819E-02	+0.110E-01	+0.219E-01	+0.129E-01	+0.453E-01
	−0.990E-02	−0.114E-01	−0.226E-01	−0.156E-01	−0.450E-01
0.233	+0.481E-02	+0.632E-02	+0.124E-01	+0.786E-02	+0.262E-01
	−0.581E-02	−0.661E-02	−0.128E-01	−0.984E-02	−0.261E-01
0.250	+0.288E-02	+0.370E-02	+0.714E-02	+0.487E-02	+0.154E-01
	−0.347E-02	−0.389E-02	−0.741E-02	−0.626E-02	−0.155E-01
0.267	+0.175E-02	+0.220E-02	+0.417E-02	+0.306E-02	+0.926E-02
	−0.210E-02	−0.233E-02	−0.435E-02	−0.401E-02	−0.928E-02
0.284	+0.108E-02	+0.133E-02	+0.247E-02	+0.195E-02	+0.564E-02
	−0.129E-02	−0.141E-02	−0.260E-02	−0.260E-02	−0.565E-02
0.301	+0.672E-03	+0.813E-03	+0.149E-02	+0.125E-02	+0.349E-02
	−0.806E-03	−0.866E-03	−0.157E-02	−0.169E-02	−0.348E-02
0.324	+0.357E-03	+0.421E-03	+0.747E-03	+0.690E-03	+0.183E-02
	−0.427E-03	−0.447E-03	−0.795E-03	−0.951E-03	−0.182E-02
0.363	+0.128E-03	+0.147E-03	+0.244E-03	+0.263E-03	+0.647E-03
	−0.153E-03	−0.153E-03	−0.264E-03	−0.372E-03	−0.634E-03
0.428	+0.274E-04	+0.316E-04	+0.431E-04	+0.613E-04	+0.136E-03
	−0.323E-04	−0.292E-04	−0.484E-04	−0.894E-04	−0.132E-03

Table 7.1: Systematic uncertainties on the corrected inclusive jet cross section measured at $\sqrt{s}$=630 GeV. The uncertainty due to the integrated luminosity (4.4% independent of x_t) is added in quadrature to the total uncertainty.

x_t^{jet}	E_t scale	Fragm.	UE E_t	Total [nb/GeV]
0.068	+0.884E+01	+0.180E+02	+0.244E+02	+0.436E+02
	−0.572E+01	−0.163E+02	−0.216E+02	−0.395E+02
0.090	+0.211E+01	+0.438E+01	+0.354E+01	+0.837E+01
	−0.146E+01	−0.396E+01	−0.340E+01	−0.791E+01
0.110	+0.768E+00	+0.160E+01	+0.928E+00	+0.278E+01
	−0.600E+00	−0.144E+01	−0.915E+00	−0.266E+01
0.129	+0.337E+00	+0.696E+00	+0.324E+00	+0.116E+01
	−0.292E+00	−0.625E+00	−0.320E+00	−0.112E+01
0.147	+0.164E+00	+0.334E+00	+0.133E+00	+0.546E+00
	−0.154E+00	−0.299E+00	−0.131E+00	−0.528E+00
0.164	+0.854E-01	+0.171E+00	+0.606E-01	+0.275E+00
	−0.845E-01	−0.152E+00	−0.590E-01	−0.268E+00
0.182	+0.466E-01	+0.912E-01	+0.295E-01	+0.146E+00
	−0.475E-01	−0.811E-01	−0.286E-01	−0.143E+00
0.199	+0.264E-01	+0.503E-01	+0.150E-01	+0.801E-01
	−0.271E-01	−0.446E-01	−0.146E-01	−0.792E-01
0.216	+0.153E-01	+0.285E-01	+0.792E-02	+0.453E-01
	−0.157E-01	−0.252E-01	−0.775E-02	−0.450E-01
0.233	+0.914E-02	+0.165E-01	+0.427E-02	+0.262E-01
	−0.912E-02	−0.145E-01	−0.423E-02	−0.261E-01
0.250	+0.555E-02	+0.974E-02	+0.234E-02	+0.154E-01
	−0.533E-02	−0.855E-02	−0.236E-02	−0.155E-01
0.267	+0.343E-02	+0.583E-02	+0.131E-02	+0.926E-02
	−0.312E-02	−0.510E-02	−0.134E-02	−0.928E-02
0.284	+0.215E-02	+0.354E-02	+0.740E-03	+0.564E-02
	−0.182E-02	−0.309E-02	−0.768E-03	−0.565E-02
0.301	+0.137E-02	+0.218E-02	+0.425E-03	+0.349E-02
	−0.106E-02	−0.190E-02	−0.447E-03	−0.348E-02
0.324	+0.749E-03	+0.113E-02	+0.202E-03	+0.183E-02
	−0.491E-03	−0.982E-03	−0.214E-03	−0.182E-02
0.363	+0.284E-03	+0.390E-03	+0.621E-04	+0.647E-03
	−0.118E-03	−0.338E-03	−0.636E-04	−0.634E-03
0.428	+0.674E-04	+0.763E-04	+0.129E-04	+0.136E-03
	−0.708E-05	−0.663E-04	−0.930E-05	−0.132E-03

Table 7.2: Systematic uncertainties on the corrected inclusive jet cross section measured at $\sqrt{s}$=630 GeV. The uncertainty due to the integrated luminosity (4.4% independent of x_t) is added in quadrature to the total uncertainty.

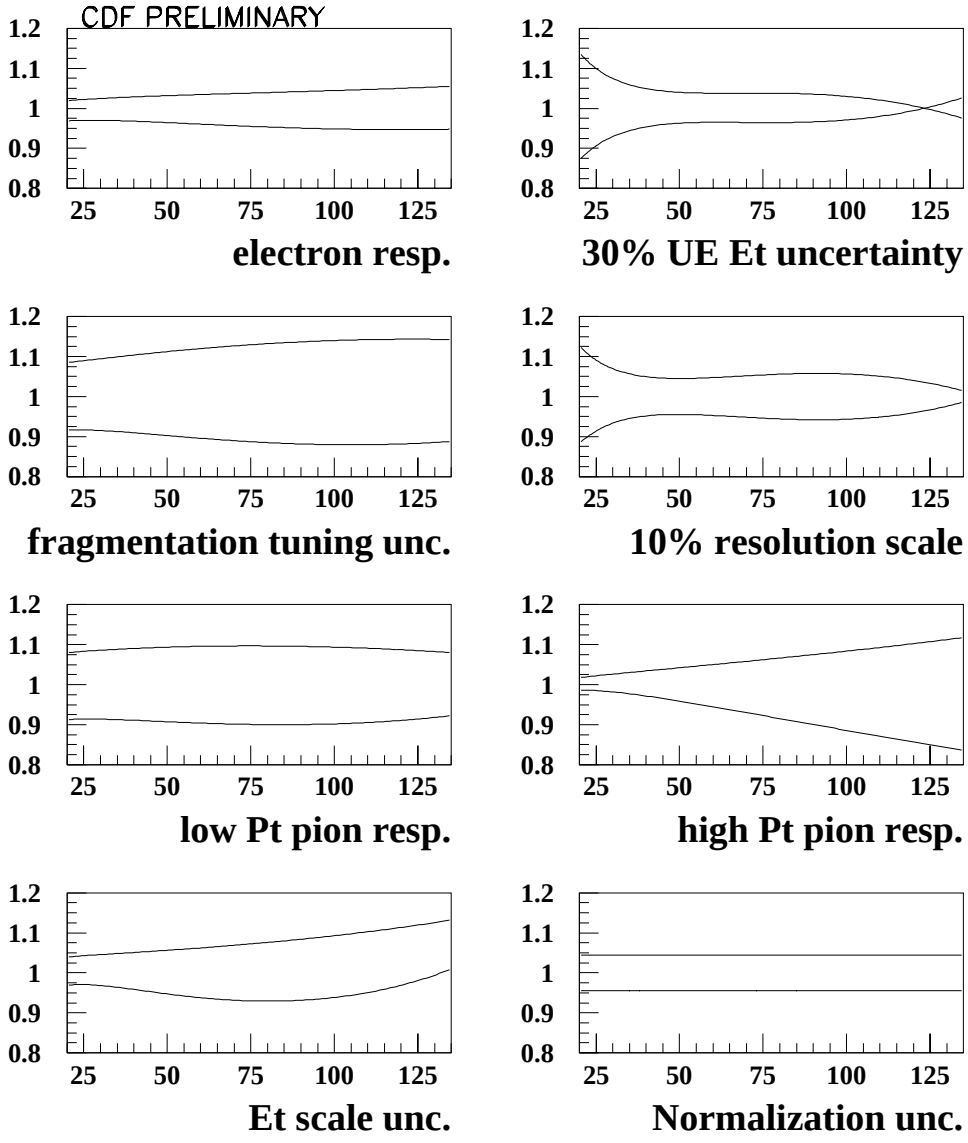

Figure 7.1: The systematic uncertainties for the $\sqrt{s}$=630 GeV Data Set.

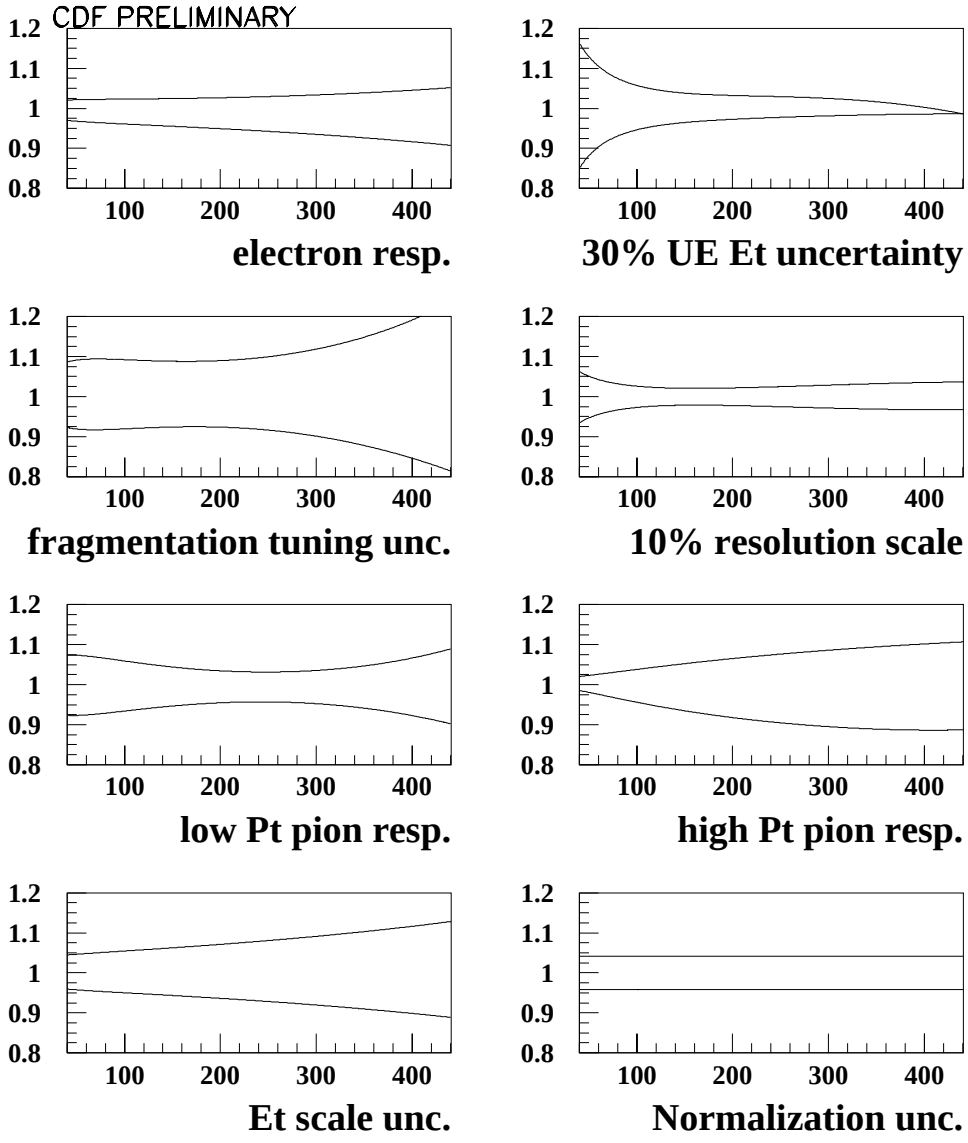

Figure 7.2: The systematic uncertainties for the $\sqrt{s}$=1800 GeV Data Set.

Chapter 8

The Ratio of Scaled Cross Sections.

The scaled cross section as a function of x_t has the following form:

$$E_t^3 \cdot \left(d^2\sigma(x_t)/dE_t d\eta\right) =$$

$$\left(0.5x_t \cdot \sqrt{s}\right)^3 \cdot \left(d^2\sigma(x_t)/dE_t d\eta\right)$$

The ratio of the scaled cross sections was calculated as:

$$R(x_t) = \left(\frac{630}{1800}\right)^3 \cdot \frac{d^2\sigma^{630}(x_t)/dE_t d\eta}{d^2\sigma^{1800}(x_t)/dE_t d\eta}$$

$$= 0.0429 \cdot \frac{d^2\sigma^{630}(x_t)/dE_t d\eta}{d^2\sigma^{1800}(x_t)/dE_t d\eta},$$

where 0.0429 is the scaling factor, x_t are the $\sqrt{s}$=630 GeV data points, $d^2\sigma^{630}(x_t)/dE_t d\eta$ is the corrected cross section at $\sqrt{s}$=630 GeV, $d^2\sigma^{1800}(x_t)/dE_t d\eta$ is the corrected cross section at $\sqrt{s}$=1800 GeV.

Data at both center of mass energies were binned in E_t so the x_t values of the data points at $\sqrt{s}$=1800 GeV do not match the data points at $\sqrt{s}$=630 GeV. The following procedure was used to evaluate the $\sqrt{s}$=1800 GeV cross section at the x_t values of the $\sqrt{s}$=630 GeV data:

$$\frac{d^2\sigma^{1800}(x_t^{630})}{dE_t d\eta} = \mathcal{F}^{1800}(x_t^{630}) \cdot \frac{d^2\sigma^{1800}(x_t^{1800})/dE_t d\eta}{\mathcal{F}^{1800}(x_t^{1800})},$$

where x_t^{630} is the x_t of a given $\sqrt{s}$=630 GeV data point; x_t^{1800} is the closest x_t point of the $\sqrt{s}$=1800 GeV data (typically within 3% of x_t^{630}). $\mathcal{F}^{1800}$ was evaluated at x_t^{630}; the ratio of the corrected cross section at $\sqrt{s}$=1800 GeV in the nearest x_t point to the value of $\mathcal{F}$ at that point was used as a normalization factor to correct for the difference between the $\mathcal{F}$ and the corrected cross section. The resulting value of $\frac{d^2\sigma^{1800}(x_t^{630})}{dE_t d\eta}$ was taken as the corrected cross section at $\sqrt{s}$=1800 GeV evaluated for x_t value of x_t^{630}. The statistical error on $\sqrt{s}$=1800 GeV cross section corresponding to x_t^{1800} point was assigned to the evaluated cross section for $x_t = x_t^{630}$.

The statistical errors on the ratio were calculated by error propagation on a ratio of uncorrelated parameters:

$$\delta\left(R(x_t)\right) = R(x_t) \cdot \sqrt{\left(\delta\sigma^{630}/\sigma^{630}\right)^2 + \left(\delta\sigma^{1800}/\sigma^{1800}\right)^2},$$

where $\sigma^{\sqrt{s}} \equiv d^2\sigma^{\sqrt{s}}(x_t)/dE_t d\eta$.

The ratio of the cross sections is provided in Table 8.1 and plotted in Figure 8.1.

8.1 Uncertainty on The Ratio of Corrected Cross Sections

The systematic uncertainties on the ratio of the scaled inclusive jet cross sections were evaluated assuming that

- the different sources of the uncertainties are not correlated,
- there is 100% bin-to-bin correlation for each source of the uncertainty,
- for the same source, the uncertainties on the cross sections measured at different center of mass energies are 100% correlated.

For each source of systematic uncertainty, the corresponding $\mathcal{F}_\alpha$'s at both center of mass energies were evaluated as functions of jet x_t:

$$x_t = 2E_t^{corrected}/\sqrt{s},$$

where $E_t^{corrected}$ are the corrected values of jet transverse energy taken from the $\sqrt{s}$= 630 GeV data set.

The ratio of the scaled $\mathcal{F}_\alpha$'s for each source ($R_{p,\alpha}$) was calculated as:

$$R_{p,\alpha} = \frac{(E_t^{630})^3 \cdot \mathcal{F}_\alpha^{630}(x_t)}{(E_t^{1800})^3 \cdot \mathcal{F}_\alpha^{1800}(x_t)} = 0.0429 \cdot \frac{\mathcal{F}_\alpha^{630}(x_t)}{\mathcal{F}_\alpha^{1800}(x_t)}.$$

These ratios were evaluated for $\mathcal{F}_\alpha$'s corresponding to the "positive" and "negative" systematic uncertainties and for the nominal $\mathcal{F}$'s at both center of mass energies.

The ratio of the scaled cross sections corresponding to the systematic uncertainty α was estimated as:

$$R_{\sigma,\alpha}(x_t) = R_{p,\alpha}(x_t) \cdot \frac{R_\sigma(x_t)}{R_p(x_t)},$$

where $R_{\sigma,\alpha}(x_t)$ is the ratio of the cross sections with $\mathcal{RF}$, corresponding to a change in parameter α, $R_p(x_t)$ is the ratio of the nominal $\mathcal{F}$'s, $R_{p,\alpha}(x_t)$ is the ratio of the $\mathcal{F}_\alpha$'s corresponding to the source of systematic uncertainty α.

The difference between $R_\sigma(x_t)$, the ratio of nominal corrected cross sections and $R_{\sigma,\alpha}$, the ratio of cross sections corresponding to a change in parameter α, is defined as the systematic uncertainty on the ratio of the cross sections due to the uncertainty on parameter α:

$$\delta\left(R_\alpha\right) = R_{\sigma,\alpha} - R_\sigma = R_\sigma \cdot \left(R_{p,\alpha}/R_p - 1\right).$$

This definition automatically accounts for the correlations of systematic uncertainties in the measurements of the inclusive jet cross sections at different center of mass energies.

The uncertainty on the cross section due to the uncertainty on the integrated luminosity was treated as uncorrelated in the measurements at two values of $\sqrt{s}$; error propagation for uncorrelated uncertainties was used to evaluate the uncertainty on the ratio:

$$\delta\left(\frac{\sigma^{630}}{\sigma^{1800}}\right) = \frac{\sigma^{630}}{\sigma^{1800}} \cdot \sqrt{\left(\frac{\delta(\mathcal{L}^{630})}{\mathcal{L}^{630}}\right)^2 + \left(\frac{\delta(\mathcal{L}^{1800})}{\mathcal{L}^{1800}}\right)^2},$$

where $\mathcal{L}^{\sqrt{s}}$ are the integrated luminosities: $\delta(\mathcal{L}^{630})/\mathcal{L}^{630} = 4.4\%$, $\delta(\mathcal{L}^{1800})/\mathcal{L}^{1800} = 4.09\%$, $\sigma^{\sqrt{s}}$ are the double differential cross sections:$d^2\sigma/dE_t d\eta$. The systematic uncertainty on the ratio due to the integrated luminosity was estimated to be

$$\delta\left(\frac{\sigma^{630}}{\sigma^{1800}}\right) = \frac{\sigma^{630}}{\sigma^{1800}} \cdot 6.01\%$$

The positive and negative systematic uncertainties on the ratio were grouped separately; the total uncertainty was calculated as the sum in quadrature of the uncertainties caused by different sources:

$$\delta R^{\pm}(x_t) = \sqrt{\sum_{\alpha} \left(\delta R^{\pm}_{\alpha}(x_t)\right)^2}$$

The values of the systematic uncertainties on the ratio due to different sources and of the resulting total systematic uncertainty are presented in Table 8.2 and in Figure 8.2.

	x_t	Ratio (stat. errors only)
1	0.068	0.971± 0.046
2	0.090	1.252± 0.047
3	0.110	1.256± 0.026
4	0.129	1.524± 0.037
5	0.147	1.474± 0.028
6	0.164	1.531± 0.028
7	0.182	1.598± 0.038
8	0.199	1.685± 0.055
9	0.216	1.639± 0.073
10	0.233	1.583± 0.095
11	0.250	1.438± 0.118
12	0.267	1.463± 0.151
13	0.284	1.695± 0.212
14	0.301	1.606± 0.248
15	0.324	1.246± 0.236
16	0.363	1.726± 0.391
17	0.428	1.442± 0.609

Table 8.1: Ratio of scaled cross sections

x_t^{jet}	e^-/γ. Resp.	Energy Resol.	π Resp. low p_t	π Resp. high p_t	E_t scale	Fragm.	UE E_t	Total
0.068	+0.001	+0.065	+0.011	+0.003	+0.004	+0.003	+0.017	+0.090
	−0.006	−0.056	−0.009	−0.012	−0.016	−0.002	−0.015	−0.085
0.090	+0.002	+0.047	+0.023	+0.008	+0.008	+0.000	+0.003	+0.092
	−0.009	−0.046	−0.020	−0.023	−0.021	−0.003	−0.006	−0.096
0.110	+0.003	+0.035	+0.033	+0.010	+0.009	+0.007	+0.001	+0.091
	−0.010	−0.036	−0.029	−0.027	−0.017	−0.010	−0.003	−0.095
0.129	+0.006	+0.037	+0.051	+0.014	+0.011	+0.017	+0.001	+0.114
	−0.012	−0.040	−0.047	−0.034	−0.014	−0.022	−0.002	−0.119
0.147	+0.007	+0.035	+0.059	+0.014	+0.010	+0.025	+0.001	+0.116
	−0.011	−0.038	−0.055	−0.033	−0.007	−0.030	−0.003	−0.120
0.164	+0.010	+0.037	+0.071	+0.014	+0.009	+0.034	+0.002	+0.128
	−0.011	−0.040	−0.066	−0.033	−0.001	−0.039	−0.005	−0.131
0.182	+0.012	+0.040	+0.082	+0.014	+0.008	+0.042	+0.003	+0.140
	−0.012	−0.043	−0.077	−0.031	−0.004	−0.048	−0.006	−0.143
0.199	+0.014	+0.043	+0.093	+0.014	+0.007	+0.051	+0.004	+0.154
	−0.012	−0.046	−0.088	−0.028	−0.008	−0.057	−0.009	−0.156
0.216	+0.015	+0.043	+0.096	+0.012	+0.005	+0.053	+0.003	+0.155
	−0.012	−0.046	−0.091	−0.022	−0.010	−0.060	−0.010	−0.157
0.233	+0.016	+0.042	+0.096	+0.010	+0.003	+0.054	+0.002	+0.153
	−0.012	−0.046	−0.091	−0.015	−0.009	−0.061	−0.011	−0.154
0.250	+0.015	+0.038	+0.089	+0.007	+0.001	+0.050	+0.001	+0.140
	−0.011	−0.042	−0.085	−0.008	−0.007	−0.056	−0.010	−0.141
0.267	+0.016	+0.038	+0.091	+0.005	+0.000	+0.050	+0.000	+0.142
	−0.012	−0.043	−0.087	−0.001	−0.003	−0.057	−0.011	−0.144
0.284	+0.019	+0.043	+0.104	+0.004	+0.002	+0.054	+0.001	+0.163
	−0.015	−0.050	−0.101	−0.006	−0.004	−0.063	−0.013	−0.165
0.301	+0.018	+0.040	+0.096	+0.002	+0.003	+0.047	+0.001	+0.151
	−0.016	−0.046	−0.093	−0.014	−0.014	−0.055	−0.012	−0.155
0.324	+0.014	+0.029	+0.070	+0.001	+0.004	+0.028	+0.001	+0.111
	−0.015	−0.035	−0.068	−0.020	−0.025	−0.035	−0.009	−0.118
0.363	+0.016	+0.037	+0.077	+0.006	+0.007	+0.010	+0.002	+0.136
	−0.027	−0.043	−0.076	−0.048	−0.082	−0.021	−0.010	−0.170
0.428	+0.006	+0.029	+0.020	+0.009	+0.006	+0.054	+0.021	+0.111
	−0.038	−0.027	−0.020	−0.068	−0.176	−0.049	−0.002	−0.219

Table 8.2: Systematic uncertainties on the ratio of the scaled inclusive jet cross sections ($\sigma(630\ GeV)/\sigma(1800\ GeV)$). The uncertainty on the ratio due to the integrated luminosity uncertainty (6.01% independent of x_t) is added in quadrature to the total uncertainty.

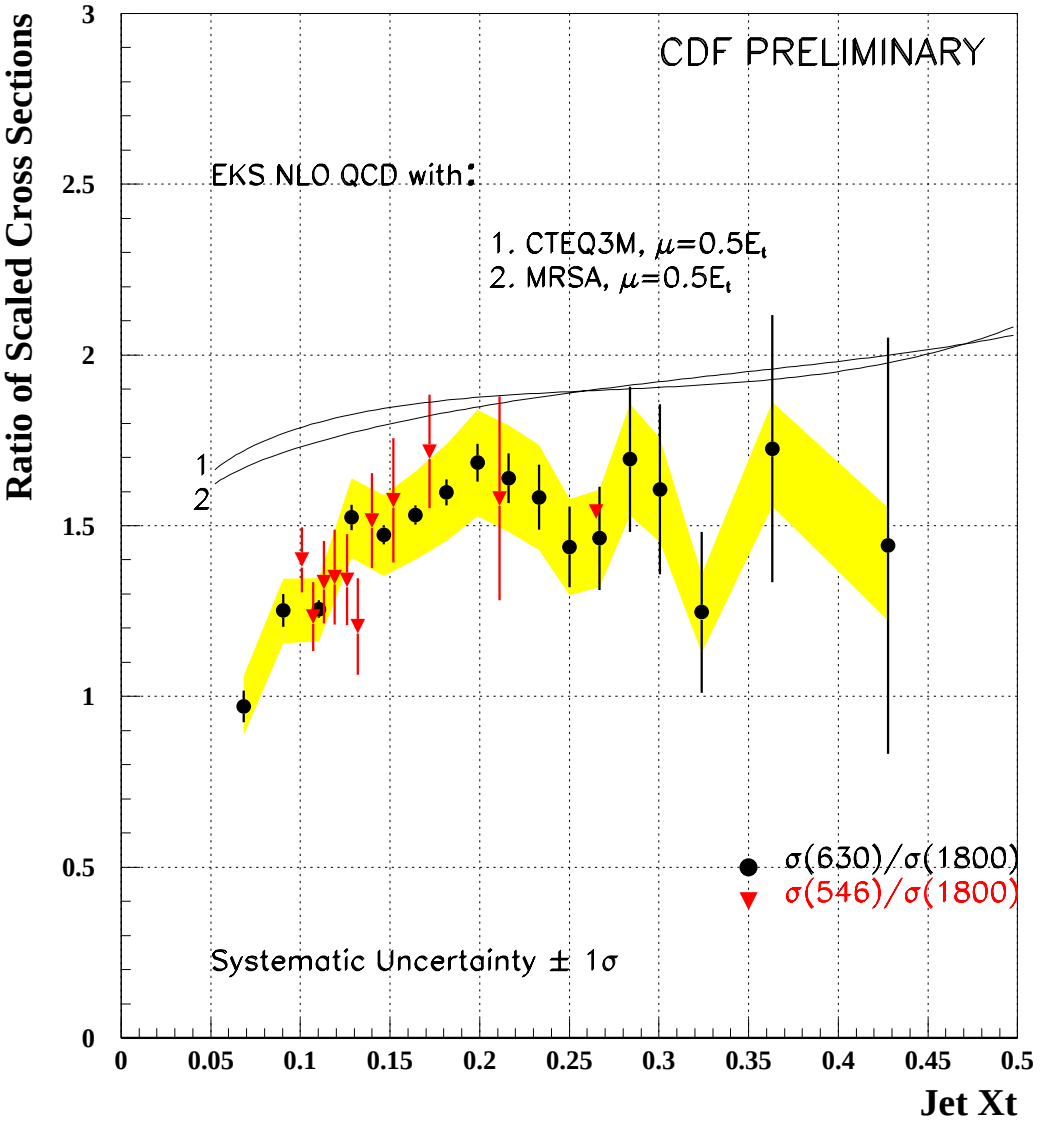

Figure 8.1: The ratio of scaled inclusive jet cross sections. Result of this analysis is compared with the ratio of cross sections measured at $\sqrt{s}$=546 and 1800 GeV.

8.2 Conclusions

The inclusive jet cross section, $\frac{d^2\sigma}{dE_t d\eta}$ is measured at center of mass energies of $\sqrt{s}$= 630 and 1800 GeV. These measurements cover the x_t range 0.07-0.43. A ratio of scaled cross sections is obtained. As expected, the systematic uncertainty on the ratio is smaller than that on the individual cross sections.

At x_t above 0.1, the measured ratio is significantly higher than the scaling prediction of 1.0.

Comparison of the measured ratio with NLO QCD showed that data are lower than QCD predictions. The difference is only in normalization for x_t above 0.2; but there is a difference in shape at the low x_t end.

A study of individual cross sections, showed that the discrepancy is due to the $\sqrt{s}$=630 GeV data. The discrepancy is present for different choices of pdf and renormalization/factorization scale used in NLO QCD calculations. This result is consistent with previous measurement by CDF of the ratio of inclusive jet cross sections at center of mass energies of 546 and 1800 GeV.

Figure 8.3 present the comparison of the ratio measured by CDF to that of DØ[39]. Two results are consistent for values of x_t above 0.12; however at low x_t end, there is a discrepancy of the order of 2σ. Since this is a data to data comparison, the explanation for the discrepancy should be sought in the details of the analysis. The two collaborations use different methods of energy calibration. A possible reason is that the Underlying Event is handled differently in the two experiments. This can affect the low x_t part of the data, while the high x_t should remain insensitive. A detailed comparison of data analyses employed by both experiments is needed for better understanding of this discrepancy.

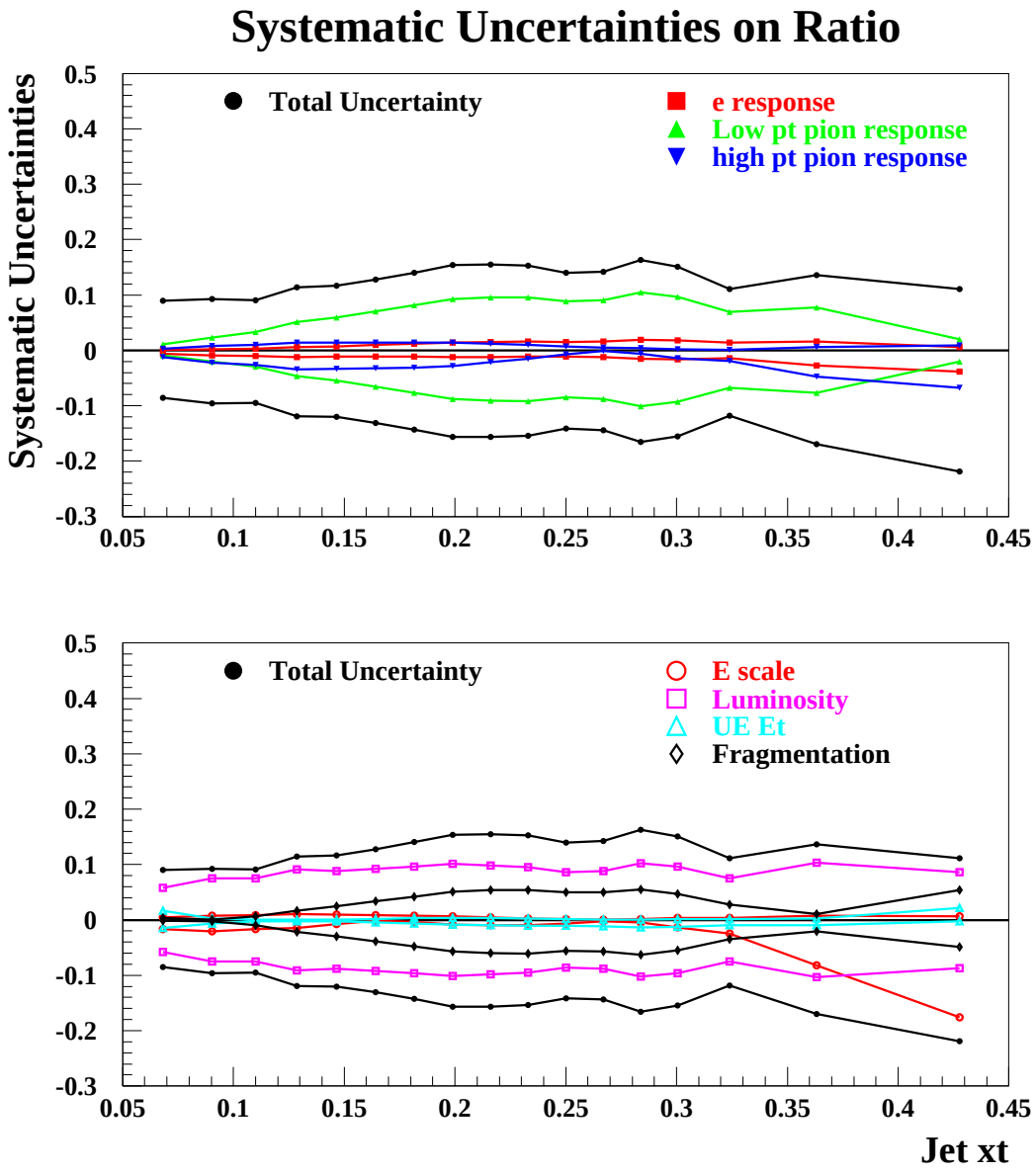

Figure 8.2: The systematic uncertainties on the ratio of scaled inclusive jet cross sections measured at $\sqrt{s}$=630 GeV to $\sqrt{s}$=1800 GeV.

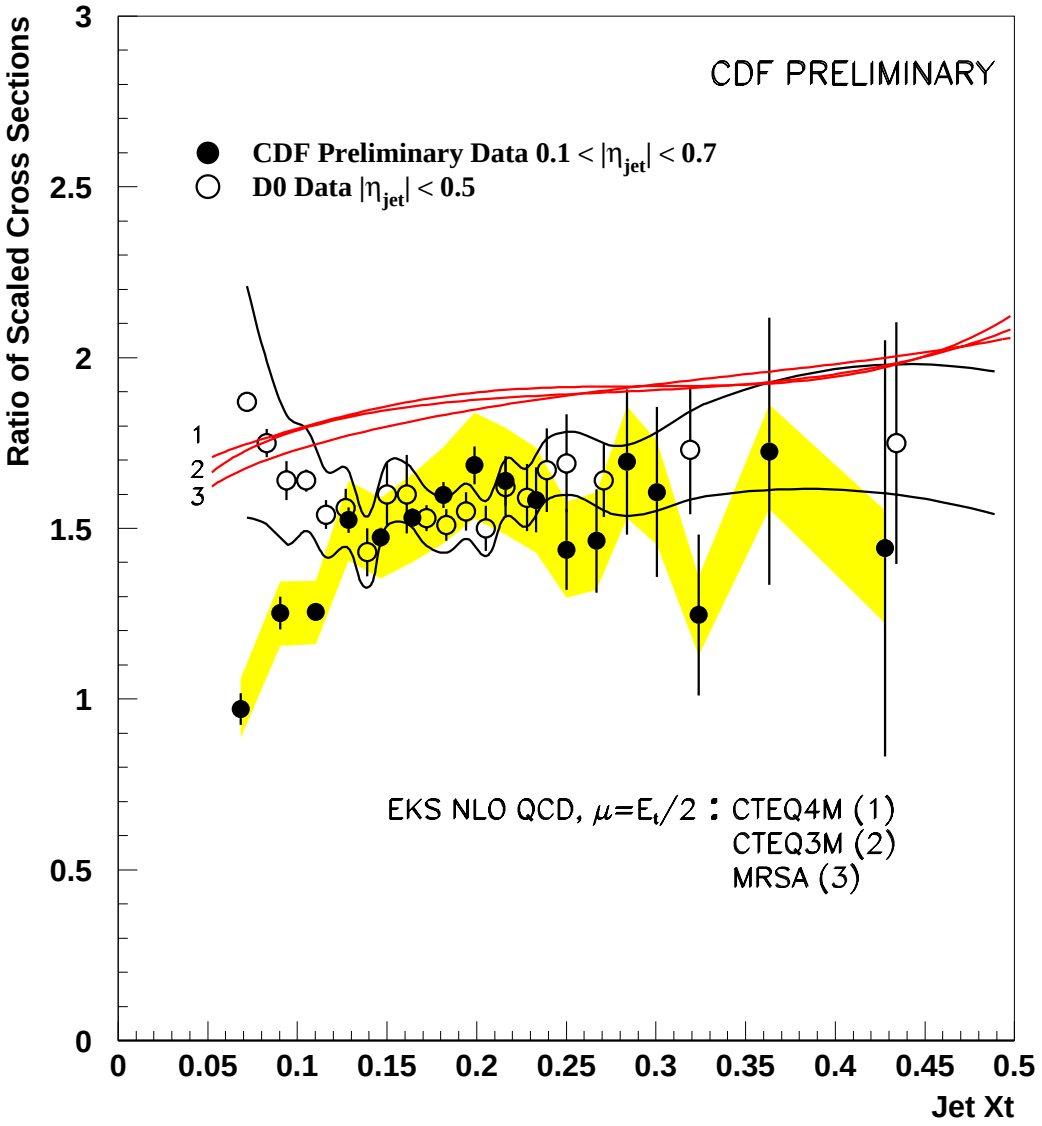

Figure 8.3: Ratio of scaled inclusive jet cross sections measured at $\sqrt{s}$=630 GeV to $\sqrt{s}$=1800 GeV by CDF and DØexperiments.

CDF COLLABORATION

F. Abe,[16] H. Akimoto,[35] A. Akopian,[30] M. G. Albrow,[7] S. R. Amendolia,[26] D. Amidei,[19] J. Antos,[32] S. Aota,[35] G. Apollinari,[30] T. Asakawa,[35] W. Ashmanskas,[17] M. Atac,[7] F. Azfar,[25] P. Azzi-Bacchetta,[24] N. Bacchetta,[24] W. Badgett,[19] S. Bagdasarov,[30] M. W. Bailey,[21] J. Bao,[38] P. de Barbaro,[29] A. Barbaro-Galtieri,[17] V. E. Barnes,[28] B. A. Barnett,[15] M. Barone,[26] E. Barzi,[9] G. Bauer,[18] T. Baumann,[11] F. Bedeschi,[26] S. Behrends,[3] S. Belforte,[26] G. Bellettini,[26] J. Bellinger,[37] D. Benjamin,[34] J. Benlloch,[18] J. Bensinger,[3] D. Benton,[25] A. Beretvas,[7] J. P. Berge,[7] J. Berryhill,[5] S. Bertolucci,[9] B. Bevensee,[25] A. Bhatti,[30] K. Biery,[7] M. Binkley,[7] D. Bisello,[24] R. E. Blair,[1] C. Blocker,[3] A. Bodek,[29] W. Bokhari,[18] V. Bolognesi,[2] G. Bolla,[24] D. Bortoletto,[28] J. Boudreau,[27] L. Breccia,[2] C. Bromberg,[20] N. Bruner,[21] E. Buckley-Geer,[7] H. S. Budd,[29] K. Burkett,[19] G. Busetto,[24] A. Byon-Wagner,[7] K. L. Byrum,[1] J. Cammerata,[15] C. Campagnari,[7] M. Campbell,[19] A. Caner,[26] W. Carithers,[17] D. Carlsmith,[37] A. Castro,[24] D. Cauz,[26] Y. Cen,[29] F. Cervelli,[26] P. S. Chang,[32] P. T. Chang,[32] H. Y. Chao,[32] J. Chapman,[19] M. -T. Cheng,[32] G. Chiarelli,[26] T. Chikamatsu,[35] C. N. Chiou,[32] L. Christofek,[13] S. Cihangir,[7] A. G. Clark,[10] M. Cobal,[26] E. Cocca,[26] M. Contreras,[5] J. Conway,[31] J. Cooper,[7] M. Cordelli,[9] C. Couyoumtzelis,[10] D. Crane,[1] D. Cronin-Hennessy,[6] R. Culbertson,[5] T. Daniels,[18] F. DeJongh,[7] S. Delchamps,[7] S. Dell'Agnello,[26] M. Dell'Orso,[26] R. Demina,[7] L. Demortier,[30] M. Deninno,[2] P. F. Derwent,[7] T. Devlin,[31] J. R. Dittmann,[6] S. Donati,[26] J. Done,[33] T. Dorigo,[24] A. Dunn,[19] N. Eddy,[19] K. Einsweiler,[17] J. E. Elias,[7] R. Ely,[17] E. Engels, Jr.,[27] D. Errede,[13] S. Errede,[13] Q. Fan,[29] G. Feild,[38] C. Ferretti,[26] I. Fiori,[2] B. Flaugher,[7] G. W. Foster,[7] M. Franklin,[11] M. Frautschi,[34] J. Freeman,[7] J. Friedman,[18] H. Frisch,[5] Y. Fukui,[16]

S. Funaki,[35] S. Galeotti,[26] M. Gallinaro,[24] O. Ganel,[34] M. Garcia-Sciveres,[17] A. F. Garfinkel,[28] C. Gay,[11] S. Geer,[7] D. W. Gerdes,[15] P. Giannetti,[26] N. Giokaris,[30] P. Giromini,[9] G. Giusti,[26] L. Gladney,[25] D. Glenzinski,[15] M. Gold,[21] J. Gonzalez,[25] A. Gordon,[11] A. T. Goshaw,[6] Y. Gotra,[24] K. Goulianos,[30] H. Grassmann,[26] L. Groer,[31] C. Grosso-Pilcher,[5] G. Guillian,[19] R. S. Guo,[32] C. Haber,[17] E. Hafen,[18] S. R. Hahn,[7] R. Hamilton,[11] R. Handler,[37] R. M. Hans,[38] F. Happacher,[26] K. Hara,[35] A. D. Hardman,[28] B. Harral,[25] R. M. Harris,[7] S. A. Hauger,[6] J. Hauser,[4] C. Hawk,[31] E. Hayashi,[35] J. Heinrich,[25] K. D. Hoffman,[28] M. Hohlmann,[5] C. Holck,[25] R. Hollebeek,[25] L. Holloway,[13] A. Hölscher,[14] S. Hong,[19] G. Houk,[25] P. Hu,[27] B. T. Huffman,[27] R. Hughes,[22] J. Huston,[20] J. Huth,[11] J. Hylen,[7] H. Ikeda,[35] M. Incagli,[26] J. Incandela,[7] G. Introzzi,[26] J. Iwai,[35] Y. Iwata,[12] H. Jensen,[7] U. Joshi,[7] R. W. Kadel,[17] E. Kajfasz,[24] H. Kambara,[10] T. Kamon,[33] T. Kaneko,[35] K. Karr,[36] H. Kasha,[38] Y. Kato,[23] T. A. Keaffaber,[28] L. Keeble,[9] K. Kelley,[18] R. D. Kennedy,[7] R. Kephart,[7] P. Kesten,[17] D. Kestenbaum,[11] R. M. Keup,[13] H. Keutelian,[7] F. Keyvan,[4] B. Kharadia,[13] B. J. Kim,[29] D. H. Kim,[7a] H. S. Kim,[14] S. B. Kim,[19] S. H. Kim,[35] Y. K. Kim,[17] L. Kirsch,[3] P. Koehn,[29] K. Kondo,[35] J. Konigsberg,[8] S. Kopp,[5] K. Kordas,[14] A. Korytov,[8] W. Koska,[7] E. Kovacs,[7a] W. Kowald,[6] M. Krasberg,[19] J. Kroll,[7] M. Kruse,[29] T. Kuwabara,[35] S. E. Kuhlmann,[1] E. Kuns,[31] A. T. Laasanen,[28] S. Lammel,[7] J. I. Lamoureux,[3] T. LeCompte,[1] S. Leone,[26] J. D. Lewis,[7] P. Limon,[7] M. Lindgren,[4] T. M. Liss,[13] N. Lockyer,[25] O. Long,[25] C. Loomis,[31] M. Loreti,[24] J. Lu,[33] D. Lucchesi,[26] P. Lukens,[7] S. Lusin,[37] J. Lys,[17] K. Maeshima,[7] A. Maghakian,[30] P. Maksimovic,[18] M. Mangano,[26] J. Mansour,[20] M. Mariotti,[24] J. P. Marriner,[7] A. Martin,[38] J. A. J. Matthews,[21] R. Mattingly,[18] P. McIntyre,[33] P. Melese,[30] A. Menzione,[26] E. Meschi,[26] S. Metzler,[25] C. Miao,[19] T. Miao,[7] G. Michail,[11] R. Miller,[20] H. Minato,[35] S. Miscetti,[9] M. Mishina,[16] H. Mitsushio,[35] T. Miyamoto,[35]

S. Miyashita,[35] N. Moggi,[26] Y. Morita,[16] J. Mueller,[27] A. Mukherjee,[7] T. Muller,[4] P. Murat,[26] H. Nakada,[35] I. Nakano,[35] C. Nelson,[7] D. Neuberger,[4] C. Newman-Holmes,[7] C.-Y. Ngan,[18] M. Ninomiya,[35] L. Nodulman,[1] S. H. Oh,[6] K. E. Ohl,[38] T. Ohmoto,[12] T. Ohsugi,[12] R. Oishi,[35] M. Okabe,[35] T. Okusawa,[23] R. Oliveira,[25] J. Olsen,[37] C. Pagliarone,[2] R. Paoletti,[26] V. Papadimitriou,[34] S. P. Pappas,[38] N. Parashar,[26] S. Park,[7] A. Parri,[9] J. Patrick,[7] G. Pauletta,[26] M. Paulini,[17] A. Perazzo,[26] L. Pescara,[24] M. D. Peters,[17] T. J. Phillips,[6] G. Piacentino,[2] M. Pillai,[29] K. T. Pitts,[7] R. Plunkett,[7] L. Pondrom,[37] J. Proudfoot,[1] F. Ptohos,[11] G. Punzi,[26] K. Ragan,[14] D. Reher,[17] A. Ribon,[24] F. Rimondi,[2] L. Ristori,[26] W. J. Robertson,[6] T. Rodrigo,[26] S. Rolli,[26] J. Romano,[5] L. Rosenson,[18] R. Roser,[13] W. K. Sakumoto,[29] D. Saltzberg,[5] A. Sansoni,[9] L. Santi,[26] H. Sato,[35] P. Schlabach,[7] E. E. Schmidt,[7] M. P. Schmidt,[38] A. Scribano,[26] S. Segler,[7] S. Seidel,[21] Y. Seiya,[35] G. Sganos,[14] M. D. Shapiro,[17] N. M. Shaw,[28] Q. Shen,[28] P. F. Shepard,[27] M. Shimojima,[35] M. Shochet,[5] J. Siegrist,[17] A. Sill,[34] P. Sinervo,[14] P. Singh,[27] J. Skarha,[15] K. Sliwa,[36] F. D. Snider,[15] T. Song,[19] J. Spalding,[7] T. Speer,[10] P. Sphicas,[18] F. Spinella,[26] M. Spiropulu,[11] L. Spiegel,[7] L. Stanco,[24] J. Steele,[37] A. Stefanini,[26] K. Strahl,[14] J. Strait,[7] R. Ströhmer,[7a] D. Stuart,[7] G. Sullivan,[5] A. Soumarokov,[32] K. Sumorok,[18] J. Suzuki,[35] T. Takada,[35] T. Takahashi,[23] T. Takano,[35] K. Takikawa,[35] N. Tamura,[12] B. Tannenbaum,[21] F. Tartarelli,[26] W. Taylor,[14] P. K. Teng,[32] Y. Teramoto,[23] S. Tether,[18] D. Theriot,[7] T. L. Thomas,[21] R. Thun,[19] M. Timko,[36] P. Tipton,[29] A. Titov,[30] S. Tkaczyk,[7] D. Toback,[5] K. Tollefson,[29] A. Tollestrup,[7] W. Trischuk,[14] J. F. de Troconiz,[11] S. Truitt,[19] J. Tseng,[18] N. Turini,[26] T. Uchida,[35] N. Uemura,[35] F. Ukegawa,[25] G. Unal,[25] J. Valls,[7a] S. C. van den Brink,[27] S. Vejcik, III,[19] G. Velev,[26] R. Vidal,[7] M. Vondracek,[13] D. Vucinic,[18] R. G. Wagner,[1] R. L. Wagner,[7] J. Wahl,[5] N. B. Wallace,[26] A. M. Walsh,[31] C. Wang,[6] C. H. Wang,[32] J. Wang,[5] M. J. Wang,[32]

Q. F. Wang,[30] A. Warburton,[14] T. Watts,[31] R. Webb,[33] C. Wei,[6] C. Wendt,[37] H. Wenzel,[17] W. C. Wester, III,[7] A. B. Wicklund,[1] E. Wicklund,[7] R. Wilkinson,[25] H. H. Williams,[25] P. Wilson,[5] B. L. Winer,[22] D. Winn,[19] D. Wolinski,[19] J. Wolinski,[20] S. Worm,[21] X. Wu,[10] J. Wyss,[24] A. Yagil,[7] W. Yao,[17] K. Yasuoka,[35] Y. Ye,[14] G. P. Yeh,[7] P. Yeh,[32] M. Yin,[6] J. Yoh,[7] C. Yosef,[20] T. Yoshida,[23] D. Yovanovitch,[7] I. Yu,[7] L. Yu,[21] J. C. Yun,[7] A. Zanetti,[26] F. Zetti,[26] L. Zhang,[37] W. Zhang,[25] and S. Zucchelli[2]

(CDF Collaboration)

[1] *Argonne National Laboratory, Argonne, Illinois 60439*

[2] *Istituto Nazionale di Fisica Nucleare, University of Bologna, I-40127 Bologna, Italy*

[3] *Brandeis University, Waltham, Massachusetts 02264*

[4] *University of California at Los Angeles, Los Angeles, California 90024*

[5] *University of Chicago, Chicago, Illinois 60638*

[6] *Duke University, Durham, North Carolina 28708*

[7] *Fermi National Accelerator Laboratory, Batavia, Illinois 60510*

[8] *University of Florida, Gainesville, FL 33611*

[9] *Laboratori Nazionali di Frascati, Istituto Nazionale di Fisica Nucleare, I-00044 Frascati, Italy*

[10] *University of Geneva, CH-1211 Geneva 4, Switzerland*

[11] *Harvard University, Cambridge, Massachusetts 02138*

[12] *Hiroshima University, Higashi-Hiroshima 724, Japan*

[13] *University of Illinois, Urbana, Illinois 61801*

[14] *Institute of Particle Physics, McGill University, Montreal H3A 2T8, and University of Toronto, Toronto M5S 1A7, Canada*

[15] *The Johns Hopkins University, Baltimore, Maryland 21218*

[16] *National Laboratory for High Energy Physics (KEK), Tsukuba, Ibaraki 315, Japan*

[17] *Ernest Orlando Lawrence Berkeley National Laboratory, Berkeley, California 94720*

[18] *Massachusetts Institute of Technology, Cambridge, Massachusetts 02139*

[19] *University of Michigan, Ann Arbor, Michigan 48109*

[20] *Michigan State University, East Lansing, Michigan 48824*

[21] *University of New Mexico, Albuquerque, New Mexico 87132*

[22] *The Ohio State University, Columbus, OH 43320*

[23] *Osaka City University, Osaka 588, Japan*

[24] *Universita di Padova, Istituto Nazionale di Fisica Nucleare, Sezione di Padova, I-36132 Padova, Italy*

[25] *University of Pennsylvania, Philadelphia, Pennsylvania 19104*

[26] *Istituto Nazionale di Fisica Nucleare, University and Scuola Normale Superiore of Pisa, I-56100 Pisa, Italy*

[27] *University of Pittsburgh, Pittsburgh, Pennsylvania 15270*

[28] *Purdue University, West Lafayette, Indiana 47907*

[29] *University of Rochester, Rochester, New York 14628*

[30] *Rockefeller University, New York, New York 10021*

[31] *Rutgers University, Piscataway, New Jersey 08854*

[32] *Academia Sinica, Taipei, Taiwan 11530, Republic of China*

[33] *Texas A&M University, College Station, Texas 77843*

[34] *Texas Tech University, Lubbock, Texas 79409*

[35] *University of Tsukuba, Tsukuba, Ibaraki 315, Japan*

[36] *Tufts University, Medford, Massachusetts 02155*

[37] *University of Wisconsin, Madison, Wisconsin 53806*

[38] *Yale University, New Haven, Connecticut 06511*

Bibliography

[1] R.P.Feynman, Photon Hadron Interactions, W.A.Benjamin, New York (1972).

[2] R.K.Ellis, W.J.Stirling, B.R.Webber, QCD and Collider Physics, Cambridge University Press (1996).

[3] Particle Data Group, Phys. Rev. **D 50**, 1173 (1994).

[4] J.C.Collins, D.E.Soper, Ann. Rev. Nucl. Part. Sci. **37**, 383 (1987).

[5] V.N.Gribov, L.N.Lipatov, Sov. J. Nucl. Phys. **15**, 438 (1972);
G.Altarelli, G.Parisi, Nucl. Phys. **B 126**, 298 (1977).

[6] A.D.Martin, R.G.Roberts, W.J.Stirling, Phys. Lett. **B 354**, 155 (1995).

[7] M.Glük, E.Reya, A.Vogt, Z. Phys. **C 67**, 433 (1995).

[8] H.L.Lai *et al.*, Phys. Rev. **D55**, 1280 (1997)
hep-ph/9606399.

[9] S.Bethke *et al.*, (JADE Collaboration) Phys. Lett. **B213**, 235 (1988).

[10] S.Catani *et al.*, Phys. Lett. **B269**, 432 (1991).

[11] J.Huth Proc. of the 1990 DPF summer study on HEP, Snowmass, Colorado, World Scientific (1990).

[12] F.Abe *et al.*, (CDF Collaboration) Phys. Rev. **D45**, 1448 (1992)

[13] G.Marchesini *et al.*, Comp. Phys. Commun. **67**, 465 (1992).

[14] S.D.Ellis, Z.Kunszt, D.E.Soper, Phys. Rev. Lett. **64**, 2121 (1990).

[15] J.A.Appel *et al.*, (UA2 Collaboration) Phys. Lett. bf B160, 349 (1985).

[16] T.Akesson *et al.*, (AFS Collaboration) Phys. Lett. bf B118, 185 (1982)
T.Akesson *et al.*, (AFS Collaboration) Phys. Lett. bf B123, 133 (1983).

[17] G.Arnison *et al.*, (UA1 Collaboration) Phys. Lett. bf B172, 461 (1986).

[18] F.Abe *et al.*, (CDF Collaboration) PRL **70**, 1376 (1993).

[19] S.D.Ellis, Proc. XXVIIIth Recontre de Moriond, QCD and High Energy Hadronic Interactions 235 (1993).

[20] F.Abe *et al.*, Nucl. Instrum. Methods **A 271**, 387 (1988).

[21] S.Sedel for CDF Collaboration, Proc. Second Workshop on Vertex Detectors, Slovenia (1994).

[22] F.Snider *et al.*, Nucl. Instrum. Methods **A 268**, 75 (1988).

[23] F.Bedeschi *et al.*, Nucl. Instrum. Methods **A 268**, 50 (1988).

[24] S. Bhadra *et al.* (CDF), Nucl. Instrum. Methods **A 268**, 92 (1988).

[25] L.Balka *et al.*, Nucl. Instrum. Methods **A 267**, 272 (1988).

[26] S.R.Hahn *et al.*, Nucl. Instrum. Methods **A 267**, 351 (1988).

[27] A.Bertoclucci *et al.*, Nucl. Instrum. Methods **A 267**, 301 (1988).

[28] A.Beretvas, B.Flaugher, J.Lamoureux CDF Note 4771 (1998).

[29] D.Amidei *et al.*, Nucl. Instrum. Methods **A 269**, 51 (1988).

[30] H.Areti *et al.*, Proc. 23rd Conf. on HEP, Berkeley, California (1986).

[31] E.Barsotti *et al.*, Nucl. Instrum. Methods **A 269**, 82 (1988).

[32] G.Drake *et al.*, Nucl. Instrum. Methods **A 269**, 68 (1988).

[33] T.Hessing, S.Behrends CDF Note 1132 (1990).

[34] M.Shapiro *et al.*, CDF Note 1810 (1992).

[35] D.Brown, S.Kannappan CDF Note 873 (1989).

[36] T.Hessing *et al.*, CDF Note 1131 (1990).

[37] F.James MINUIT (Function Minimization and Error Analysis) Reference Manual, CERN Program Library, **D506**.

[38] S.Behrends, A.F.Garfinkel, CDF Note 1650 (1988).

[39] J.P.Krane, Ph.D. Thesis, University of Nebraska (unpublished).